# Université Kasdi Merbah Ouargla

---

## Faculté des sciences appliquées

**********

## Département de génie des procédés


---

# Thèse de doctorat en sciences

**Spécialité: Génie des procédés**

**Option: Génie des procédés**


**Présentée par: CHAIB Hadjira**


**Thème**

# Contribution à l'étude structurale et électronique par premiers principes des hydrures à base de lithium solides utilisés pour le stockage réversible de l'hydrogène

**Soutenue publiquement le 06/06/2023**

**Devant le jury composé de :**

| | | | |
|---|---|---|---|
| **M. KORICHI Mourad** | **Professeur** | **Univ. Ouargla** | **Président du jury** |
| **Mme. BENKRIMA Yamina** | **MCA** | **ENS Ouargla** | **Examinatrice** |
| **Mlle. MEFTAH Nassima** | **MCA** | **Univ. El-Oued** | **Examinatrice** |
| **M. SOUIGAT Abdelkader** | **MCA** | **ENS Ouargla** | **Examinateur** |
| **M. BOUKRAA Aomar** | **Professeur** | **Univ. Ouargla** | **Rapporteur** |
| **M. MOHAMMEDI Lazhar** | **Professeur** | **Univ. Ouargla** | **Co-Rapporteur** |

**Année universitaire 2022/2023**

# Abstract

The current work is based on the DFT and FP-LAPW approximations, implemented in the WIEN2k code, to study Li based hydrides used for the reversible storage of hydrogen. Structural, electronic and stability properties of saline hydrides $LiH_n$ (n=1, 2, 4) were calculated in the hope of determining which ones are more hydrogen reversible. The less stable hydride is LiH_221 which has the lowest cohesive energy and could probably be used for hydrogen storage. The effect of the hydrostatic pressure on the LiH hydride (crystallized in 225 space group) was studied to determine the convenient pressure that could be utilized in hydrogen storage systems. The best point for hydrogen storage applications among these points is that corresponding to P=5.972 GPa. In addition, the latter has the smallest lattice parameters, which is satisfactory for hydrogen storage systems. In order to select the most suitable atomic substitutions in $Li_7XH_8$ (X (AM) = Na, K, Rb and X (TM) = Ti, V, Cr), which stores and releases hydrogen quickly and abundantly, the influence of alkali (AM) and transition metal (TM) atom substitutions is qualitatively examined. The hydrides LiH and $Li_7XH_8$'s structural and electronic characteristics are established. The calculated formation energy values and electron properties allow for the determination of the impact of alkali and transition metal atom substitutions on the stability of the hydrides $Li_7XH_8$. In order to find the appropriate and acceptable atomic substitution and achieve both a high storage capacity and a good reversibility for the hydrogen, the gravimetric hydrogen storage parameter is examined alongside the stability of the hydrides $Li_7XH_8$. $Li_7CrH_8$ has been shown to be the least stable phase among all alkali and transition metal atom substitutions. The lattice parameters of the $Li_7CrH_8$ hydride are also less than those of the others. While having a similar relative fall in formation energy, the transition metal substituted hydrides exhibit a smaller relative decline in the gravimetric hydrogen storage density than the alkali metal substituted ones. The explanation of our findings is supported by analyses of the electron density and density of states. The same method, as in $Li_7XH_8$ hydrides, was applied on $Li_3XH_4$ (X (AM) = Na, K, Rb and X (TM) = Ti, V, Cr) to compare, qualitatively and quantitatively, between the two hydride systems. The number and the type of substituted atoms have an effect on the stability and, as a result, on the hydrogen storage performance. The two substitution hydrides falling in the ideal range for fuel cell applications (-20 - -40 kJ/mol $H_2$) are $Li_3RbH_4$ and $Li_3VH_4$ hydride. The less stable hydride, compared to others, is $Li_3CrH_4$ which has the lowest formation energy value lower than the ideal range.

**Keywords**: DFT; FP-LAPW; Li Hydrides; Hydrogen storage; atom substitutions; formation energy.

# ملخص

يعتمد هذا العمل على تقريبات DFT و FP-LAPW، الكائنة في برنامج WIEN2k، لدراسة بعض هيدريدات الليثيوم التي يمكن استخدامها في تخزين الهيدروجين العكوس. تم حساب الخصائص البنيوية، الإلكترونية والإستقرارية لبعض الهيدريدات المالحة $LiH_n$ (حيث: n = 1, 2, 3) على أمل تحديد أي منها أكثر قابلية لعكوسية الهيدروجين. تم الحصول على الهيدريد الأقل استقرارًا وهو LiH_221 الذي يحتوي على أقل طاقة تماسك ويمكن استخدامه على الأرجح لتخزين الهيدروجين. تمت دراسة تأثير الضغط الهيدروستاتيكي على هيدريد LiH (المتبلور في الزمرة الفضائية رقم 225) لتحديد الضغط المناسب الذي يمكن استخدامه في أنظمة تخزين الهيدروجين. أفضل نقطة لتطبيقات تخزين الهيدروجين من بين هذه النقاط هي تلك المقابلة للضغط P= 5.972 GPa. بالإضافة إلى ذلك، ثوابت الشبكة المقابلة لهذا الضغط أصغرية، وهو أمر مرضٍ لأنظمة تخزين الهيدروجين. تم كذلك دراسة تأثير الإستبدال الذري بإستخدام ذرات المعادن القلوية (MA) وذرات المعادن الانتقالية (MT) في هيدريدات الليثيوم بهدف تحديد الاستبدالات المناسبة بين جميع الاستبدالات الممكنة في $Li_7XH_8$ حيث (X (MA) = Na, K, Rb و (X (MT) = Na, K, Rb) ، الذي يخزن ويطرح الهيدروجين بسهولة وبوفرة. تم حساب الخصائص البنيوية والإلكترونية لهيدريدات LiH و $Li_7XH_8$. دراسة تأثير الإستبدلات الذرية للهيدريد $Li_7XH_8$ بإستخدام ذرات المعادن القلوية وذرات المعادن الانتقالية تمت من خلال حساب طاقة التشكل والخصائص الإلكترونية. مقارنة كثافة تخزين الهيدروجين جنبًا إلى جنب مع إستقرار الهيدريد $Li_7XH_8$ بهدف تحديد الاستبدال الذري المناسب والمقبول الذي يحقق سعة تخزين عالية وعكوسية جيدة للهيدروجين في نفس الوقت. تم الحصول على الهيدريد الأقل استقرارًا الموافق لـ $Li_7CrH_8$ بين جميع الإستبدالات الذرية. بالإضافة إلى ذلك، يتميز هذا الهيدريد $Li_7CrH_8$ بثوابت شبكية أصغرية مقارنتا مع غيرها. الانخفاض النسبي في كثافة تخزين الهيدروجين للهيدريدات المستبدلة بذرات المعادن الانتقالية أصغر من الانخفاض النسبي من تلك المستبدلة بذرات المعادن القلوية، على الرغم من أن لديهم انخفاض نسبي مماثل في طاقة التشكل. تدعم كثافة الحالات والكثافة الإلكترونية نتائجنا وتحليلاتنا. تم تطبيق نفس الطريقة السابقة على $Li_3XH_4$حيث (X (MA) = Na, K, Rb و (X (MT) = Na, K, Rb) ومقارنتها كميا ونوعيا مع $Li_7XH_8$. عدد ونوع الذرات المستبدلة يوثر على الاستقرار الهيدريدات، ونتيجة لذلك، على أداء تخزين الهيدروجين. كلى الهيدريدان $Li_3RbH_4$ و$Li_3VH_4$ يقعان في النطاق المثالي لتطبيقات خلايا الوقود (-20 - -40 kJ/mol $H_2$). الهيدريد $Li_3CrH_4$ هو الهدريد الأقل استقرارًا مقارنة بالآخرين والموافق لأقل قيمة طاقة تشكل أقل من النطاق المثالي.

**الكلمات المفتاحية**: DFT؛ FP-LAPW؛ هيدريدات الليثيوم؛ تخزين الهيدروجين؛ الإستبدلات الذرية؛ طاقة التشكل.

# Résumé

Ce travail est basé sur les deux approximations DFT et FP-LAPW, implémentées dans le code WIEN2k, pour étudier les hydrures à base de Li utilisés pour le stockage réversible de l'hydrogène. Les propriétés structurales, électroniques et de stabilité des hydrures salins $LiH_n$ (n = 1, 2, 4) ont été calculées pour déterminer lesquels sont les plus réversibles à l'hydrogène. L'hydrure le moins stable trouvé est LiH_221 qui possède une énergie de cohésion la plus faible et pourrait probablement être utilisé pour le stockage de l'hydrogène. L'effet de pression hydrostatique sur l'hydrure de LiH (cristallisé dans le groupe d'espace 225) a été étudié pour définir la pression appropriée qui pourrait être utilisée dans les systèmes de stockage d'hydrogène. Le meilleur point qui peut être utilisé dans les applications de stockage d'hydrogène parmi ces points est celui correspondant à P=5,972 GPa. De plus, ce dernier présente les paramètres de maille les plus petits, ce qui est satisfaisant pour les systèmes de stockage d'hydrogène. L'effet des substitutions atomiques des métaux alcalins (MA) et de métaux de transition (MT) dans les hydrures à base de Li est étudié, qualitativement, pour déterminer les substitutions atomiques appropriées parmi toutes les substitutions possibles dans $Li_7XH_8$ (X (MA) = Na, K, Rb et X (MT) = Ti, V, Cr) qui stockent et restituent l'hydrogène facilement et considérablement. Les propriétés structurales et électroniques des hydrures LiH et $Li_7XH_8$ sont calculées. L'effet des substitutions atomiques de métaux alcalins et de transition sur la stabilité des hydrures $Li_7XH_8$ est accompli par le calcul des valeurs d'énergie de formation et des propriétés électroniques. Le paramètre gravimétrique de stockage de l'hydrogène est comparé avec la stabilité des hydrures $Li_7XH_8$ pour déterminer la substitution atomique appropriée et acceptable, obtenant simultanément une capacité de stockage élevée et une bonne réversibilité pour l'hydrogène. La phase la moins stable s'est avérée être $Li_7CrH_8$ parmi toutes les substitutions atomiques de métaux alcalins et de transition. De plus, l'hydrure $Li_7CrH_8$ a des paramètres de réseau plus petits que les autres. Le déclin relatif de la densité gravimétrique de stockage d'hydrogène pour les hydrures substitués par un métal de transition est inférieur à celui des hydrures substitués par un métal alcalin, même s'ils ont un déclin relatif similaire de l'énergie de formation. Les analyses de densité d'états et de densité électronique supportent l'explication de nos résultats. La même méthode, comme dans les hydrures $Li_7XH_8$, a été appliquée sur $Li_3XH_4$ (X (MA) = Na, K, Rb et X (MT) = Ti, V, Cr) pour comparer, qualitativement et quantitativement, entre les deux systèmes d'hydrures. Le nombre et le type d'atomes substitués ont un effet sur la stabilité et, par conséquent, sur les performances de stockage de l'hydrogène. Les deux hydrures de substitution se situant dans la gamme idéale pour les applications de pile à combustible (-20 - -40 kJ/mol $H_2$) sont les hydrures $Li_3RbH_4$ et $Li_3VH_4$. L'hydrure le moins stable, comparé aux autres, est $Li_3CrH_4$ qui a une énergie de formation la plus basse, et inférieure à la plage idéale.

**Mots clés**: DFT; FP-LAPW; Hydrures de Li; Stockage de l'hydrogène; Substitutions atomiques; Energie de formation.

# Dedication

I dedicate my thesis work is dedicated to the memory of my farther and my beloved mother, who has been encouraging me for many years. My mum is a unique individual. She took care of me, helped me get dressed, stood up for me, held me, yelled at me, kissed me, but most importantly, she loved me without condition. I am at a loss for words to express how significant my mum was to me.

This thesis work is dedicated to my husband, Lazhar, who has been a constant source of support and encouragement during the challenges of study and life. I am truly thankful for having you in my life.

I am dedicating this work to my brothers and sisters: Brahim, Nacira, Abdelaziz, Karima, Cheikh, Houria, Oum-Elkhir, Mammar, Hocine, Djalil and Mariem.

I dedicate this work to my daughter, Soltana and my sons, Iyad, Laid, Mohammed Baraa and Majid Eddine, remember all things are possible. Never be afraid to pursue your dreams and goals. You are precious gifts from the God. I love you without measure. Thank you for your patience as I pursued and completed this degree.

I also dedicate this thesis to my big families CHAIB and MOHAMMEDI and to my many friends.

# Acknowledgements

First and formost, praises and thanks to the God, the Almighty, for his showers of blessings throughout my research work to complete the research successfully.

I am deeply indebted to the laboratory of Development of New and Renewable Energies in Arid and Saharian Zones, Ouargla University. The work of the thesis was done in this laboratory.

I would like to express my deepest gratitude to my supervisor, Pr. BOUKRAA Aomar, Professor at Ouargla University and Head of the laboratory of Development of New and Renewable Energies in Arid and Saharian Zones, for giving me the opportunity to do research and providing invaluable guidance throughout this research.

Words cannot express my gratitude to my assistant supervisor, Pr. MOHAMMEDI Lazhar, Professor at Ouargla University, for his dynamism for the work, for his support, encouragement and patience.

Special thanks to Pr. KORICHI Mourad, Professor at Ouargla University and Vice-Rector of External Relations, Cooperation, Animation, Communication and Scientific Events, for accepting to chair the jury members and to discuss this work.
Thanks should also go to Dr. BENKRIMA Yamina and Dr. SOUIGAT Abdelkader, from Higher Normal School of Ouargla for being examiners to my work.

I would like to extend my sincere thanks to Dr. MEFTAH Nassima from El-Oued University, for accepting to examine and evaluate my work.

I am also grateful to thank everyone closer or farther who help me to complete this work.

# Contents

# List of figures

# List of tables

# General introduction

One of the fundamental necessities for living is energy. Daily activities such as commuting to work, cleaning, cooking, travelling, working on machines are more or less dependent on energy [1]. Without energy, social progress and world peace are not feasible. Globally, energy is a primary necessity for subsistence [2]. The energy sources are not distributed equally in all geographic locations [3]. The continued population growth has motivated the successful implementation of various energy sources, most of which rely on fossil fuels.

The high demands for fossil fuel energy sources have a big environmental impact. Concerns about climate change, which is currently seen as the biggest global issue, have been caused by the rise in atmospheric greenhouse gas concentrations. Around 33 Gigatons of CO2 were released into the atmosphere in 2019 due to activities related to energy, accounting for almost 87% of all $CO_2$ emissions worldwide [4]. Significant environmental effects brought on by the resultant climate change include the extinction of animal species [5, 6], decreased agricultural productivity [7-9], more frequent extreme weather events [10], human migration [11–13] and wars [14–16]. There is a growing focus on reducing greenhouse gas emissions globally in order to slow the path of climate change. It is reasonable to anticipate that a considerable decrease in fossil fuel use follows from a decrease in greenhouse gas emissions [17].

Energy systems have recently seen some improvements as a result of the COVID-19 epidemic. Fossil fuel consumption has decreased as a result of the epidemic, particularly coal [18], which was using up to half of its capacity by 2020. Moreover, the trend toward a worldwide energy transition has been positively impacted by the growing share of renewable energy sources [19]. Governments are heavily investing in relevant research into hydrogen as a potential fuel and energy source in the future. The main components of the hydrogen economy are production, storage, delivery and usage [20].

The practical storage of hydrogen is likely the biggest barrier to the viability of the hydrogen economy on a wide scale because of its small weight and gaseous form, which create difficult storage challenges. There are numerous physical and chemical ways to store hydrogen. Hence, a storage technique that provides both a high volumetric energy density and a high gravimetric energy density is necessary. Furthermore, it is essential that the hydrogen storage and release process has quick kinetics, low enthalpy change and moderate operating conditions. Other crucial concerns are security, affordability and widespread acceptability [21].

Metal hydrides are among principal methods for hydrogen storage. Hydrogen interacts chemically with metal alloys to form metal hydrides which are considered as promising hydrogen storage materials. The hydride is formed when a hydrogen molecule is dissociated into atomic hydrogen at the surface which diffuses subsequently into the bulk and reacts within the metal or alloy structure [22].

The aim of this work is the enhancement of hydrogen storage properties in Li based hydrides for being more reversible with high density. It is based on the DFT and FP-LAPW approximations, implemented in the WIEN2k code. It is mainly divided into four sections as follows:

- Structural, electronic and stability properties of saline hydrides $LiH_n$ (n=1, 2, 4) were calculated in the hope of determining which ones are more hydrogen reversible.
- The effect of the hydrostatic pressure on the LiH hydride (crystallized in 225 space group) was studied to determine the convenient pressure that could be utilized in hydrogen storage systems.
- The stability of the Li-based hydride is decreased and the hydrogen kinetics are improved by the metal atom substitution of a few lithium atoms. In order to select the most suitable atomic substitutions in $Li_7XH_8$ (X (AM) = Na, K, Rb and X (TM) = Ti, V, Cr), which stores and releases hydrogen simply and abundantly, the influence of alkali (AM) and transition metal (TM) atom substitutions is qualitatively examined. The hydrides LiH and $Li_7XH_8$'s structural and electronic properties are established. The calculated formation energy values and electron properties allow for the determination of the impact of alkali and transition metal atom substitutions on the stability of the hydrides $Li_7XH_8$. In order to find the appropriate and acceptable atomic substitution and achieve both a high storage capacity and a good reversibility for the hydrogen, the gravimetric hydrogen storage parameter is compared with the stability of the hydrides $Li_7XH_8$.
- The same method, as in $Li_7XH_8$ hydrides, was applied on $Li_3XH_4$ (X (AM) = Na, K, Rb and X (TM) = Ti, V, Cr) to compare, qualitatively and quantitatively, between the two hydride systems.

This thesis is organized in three chapters in addition to a general introduction and a general conclusion. The first chapter is reserved for taking overview about hydrogen production and storage. The second chapter describes density functional theory, calculation methods and WIEN2k code. The last chapter is devoted to our results and their discussions.

This thesis is thought to be helpful to all scholars, scientists and professionals interested in the study of hydrogen storage materials.

## References of the general introduction

[1] Rusman NAA, Dahari M. A review on the current progress of metal hydrides material for solid-state hydrogen storage applications, Int J Hydrogen Energy 2016;28:12108-12126.

[2] Dewangan SK, Mohan M, Kumar V, Sharma A, Ahn B. A comprehensive review of the prospects for future hydrogen storage in materials-application and outstanding issues. Int J Energy Research 2022:1-28.

[3] Koultoukis ED, Gkanas EI, Makridis SS, Christodoulou CN, Fruchart D, Stubos AK. High-temperature activated $AB_2$ nanopowders for metal hydride hydrogen compression. Int J Ener Res. 2014;38:477-486.

[4] Muhammad A. Liquid Hydrogen: A Review on Liquefaction, Storage, Transportation, and Safety. Energies 2021;14:5917.

[5] Walsh BS, Parratt SR, Hoffmann AA, Atkinson D, Snook RR, Bretman A, Price TAR. The Impact of Climate Change on Fertility. Trends Ecol Evol 2019;34:249–259.

[6] CaraDonna PJ, Cunningham JL, Iler AM. Experimental warming in the field delays phenology and reduces body mass, fat content and survival: Implications for the persistence of a pollinator under climate change. Funct Ecol 2018;32:2345-2356.

[7] Hernandez-Ochoa IM, Asseng S, Kassie BT, Xiong W, Robertson R, Pequeno DNL.; Sonder, K, Reynolds M, Babar MA, Milan AM, Hoogenboom G . Climate change impact on Mexico wheat production. Agric For Meteorol 2018;263:373-387.

[8] Kontgis C, Schneider A, Ozdogan M, Kucharik C, Tri VPD, Duc NH, Schatz J. Climate change impacts on rice productivity in the Mekong River Delta. Appl Geogr 2019;102:71-83.

[9] Raymundo R, Asseng S, Robertson R, Petsakos A, Hoogenboom G, Quiroz R, Hareau G, Wolf J. Climate change impact on global potato production. Eur J Agron 2018;100:87-98.

[10] Mazdiyasni O, AghaKouchak A. Substantial increase in concurrent droughts and heatwaves in the United States. Proc Natl Acad Sci. USA 2015;112:11484-11489.

[11] Warner K, Ehrhart C, de Sherbinin A, Adamo S, Chai-Onn T. In Search of Shelter: Mapping the Effects of Climate Change on Human Migration and Displacement; Climate Change CARE International. London, UK, 2009;26.

[12] Black R, Bennett SR, Thomas S.M, Beddington JR. Climate change: Migration as adaptation. Nature 2011;478:447–449.

[13] McLeman R, Smit B. Migration as an Adaptation to Climate Change. Clim Chang 2006;76:31-53.

[14] Reuveny R. Climate change-induced migration and violent conflict. Political Geogr 2007;26:656-673.
[15] Nordås R, Gleditsch NP. Climate change and conflict. Political Geogr 2007;26:627-638.
[16] Barnett J. Security and climate change. Glob Environ Chang 2003;13:7-17.
[17] Rivard E, Trudeau M, Zaghib K. Hydrogen Storage for Mobility: A Review. Materials 2019;12:1973.
[18] Mutezo G, Mulopo J. A review of Africa's transition from fossil fuels to renewable energy using circular economy principles. Renew Sustain Energy Rev 2021; 137:110609.
[19] Klemeš JJ, Van Fan Y, Jiang P. The energy and environmental footprints of COVID-19 fighting measures—PPE, disinfection, supply chains. Energy 2020;211:118701.
[20] Moradi R, Groth KM. Hydrogen storage and delivery: Review of the state of the art technologies and risk and reliability analysis. Int J Hydrogen Energy 2017;44:12254-12269.
[21] Usman MR. Hydrogen storage methods: Review and current status. Renewable and Sustainable Energy Reviews 2020;167:112743.
[22] Barthelemy H, Weber M, Barbier F. Hydrogen storage: recent improvements and industrial perspectives. Int J Hydrogen Energy 2017;42:7254-2.

# Chapter I: Overview about hydrogen production and hydrogen storage

## I.1 Introduction

Due to its vast availability in its oxidized condition in nature, hydrogen is the most common element on Earth (also known as water). Via a variety of conversion technologies, such as thermochemical, electrochemical and biological processes, it can be created from primary energy sources. Additionally, because hydrogen can be converted into and out of other secondary energy sources like heat and electricity, this might result in a mutual conversion of these other secondary energy sources [1].

An increasingly practical, safe and ecofriendly choice for transportation and energy storage is hydrogen. The most energetic gas by weight, hydrogen creates mainly water as a waste when used in fuel cells. It can be stored in both little and big amounts using a variety of techniques. A future hydrogen economy may benefit from a variety of physical and chemical hydrogen storage systems, each with unique capabilities and storage capacities [2].

Gaseous, liquid, or solid forms of hydrogen can all be stored. The primary strategies for storing hydrogen are as follows [3-5]:

- Compressed hydrogen
- Liquefied hydrogen
- Cryo-compressed hydrogen
- Physically adsorbed hydrogen
- Metal hydrides
- Complex hydrides
- Liquid organic hydrogen carriers (LOHC) or Liquid organic hydrides

This chapter is to review hydrogen properties, hydrogen production and currently available hydrogen storage methods.

## I.2 Hydrogen properties

The chemical element hydrogen is represented by the letter H and atomic number 1. The periodic table's lightest element, hydrogen possesses the smallest and lightest molecular structure. The hydrogen molecule is exceedingly small (van der Waals radius of 120 pm) and approximately 14 times lighter than air at 20 °C and 1 atm, respectively. It also has a high diffusion rate (0.61 $cm^2/s$) and buoyancy [6]. It is non-toxic, colorless, odorless and highly flammable. It is used to bombard neutrons to form radioactive isotopes which are utilized in nuclear devices [7]. Table I.1 lists the physical and chemical properties of hydrogen.

**Table I.1:** Physical and chemical properties of hydrogen.

| Properties | Value | Ref. |
|---|---|---|
| Name, symbol, number | Hydrogen, H, 1 | [7] |
| Molecular weight (g/mol) | 2.016 | [7] |
| Lower heating value (MJ/kg) | 118.8 | [7] |
| Higher heating value (MJ/kg) | 143 | [7] |
| Electrons, protons, neutrons | 1, 1, 0 | [7] |
| Category | Nonmetal | [7] |
| Group, period, bloc | 1, 1, s | [7] |
| Density of gaseous hydrogen at 25°C and 1atm ($kg/m^3$) | 0.08987 | [1, 7, 8] |
| Density of liquid hydrogen at -253°C ($kg/m^3$) | 70.85 | [1, 7, 8] |
| Density of solid hydrogen at -259 °C ($kg/m^3$) | 858 | [1, 7, 8] |
| Critical density ($kg/m^3$) | 31.2 | [1, 8] |
| Atomic radius ( Å) | 0.259 | [7] |
| Electronic Configuration | $1s^1$ | [7] |
| crystal structure | Hexagonal | [7] |
| Ionic radius (nm) | 0.208 | [7] |
| Isotope | 3 | [7] |
| Viscosity at 25°C (cP: centipoise) | 0.0008992 | [1, 8] |
| Melting point (°C) | -259.2 | [7, 8] |
| Boiling point at 1 atm (°C) | -252.8 | [1, 7, 8] |
| Ionization energy | 13.5989 eV | [7] |
| Flash point (°C) | −253 | [7] |
| Critical temperature (°C) | -240 | [1, 8] |
| Critical pressure (MPa) | 1.3 | [1, 8] |
| Research octane number (RON) >130 | >130 | [1, 7] |
| Toxicity | None, simple asphyxiant | [7] |
| Heat capacity of hydrogen gas at 25°C (kJ/kg °C) | 14.3 | [1, 9] |
| Heat capacity of hydrogen liquid at -256°C (kJ/kg °C) | 8.1 | [1, 9] |
| Heat capacity of hydrogen liquid at -259.8°C (kJ/kg °C) | 2.63 | [1, 8] |
| Heat of vaporization at -253°C (kJ/kg) | 447 | [1, 8] |
| Heat of fusion at -259 °C (kJ/kg) | 58 | [1, 8] |
| Thermal conductivity at 25°C (W/cmK) | 0.018 | [1, 8] |
| Latent heat of vaporization (kJ/kg) | 461 | [1] |

In comparison to water, organic solvents are slightly more soluble in hydrogen. Many metals can absorb hydrogen. Steel that has absorbed hydrogen may become brittle, which could eventually cause mechanical and chemical processes to fail. Hydrogen is not a very reactive substance at room temperature unless it has been somehow activated, such as by the right catalysis. It is quite reactive at high temperatures. At high temperatures, the molecule hydrogen separates into free atoms. Even at room temperature, atomic hydrogen is a strong reductant.

In order to create free metals, Hydrogen reacts with the oxides and chlorides of numerous metals, including silver, copper, lead, bismuth and mercury. Certain salts, including nitrates, nitrites, sodium and potassium cyanides, are reduced to their metallic state via this process. It produces hydrides such as NAH, KH, $H_2S$ and $PH_3$ when it reacts with a variety of elements, including metals and non-metals. Hydrogen peroxide, $H_2O_2$, is created when atomic hydrogen and oxygen combine.

## I.3 Hydrogen production

The industrial production of hydrogen can be classified into three big categories according to three colors which are [9]:

- Green hydrogen, which means hydrogen production based on renewable energy.
- Purple hydrogen, which means hydrogen production based on nuclear energy.
- Blue hydrogen, which means hydrogen production based on coal gasification and natural gas integrated with carbon capture and storage methods.

There are many important hydrogen production processes such as steam methane reforming, coal gasification, naphtha reforming, landfill gas dry reformation, steam reforming of waste oil, $H_2S$ methane reforming, steam-iron process, methane/natural gas pyrolysis, partial oxidation of heavy oil and coal, grid electrolysis of water, photolysis of water, chloralkali electrolysis, solar and Photovoltaic water electrolysis, high-temperature water electrolysis, thermochemical water splitting, photobiological, biomass gasification, photoelectrochemical water decomposition and photocatalytic water decomposition. The major share of hydrogen production is currently obtained by the steam methane reforming which is a $CO_2$ intensive process. Electrolysis is a conventional method that splits water into green hydrogen and oxygen by passing an electrical current coming from renewable energy sources. There are no $CO_2$ gas emissions from the electrolysis technique. Hydrogen production with steam methane reforming costs approximately three times more than with the natural gas per unit of produced energy. Similarly, hydrogen production with electrolysis costs 5 cents/kWh of electricity, roughly twice that of natural gas [9]. Fig. I.1 exhibits the classification of renewable, conventional and other hydrogen production methods [9].

### 1.3.1 Green hydrogen production

Green hydrogen production is referred to renewable energy sources. Green hydrogen is extracted from the water electrolysis operating by electrical current. The latter is generated by low-carbon

power sources which are known as renewable energy sources. The electrolysis process needs just electricity from renewable energy sources for giving green hydrogen production.

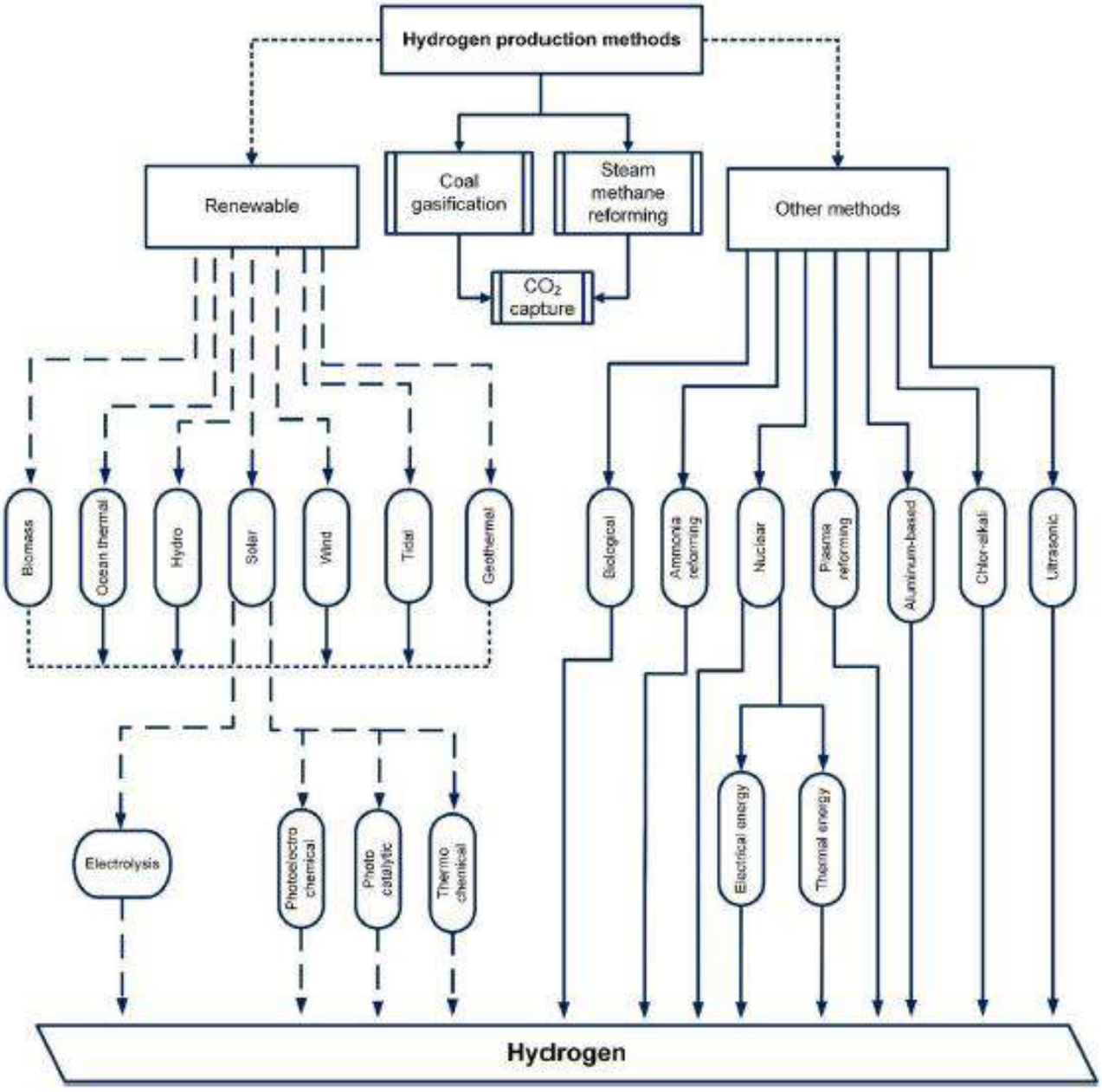


**Figure I.1:** Hydrogen production methods.

The simplest way to produce hydrogen from water is employed with two reactions in each electrode [10, 11]:

$$Anode \Longrightarrow \ H_2O + electricity \rightarrow \frac{1}{2}O_2 + 2H^+ + 2e^- \qquad \text{(I.1)}$$

$$Cathode \Longrightarrow \ 2H^+ + 2e^- \rightarrow H_2 \quad \text{(I.2)}$$

$$Overall\ process \Longrightarrow \ H_2O + electricity \rightarrow \frac{1}{2}O_2 + H_2 \quad \text{(I.3)}$$

There are different technologies for water electrolysis, the most important being: proton-exchange membrane PEM electrolyser, alkaline ALK electrolyser and solid oxide SO electrolyser [12, 13]. The PEM electrolyser has many advantages compared to other eletrolysers.

#### 1.3.1.1 Solar energy

The solar energy is considered as an important source of renewable energy in order to produce clean and sustainable green hydrogen. Fig I.2 shows solar energy sources classification for producing green hydrogen [9]. The classes of solar energy sources are the photo-electrochemical, solar thermal and solar photovoltaic [14].

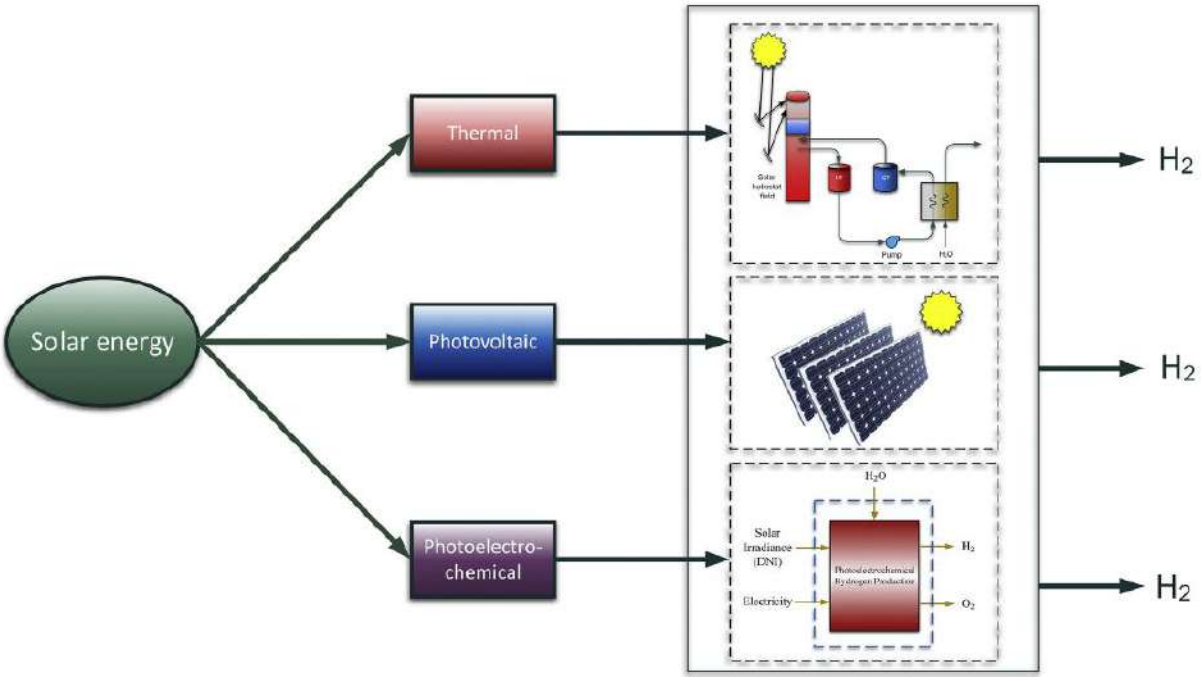


**Figure I.2:** Classification of solar energy for producing green hydrogen.

#### 1.3.1.2 Wind energy

Wind turbines are used to convert kinetic energy into electrical energy. The latter is employed in electrolysis to produce green hydrogen. Wind energy is a renewable energy source depending on

wind turbine installations and geographic locations [15-17]. Fig. I.3 displays green hydrogen production from onshore and offshore wind energy [9].

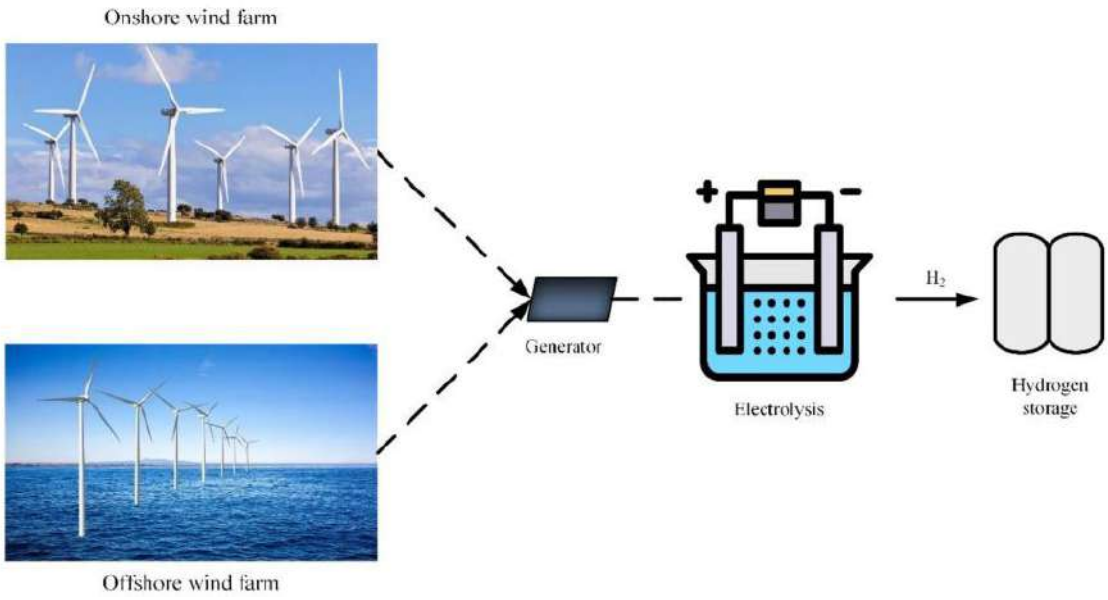


**Figure I.3:** Green hydrogen production from onshore and offshore wind energy.

#### 1.3.1.3 Geothermal energy

Geothermal energy is generated from heat in the earth's interior. It can be utilized to produce electrical energy which would be employed in electrolysis. Geothermal energy can be used to heat water making electrolysis more efficient in producing green hydrogen [18].

#### 1.3.1.4 Hydro energy

Hydro-energy is obtained from water potential energy converted into electricity. It is considered as a renewable energy source. The conversion of water kinetic energy into electricity is an effective method for large-scale electricity generation. This conversion does not contain chemical or thermodynamic processes. Hydropower energy flows can be concentrated and controlled [19].

#### 1.3.1.5 Ocean thermal energy conversion

Ocean thermal energy conversion can be used to generate electricity, due to temperature gradients between deep cold ocean water and warm surface ocean water. In tropical regions, temperature difference may be over 20°C. Ocean thermal energy conversion technology is known as a marine renewable energy system [9].

#### 1.3.1.6 Biomass gasification

The gasification process is used to convert solid biomasses (organic materials or carbonaceous fossil fuels) into combustible producer gases by several thermochemical reactions [20]. The producer gases are a mixture of carbon monoxide, carbon dioxide and hydrogen. The gasification process is a cleaner conversion process. Contrary to combustion, it produces fuel in the form of unburned producer gases, preventing many pollutants to be emitted such as $NO_x$, $SO_x$ and other particles that occur at higher temperatures than typical gasification temperatures [21].

### 1.3.2 Purple hydrogen production

Purple hydrogen is obtained from nuclear energy at high temperature. The fusion nuclear reactors need uranium atoms, as fuel, to work and subsequently to produce heat for generating stream. This generated stream moves the turbines in order to produce electricity.

### 1.3.3 Blue hydrogen production

Fossil fuels currently dominate the global hydrogen supply because of the close correlation between production costs and fuel prices, which are still kept at reasonable levels [22]. Fossil fuels are made of massive, dense hydrocarbon molecules. One of the most often used processes for producing hydrogen involves removing hydrogen by rupturing the bonds between hydrogen and carbon. These substances can be extracted for instance from biomass, coal, gasoline, oil (heavy and light), methanol and methane [23-25]. To collect the released $CO_2$ emissions, carbon capture and storage (CCS) or carbon capture and utilization (CCU) techniques are being integrated with the currently used conventional hydrogen production installations [9].

#### 1.3.3.1 Stream reforming

The stream reforming reaction is a mixture of steam with hydrocarbons at high temperatures to produce carbon oxides and hydrogen. The extracted hydrogen, by stream reforming process, is mostly from natural gas and much less from liquefied petroleum gas and naphtha [26]. The stream methane reforming from natural gas or light hydrocarbons is the most used stream reforming process. The chemical reaction of the stream methane reforming is presented as follows:

$$Overall\ process \Longrightarrow \ CH_4 + 2H_2O \rightarrow CO_2 + 4H_2 \qquad \text{(I.4)}$$

The stream methane reforming reaction is highly endothermic, which needs a high temperature from 800 to 1000°C. In order to produce blue hydrogen, highly resistant materials should be used to overcome thermal stresses.

#### 1.3.3.1 Coal gasification

Coal gasification is defined as a conventional process used for blue hydrogen production. The coal gasification converts coal into gaseous products, including carbon monoxide and hydrogen. This conversion is performed in the presence of air at high temperatures and pressures [27-29]. The main problem associated with hydrogen production through coal gasification is related to higher $CO_2$ emissions. It should be treated with carbon capture-based technologies.

## I.4 Hydrogen storage

When it comes to the large-scale use of hydrogen, hydrogen storage is regarded as a crucial component in hydrogen energy systems [2]. The storage of hydrogen is the primary technological obstacle in the way of a sustainable hydrogen economy, and up until now, this has proven to be an insurmountable obstacle. For hydrogen to be practical for transportation, its energy density must be increased. The challenge with storing hydrogen is being solved, though, and quickly. Researchers are looking into novel ways to store hydrogen [30]. Hydrogen storage techniques could be classified according to physical or chemical storage (Table I.2). Fig. I.4 shows the principles of various hydrogen storage methods [9].

**Table I.2:** Physical and chemical techniques for hydrogen storage.

| Physical storage | Chemical storage |
|---|---|
| Compressed gas (pressure higher than 30 MPa) | Hydrides (e.g., $MgH_2$, $NaAlH_4$, $NH_3BH_3$, $FeTiH_2$) |
| Liquid (temperature -253°C at 1 atm) | Adsorption (e.g., MOFs, CNTs) |
| Cryo-compressed (e.g., pressure 35 Mpa at -253°C) | Liquid organic carriers (e.g., $C_6H_6/C_6H_{12}$) |
| Slush (combination of liquid and solid hydrogen at triple point) | Reformed organic fuels (e.g., methanol, gasoline) |

### I.4.1 Compressed hydrogen

This compressed hydrogen storage method is widely used for compressing hydrogen at high pressures [31, 32]. This method offers high rates of hydrogen storage and release. There is no extra energy needed to release hydrogen [33, 34]. Additionally, the compression of hydrogen costs just about 13-18% of the lower heating value of hydrogen [33].

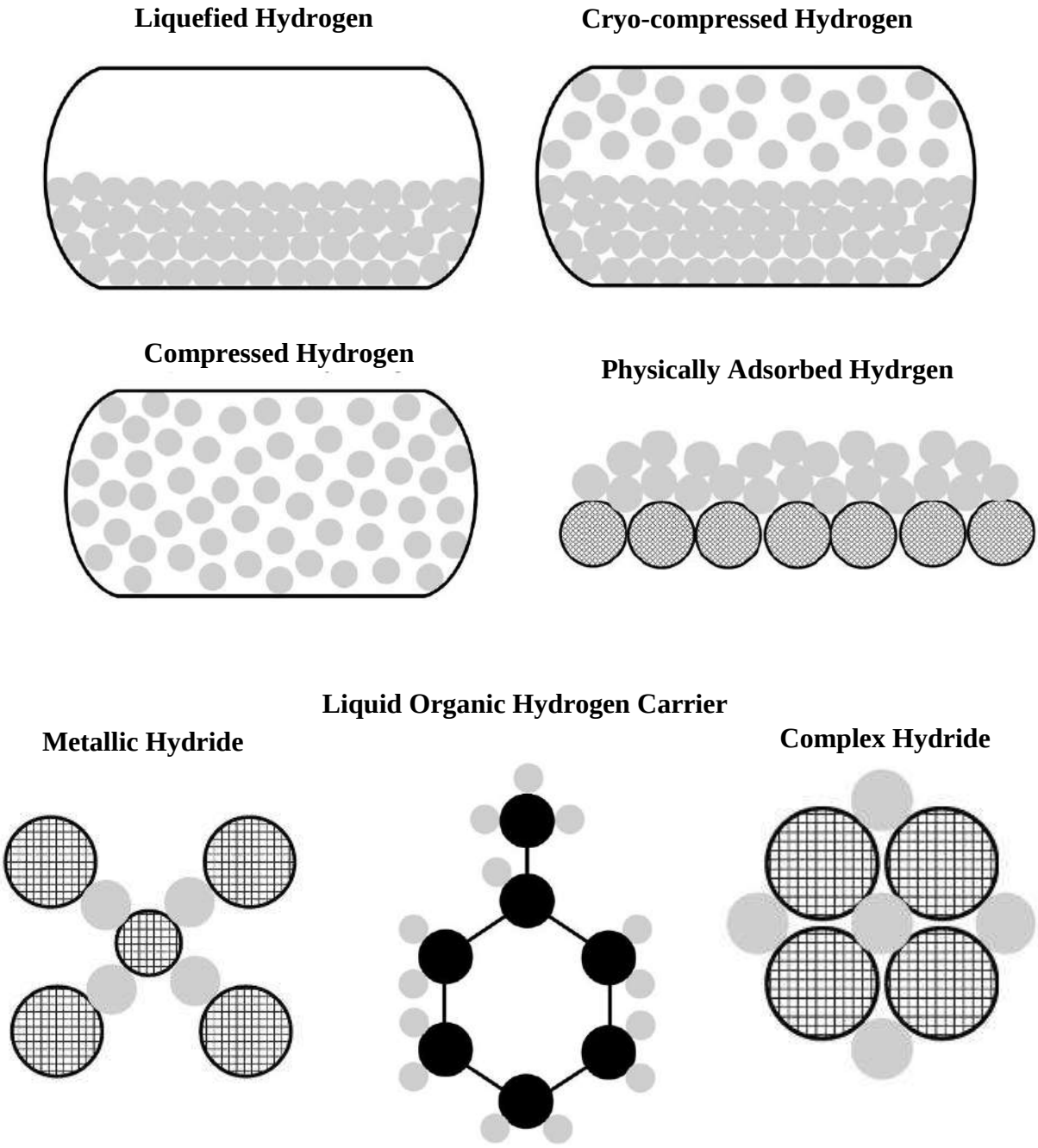


**Figure I.4:** Principles of various hydrogen storage methods.

Hydrogen is stored in either spherical or cylindrical vessels. The storage difficulties in this method, due to high hydrogen pressures, arise from the vessel materials which should be low cost, light weight and more resistant to hydrogen diffusion. According to the criteria above, there are many different types of vessels used for storing compressed hydrogen gas [2, 36, 37]. Table I.3 summarizes the types of vessels used in the compressed hydrogen method.

**Table I.3:** Types of vessels used in the compressed hydrogen method.

| Type | Vessel characteristics | Ref. |
|---|---|---|
| I | • Metallic materials: construction materials are from steel or aluminum alloy<br>• Resistant pressure up to 30 bar<br>• Thick wall<br>• Heavy weight<br>• Low energy density about 1 wt.% $H_2$ | [2, 35-37] |
| II | • Metallic wall wrapped with resin composite<br>• 30-40 less weight compared to Type I<br>• 50% more cost compared to Type I | [2, 35, 36] |
| III | • Carbon fiber composite materials covered with metal as aluminum<br>• Strong and light weight<br>• Low thermal conductivity<br>• Low rate of heat release during the compression of hydrogen<br>• Suitable for applications with pressure of 450 bar<br>• Used up to 700 bar hydrogen pressure | [2, 32] |
| IV | • Carbon fiber composite materials covered with a polymeric liner<br>• Store hydrogen at pressure of 700 bar<br>• Hydrogen energy density of 5.7 MJ/l at 700 bar | [2, 36, 38] |

The compressed hydrogen vessels have less public acceptance and have explosion risks due to shocks [39]. The compressed hydrogen as fuel cell are commercialized and more vehicles are sold and running on the roads (for example: Toyota Mirai (2021), with hydrgen compressed at 700 bar, can move 600 km in one single charge) [40].

### I.4.2 Liquefied hydrogen

Liquefied hydrogen $LH_2$ has higher density, around 70.85 g/l at -253°C, due to increased volumetric energy density to 8MJ/$LH_2$ [24, 31]. The critical hydrogen temperature of hydrogen is -240 °C, consequently hydrogen should be cooled under this critical temperature for liquefaction. Liquid hydrogen storage is a well-established technology which offers high rates of hydrogen release similar to compressed hydrogen [38]. The tank size of liquefied hydrogen is reduced, compared with compressed hydrogen, to an acceptable value. The liquid hydrogen is non corrosive and has low applied pressure on the tank wall. The liquid hydrogen vessels are made of stainless steel and aluminum alloy with insulation for cryogenic storage [30]. The liquefaction of hydrogen is costly because of the use of liquefaction technologies. Liquid hydrogen infrastructures raise many challenges, dependent on temperature conditions [37, 41].

### I.4.3 Cryo-compressed hydrogen

Both the compressed and liquefied hydrogen are combined to form the cryo-compression aspect. the hydrogen is stored under minimum hydrogen pressures of 250-350 bar and cryogenic temperatures [32, 42-44]. The cryo-compressed hydrogen has a density of 80 g/l which is higher than that of liquefied hydrogen [2, 36, 39]. In this method the filling and releasing hydrogen rates are rapid and the infrastructures are related to the compression and liquefaction of hydrogen [2, 41, 44].

### I.4.4 Metal hydrides

Hydrides are formed by interacting metals or metal alloys with hydrogen. A hydrogen molecule is dissociated into hydrogen atoms at the surface and followed by diffusion into the metal alloys (as host metal) to form hydrides. The insertion of hydrogen atoms into a host metal passes through three effects which are structural transformation, lattice expansion and hydrogen-metal interaction. The reversible formation of a metal hydride can be accomplished by direct reaction of hydrogen with a host metal or by the electrochemical splitting of water molecules [45]. The two chemical reactions are as follows [34, 46]:

$$Direct\ hydrogen\ reaction \Longrightarrow\ \ M(s) + \frac{x}{2}H_2(g) \leftrightarrow MH_x(s) + Q \qquad \text{(I.5)}$$

$$Electrochemical\ splitting\ of\ water \Longrightarrow\ \ M(s) + \frac{x}{2}H_2O(l) + \frac{x}{2}e^- \leftrightarrow MH_x(s) + \frac{x}{2}OH^-(l) \qquad \text{(I.6)}$$

*M (s)* is a host metal or alloy. The reversible hydrogen reaction with a metal occurs by increasing temperature or by decreasing pressure [47]. Absorption (filling) and desorption (releasing) of hydrogen must have equal energies to be reversible. The metal hydrides have higher hydrogen storage density than all physical hydrogen storage systems [24, 32, 36, 48, 49]. They store hydrogen at moderate temperature and pressure [24, 32, 48, 49]. The moderate formation energy for recommended metal hydride applications is in the range 20-55 kJ/mol $H_2$ [47]. However, metal hydrides have low absorption/desorption kinetics, and need high temperature and high pressure during hydrogen charging and discharging [47,50]. Additionally, The Proton Exchange Membrane PEM fuel cells in electric vehicles have operating conditions which are 1-10 bar for pressure, 1-100°C for temperature and 30-48 kJ/mol $H_2$ for formation energy [45]. The thermal management is another problem in refueling stations for on-board applications [51]. The intermetallic hydrides have intermediate stability which is good for hydrogen kinetics but

gravimetric hydrogen densities are less than 3% wt [27, 43, 52]. Table I.4 shows many storage characteristics of some metal hydrides. The enhancement of metal hydride properties can possibly be with reducing the crystal grain size, decreasing the particle size, alloying, adding additives to produce composites, using catalysts, nanostructuring and nanoconfinement [9].

**Table I.4:** Storage characteristics of some metal hydrides.

| Metal hydrides | $H_2$ Density (wt%) | Formation energy (kJ/mol $H_2$) | Ref. |
|---|---|---|---|
| $MgH_2$ | 7.6 | 75 | [24, 45] [53-63] |
| $Mg_2FeH_6$ | 5.5 | 77.6 | |
| $Mg_2NiH_6$ | 3.59 | 65 | |
| $LaNi_5H_6$ | 1.4 | 31 | |
| $FeTiH_2$ | 1.89 | 28 | |

## I.4.5 Complex hydrides

Complex hydrides are composed from covalent hydrogen atoms bonding with a central atom in complex coordinates such as $[BH_4]^{-1}$, $[NH_2]^{-1}$, $[AlH_4]^{-1}$and $[AlH_6]^{-3}$ as an anion and Li, Mg and Zn as a cation. The complex hydrides offer high storage densities (Table I.5). They can be classified into the following three major categories: alanates, borohydrides and amides-imides.

**Table I.5:** Some storage properties of complex hydrides.

| Complex hydrides | $H_2$ Density (wt%) | Formation energy (kJ/mol $H_2$) | Ref. |
|---|---|---|---|
| $NaAlH_4$ | 5.6 | 41 | [35, 46, 47] [64-67] |
| $LiAlH_4$ | 7.9 | 5.8 | |
| $LiBH_4$ | 13.5 | 67 | |
| $Mg(NH_2)_2$-LiH | 5.6 | 54 | |
| $LiNH_2$-LiH | 5.5 | 44 | |

These complex hydrides pose difficulties and drawbacks for hydrogen reversibility (see references [64, 65, 59, 68, 69]). The drawbacks in the complex hydrides can be overcome by catalysis, ball milling, alloying and nano-engineering. Previous works referenced here as [58, 62,

65, 67, 70-75]) have focused on the improvement of hydrogen kinetic properties in complex hydrides.

### I.4.6 Physically hydrogen adsorption

Hydrogen is adsorbed physically at the surface of the solids using van der Waals interactions. In this mode of storage, hydrogen is more reversible and offers high kinetic adsorbed/desorbed reactions [49, 52, 76, 77]. Therefore, formation energy values are only 1-10 kJ/mol [9]. The heat problems are easier to control and manage [2]. Microporous carbon structures, metal organic frameworks and zeolites are candidate adsorbent materials (physical adsorption). Metal organic frameworks are adaptable and have several design options. Zeolites are aluminosilicates that are microporous and organized and have a sizable surface area. High surface area in adsorbent materials is certainly a requirement.

Table I.6 show some storage properties of adsorbent materials.

**Table I.6:** Some storage properties of adsorbent materials.

| **Absorbent materials** | **$H_2$ Density (wt%)** | **Ref.** |
|---|---|---|
| Activated carbon at 77 K and 30–60 bar | 5 wt% $H_2$ | [78] |
| Single Walled Carbon Nano Tubes (SWCNTs) at 77 K and 10 MPa | 1.73 wt% | [77, 79] |
| Various types of CNTs (inclusive SWCNTs and MWCNTs) with and without post modifications at room temperature and 12 MPa | less than 1.7 wt%. | [80] |
| CaX zeolite at 15 bar and 77 K | 2.19 wt% | [81] |
| NaX zeolite at 77 K and 40 bar | 2.55 wt% | [82] |
| Metal organic frameworks-210 MOF-210 at 77 K and 80 bar | 7.9 wt% | [83] |
| Metal organic frameworks-5 MOF-5 at 77 K and near ambient pressure | 4.5 wt% | [84] |
| Metal organic frameworks-5 MOF-5 at room temperature and 20 bar | 1 wt% | |
| NU-100 at 56 bar and 77 K | 9 wt% | [85] |

The drawbacks of this mode of storage for being in onboard applications are because of low temperature conditions.

### I.4.7 Liquid organic hydrogen carriers

This mode of storage has two names: Liquid organic hydrogen carrier LOHC or liquid organic hydride LOH. The hydrogen is stored chemically in hydrogen vacant sites of organic molecules. Fig I.5 displays the organic hydride cycle construct for on board and stationary applications. The needed hydrogen in LOH is removed in the reactor for power production. The latter can be in stationary power plants or on motor vehicles. The consumptive product (LOHC less $H_2$) is transferred into storage tanks and subsequently into hydrogenation facilities for getting recharged hydrogen organic hydride. LOHC (more $H_2$) returns in the direction of storage tanks and then toward stationary power plants or on motor vehicles. The carbon atoms reside in the cycle and do not leave for the exterior. Gravimetric hydrogen density of LOHC varies in the range 1.7-7.3 at%. LOHC remains a liquid at room temperature [9]. The drawbacks in this mode of storage are the infrastructure.

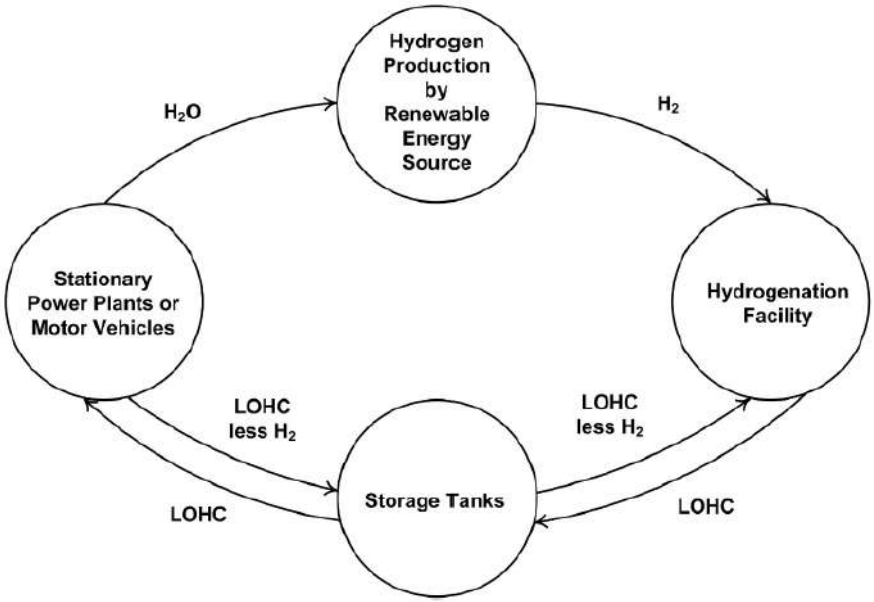


**Figure I.5:** Construct of the organic hydride cycle.

## I.5 References of the chapter I

[1] Muhammad A. Liquid Hydrogen: A Review on Liquefaction, Storage, Transportation, and Safety. Energies 2021;14:5917.

[2] Moradi R, Groth KM. Hydrogen storage and delivery: Review of the state of the art technologies and risk and reliability analysis. Int J Hydrogen Energy 2019;44:12254-12269.

[3] Usman MR. Hydrogen storage methods: Review and current status. Renewable and Sustainable Energy Reviews 2020;167:112743.

[4] Principi G, Agresti F, Maddalena A, Lo Russo S. The problem of solid state hydrogen storage. Energy 2009;34(12):2087-2091.

[5] Zlotea C, Latroche M. Role of nanoconfinement on hydrogen sorption properties of metal nanoparticles hybrids. Coll Surf A Physicochem Eng Asp 2013;439(0):117-130.

[6] Kovač A, Paranos M.; Marciuš D. Hydrogen in energy transition: A review. Int J Hydrogen Energy 2021;46:10016-10035.

[7] Mazloomi K, Gomes C. Hydrogen as an energy carrier: Prospects and challenges. Renew. Sustain Energy Rev 2012;16:3024-3033.

[8] Najjar Y.S. Hydrogen safety: The road toward green technology. Int J Hydrogen Energy 2013:38:10716-10728.

[9] Ishaq H, Dincer I, Crawford C. A review on hydrogen production and utilization: Challenges and opportunities. Int J Hydrogen Energy 2022;47:26238-26264.

[10] Safari F, Dincer I. A Review and Comparative Evaluation of Thermochemical Water Splitting Cycles for Hydrogen Production. Energy Convers Manage 2020;205:112182.

[11] Schmidt O, Gambhir A, Staffell I, Hawkes A, Nelson J, Few S. Future Cost and Performance of Water Electrolysis: An Expert Elicitation Study. Int J Hydrogen Energy 2017;42(52):30470−30492.

[12] Brauns J, Turek T. Alkaline Water Electrolysis Powered by Renewable Energy: A Review. Processes 2020; 8 (2):248.

[13] Chi J, Yu H. Water Electrolysis Based on Renewable Energy for Hydrogen Production. Chin J Catal 2018;39 (3):390-394.

[14] Calise F, D'Accadia MD, Santarelli M, Lanzini A, Ferrero D. Solar hydrogen production: processes, systems and technologies. In: Sol Hydrog Prod Process Syst Technol;2019.

[15] Wang S, Liu J. Life-cycle green-house gas emissions of onshore and offshore wind turbines. J Clean Prod 2019;210:804-810.

[16] Letcher TM. Wind energy engineering: a handbook for onshore and offshore wind turbines. Wind energy eng. A handb. onshore offshore wind turbines;2017.
[17] Jacobson MZ. 100% clean, renewable energy storage for everything. Chapter 6: Onshore and offshore wind energy, Stanford University, california 2020:192-247.
[18] Soltani M, Kashkooli FM, Dehghani-Sanij AR, Kazemi AR, Bordbar N, Farshchi MJ, Elmi M, Gharali K, Dusseault M B. A comprehensive study of geothermal heating and cooling systems. Sustain Cities Soc 2019;44:793-818.
[19] Peng Z, Chen X, Yao L. Research status and future of hydrorelated sustainable complementary multi-energy power generation. Sustain Future 2021;3:100042.
[20] Rodriguez Correa C, Kruse A. Supercritical water gasification of biomass for hydrogen production - Review. J Supercrit Fluids 2018;133:573-590.
[21] Inayat A, Ahmad MM, Yusup S, Mutalib MIA, Khan Z. Biomass steam gasification for hydrogen production: a systematic review. Biomass Bioenergy Process Prop 2014;9783319076:329-343.
[22] Nikolaidis P, Poullikkas A. A comparative overview of hydrogen production process. Renewable and Sustainable Energy Reviews 2017;67:597-611.
[23] Rosen MA, Koohi-Fayegh S. The prospects for hydrogen as an energy carrier: an overview of hydrogen energy and hydrogen energy systems. Energy Ecol Environ 2016;1(1):10-29.
[24] Abe JO, Popoola API, Ajenifuja E, Popoola OM. Hydrogen energy, economy and storage: Review and recommendation. International journal of hydrogen energy 2019;44:15072-15086.
[25] DEMIRBAS FA. Storage and Transportation Opportunities of Hydrogen. Energy Sources Part B 2007;2:287-295.
[26] Megía PJ, Vizcaíno AJ, A.Calles J, Carrero A. Hydrogen Production Technologies: From Fossil Fuel toward Renewable Sources. A mini Review. Energy Fuels 2021;35:16403-16415.
[27] Stiegel J, Ramezan M. Hydrogen from Coal Gasification: An Economical Pathway to a Sustainable Energy Future. Int J Coal Geol 2006; 65 (3-4):173-190.
[28] Mularski J, Pawlak-Kruczek H, Modlinski N. A Review of Recent Studies of the CFD Modelling of Coal Gasification in Entrained Flow Gasifiers, Covering Devolatilization, Gas-Phase Reactions, Surface Reactions, Models and Kinetics. Fuel 2020; 271:117620.
[29] Dincer I, Acar C. Review and Evaluation of Hydrogen Production Methods for Better Sustainability. Int J Hydrogen Energy 2015;40(34):11094−11111.
[30] Niaz GS, Manzoor T, Pandith AH. Hydrogen storage: Materials, methods and perspectives. Renewable and Sustainable Energy Reviews 2015;50:457-469.

[31] Durbin DJ, Malardier-Jugroot C. Review of hydrogen storage techniques for on board vehicle applications. Int J Hydrogen Energy 2013;38:14595-145617.
[32] Zhang F, Zhao P, Niu M, Maddy J. The survey of key technologies in hydrogen energy storage. Int J Hydrogen Energy 2016;41:14535-14552.
[33] Jensen JO, Vestbø AP, Li Q, Bjerrum NJ. The energy efficiency of onboard hydrogen storage. J Alloys Compd 2007;446-447:723-728.
[34] Tarasov BP, Lototskii MV, Yartys VA. Problem of hydrogen storage and perspective uses of hydrides for hydrogen accumulation. Russ J Gen Chem 2007;77:694–711.
[35] Abdalla AM, Hossain S, Nisfindy OB, Azad AT, Dawood M, Azad AK. Hydrogen production, transportation and key challenges with applications: a review. Energy Convers Manag 2018;165:602–627.
[36] Barthelemy H, Weber M, Barbier F. Hydrogen storage: recent improvements and industrial perspectives. Int J Hydrogen Energy 2017;42:7254-7262.
[37] Harris R, Book D, Anderson P, Edwards P. Hydrogen storage, the grand challenge. Fuel Cell Rev 2004;1:17-23.
[38] Rivard E, Trudeau M, Zaghib K. Hydrogen Storage for Mobility: A Review. Materials 2019;12:1973.
[39] Jorgensen SW. Hydrogen storage tanks for vehicles: recent progress and current status. Curr Opin Solid State Mater Sci 2011;15:39-43.
[40] Wang Y, Yuan H, Martinez A, Hong P, Xu H, Bockmiller FR. Polymer electrolyte membrane fuel cell and hydrogen station networks for automobiles: status, technology, and perspectives. Adv Appl Energy 2021;2:100011.
[41] Preuster P, Alexander A, Wasserscheid P. Hydrogen storage technologies for future energy systems. Annu Rev Chem Biomol Eng 2017;8:445–471.
[42] Ahluwalia RK, Hua TQ, Peng J-K, Lasher S, McKenney K, Sinha J, Sinha J. Technical assessment of cryo-compressed hydrogen storage tank systems for automotive applications. Int J Hydrogen Energy 2010;35:4171-4184.
[43] Züttel A. Hydrogen storage methods. Naturwissenschaften 2004;91:157–172.
[44] Aceves SM, Espinosa-Loza F, Ledesma-Orozco E, Ross TO, Weisberg AH, Brunner TC, Kircher O. High-density automotive hydrogen storage with cryogenic capable pressure vessels. Int J Hydrogen Energy 2010;35:1219-1226.
[45] Schlapbach L, Zuttel A. Hydrogen-storage materials for mobile applications. Nature 2001;414:353-358.

[46] Sakintuna B, Lamari-Darkrim F, Hirscher M. Metal hydride materials for solid hydrogen storage: a review. Int J Hydrogen Energy 2007;32:1121–1140.
[47] Graetz J. New approaches to hydrogen storage. Chem Soc Rev 2009;38:73-82.
[48] Durbin DJ, Malardier-Jugroot C. Review of hydrogen storage techniques for on board vehicle applications. Int J Hydrogen Energy 2013;38:14595–14617.
[49] Prabhukhot PR, Wagh MM, Gangal AC. A review on solid state hydrogen storage material. Adv Energy Power 2016;4:11–22.
[50] Ren J, Musyoka NM, Langmi HW, Mathe M, Liao S. Current research trends and perspectives on materials-based hydrogen storage solutions: a critical review. Int J Hydrogen Energy 2017;42:289–311.
[51] Pasini JM, Corgnale C, van Hassel BA, Motyka T, Kumar S, Simmons KL. Metal hydride material requirements for automotive hydrogen storage systems. Int J Hydrogen Energy 2013;38:9755–9765.
[52] Zhou L. Progress and problems in hydrogen storage methods. Renew Sustain Energy Rev 2005;9:395–408.
[53] Jain LP, Lal C, Jain A. Hydrogen storage in Mg: a most promising material. Int J Hydrogen Energy 2010;35. 5133–5144.
[54] Zaluska A, Zaluski L, Strom-Olsen JO. Nanocrystalline magnesium for hydrogen storage. J Alloys Compd 1999;288:217-225.
[55] Wang Y. Recent advances in additive-enhanced magnesium hydride for hydrogen storage. Prog Nat Mater Int 2017;27:41-49.
[56] Bodanović B, Reiser A, Schlichte K, Spliethoff B, Tesche B. Thermodynamics and dynamics of the Mg-Fe-H system and its potential for thermochemical thermal energy storage. J Alloys Compd 2002;345:77-89.
[57] Johnson SR, Anderson PA, Edwards PP, Gameson I, Prendergast JW, et al. Chemical activation of MgH2; a new route to superior hydrogen storage materials. Chem Commun 2005;22:2823-2825.
[58] Bendyna JK, Dyjak S, Notten PHL. The influence of ball-milling time on the dehydrogenation properties of the NaAlH4-MgH2 composite. Int J Hydrogen Energy 2015;40:4200–4206.
[59] Møller KT, Sheppard D, Ravnsbæk DB, Buckey CE, Akiba E, Li H-W, Jensen TR. Complex metal hydrides for hydrogen, thermal and electrochemical energy storage. Energies 2017;10:1645.

[60] Zhang Y, Tian Q-F, Liu S-S, Sun L-X. The destabilization mechanism and de/ rehydrogenation kinetics of $MgH_2$-$LiAlH_4$ hydrogen storage system. J Power Sources 2008;185:1514-1518.

[61] Dornheim M. Tailoring reaction enthalpies of hydrides. In: Hirscher M, editor. Handbook of hydrogen storage: new materials for future energy storage. Weinheim: Wiley-VCH 2010:187-214.

[62] Rafi-ud-Din, Xuanhui Q, Ping L, Zhang L, Ahmad M, Iqbal MZ, et al. Enhanced hydrogen storage performance for $MgH_2$-$NaAlH_4$ system - the effects of stoichiometry and $Nb_2O_5$ nanoparticles on cycling behavior. RSC Adv 2012;2:4891-4903.

[63] Dornheim M, Klassen T. High temperature hydrides. In: Garche J, Dyer CK, Mosely PT, Ogumi Z, Rand DAJ, Scrosati B, editors. Encyclopedia of electrochemical power sources. New York: Academic Press;2009:459-472.

[64] Jain A, Agarwal S, Ichikawa T. Catalytic Tuning of sorption kinetics of lightweight hydrides: a review of the materials and mechanism. Catalysts 2018;8:651.

[65] Bodanović B, Felderhoff M, Streukens G. Hydrogen storage in complex metal hydrides. J Serb Chem Soc 2009;74:183-196.

[66] Ashby EC, Kobetz P. The direct synthesis of $Na_3AlH_6$. Inorg Chem 1966;5:1615-1617.

[67] Orimo S-I, Nakamori Y, Eliseo JR, Züttel A, Jensen CM. Complex hydrides for hydrogen storage. Chem Rev 2007;107:4111-4132.

[68] Rusman NAA, Dahari M. A review on the current progress of metal hydrides material for solid-state hydrogen storage applications. Int J Hydrogen Energy 2016;41:12108-12126.

[69] Barkhodarian G, Klassen T, Dornheim M, Bormann R. Unexpected kinetic effect of $MgB_2$ in reactive hydride composites containing complex borohydrides. J Alloys Compd 2007;440:L18-L21.

[70] Bodanović B, Schwickardi M. Ti-doped alkali metal aluminum hydrides as potential novel reversible hydrogen storage materials. J Allys Compd 1997;253-254:1-9.

[71] Ismail M, Zhao Y, Yu XB, Mao JF, Duo SX. The hydrogen storage properties and reaction mechanism of the $MgH_2$-$NaAlH_4$ composite system. Int J Hydrogen Energy 2011;36:9045-9050.

[72] Ismail M, Zhao Y, Yu XB, Duo SX. Improved hydrogen storage performance of $MgH_2$-$NaAlH_4$ composite by addition of $TiF_3$. Int J Hydrogen Energy 2012;37:8395-8401.

[73] Züttel A, Wenger P, Rentsch S, Sudan P, Mauron Ph, Emmenegger Ch. $LiBH_4$ a new hydrogen storage material. J Power Sources 2003;118:1-7.

[74] Lu Z-H, Xu Q. Recent progress in boron - and nitrogen-based chemical hydrogen storage. Func Mater Lett 2012;5:1230001-1-1230001-9.

[75] He T, Cao H, Chen P. Complex hydrides for energy storage, conversion, and utilization. Adv Mater 2019;31:1-19.
[76] Møller KT, Jensen TR, Akiba E, Li H-W. Hydrogen - A sustainable energy carrier. Prog Nat Sci-Mat 2017;27:34-40.
[77] Lim KL, Kazemian H, Yakoob Z, Daud WRW. Solid-state materials and methods for hydrogen storage: a critical review. Chem Eng Technol 2010;33-213-226.
[78] Zhou L, Zhou YP, Sun Y. Enhanced storage of hydrogen at the temperature of liquid nitrogen. Int J Hydrogen Energy 2004;29:319-322.
[79] Zhao T, Ji X, Jin W, Yang W, Li T. Hydrogen storage capacity of single-walled carbon nanotube prepared by a modified arc discharge. Fullerenes, Nanotub Carbon Nanostruct 2017;25:355-358.
[80] Liu C, Chen Y, Wu C-Z, Xu S-T, Cheng H-M. Hydrogen storage in carbon nanotubes revisited. Carbon 2010;48:452-455.
[81] Langmi HM, Book D, Walton A, Johnson SR, Al-Mamouri MM, Speight JD, Edwards PP, Harris IR, Anderson PA. Hydrogen storage in ion-exchanged zeolites. J Alloys Compd 2005;404-406:637-642.
[82] Du XM, Wu ED. Physisorption of hydrogen in A, X and ZSM-5 types of zeolites at moderately high pressures. Chin J Chem Phys 2006;19:457-2.
[83] Langmi HW, Ren J, North B, Mathe M, Bessarabov D. Hydrogen storage in metal-organic frameworks: a review. Electrochim Acta 2014;128:368-392.
[84] Li H, Eddaoudi M, O'Keeffe M, Yaghi OM. Design and synthesis of an exceptionally stable and highly porous metal-organic framework. Nature 1999; 402:276-279.
[85] Farha OK, Yazaydın A¨O, Eryazici I, Malliakas CD, Hauser BG, Kanatzidis MG, Nguyen ST, Snurr RQ, Hupp JT. De novo synthesis of a metal-organic framework material featuring ultrahigh surface area and gas storage capacities. Nat Chem 2010;2:944-948.

# Chapter II: Density functional theory, calculation methods and WIEN2k code

## II.1 Introduction

As a complement to experimental examinations of matter, computer modeling has become nearly vital in the field of materials science. It does so by giving researchers atomic-level understanding of ever-more complicated materials and processes [1]. The availability of broad and trustworthy ab initio electronic structure approaches that do not rely on system-specific factors is necessary due to the rising industrial need for new materials with structural and electronic properties suitable for particular applications. Such methods have undergone an extraordinary transformation over the past three decades, and they are now a crucial part of research in the fields of solid-state chemistry, condensed matter physics and materials science, where they are increasingly used to both interpret the results of previous experiments and to guide brand-new ones [1].

An effective and frequently used quantum mechanical tool for examining numerous features of matter is density functional theory (DFT). The study in this area covers a broad spectrum, from the creation of original analytical methods centered on the creation of precise exchange-correlation functional to the application of this method to forecast the molecular and electronic configuration of atoms, molecules, complexes and solids in both gas and solution phases. The search for the exchange-correlation functional, which makes use of density to represent complex many-body processes inside an element formalism, is what led to the development of DFT.

The quantum nature of matter might be accurately described if a precise exchange-correlation functional is used. The estimated exchange-correlation functional's nature determines whether a DFT implementation is successful or unsuccessful. In order to set the groundwork for DFT, which is being used to investigate innovative materials, Hohenberg-Kohn proved that every state of a system in its ground state is a distinct functional of its density [2].

The purpose of this chapter is to give a general understanding of DFT, calculating techniques and the WIEN2k code.

## II.2 Hamiltonian

A solid system is composed from nuclei (heavy and positively charged particles) and electrons (light and negatively charged particles). Both nuclei and electrons are in motion and in interaction with each other. This is a quantum many-body problem since the particles are so light that quantum mechanics is needed. The exact many-particle hamiltonian for this system is:

$$\hat{H} = -\frac{\hbar^2}{2}\sum_i \frac{\nabla^2_{\vec{R}_i}}{M_i} - \frac{\hbar^2}{2}\sum_i \frac{\nabla^2_{\vec{r}_i}}{m_e} - \frac{1}{4\pi\epsilon_0}\sum_{i,j}\frac{e^2 Z_i}{|\vec{R}_i - \vec{r}_j|} + \frac{1}{8\pi\epsilon_0}\sum_{i\neq j}\frac{e^2}{|\vec{r}_i - \vec{r}_j|} + \frac{1}{8\pi\epsilon_0}\sum_{i\neq j}\frac{e^2 Z_i Z_j}{|\vec{R}_i - \vec{R}_j|}. \quad \text{(II.1)}$$

The first and the second terms are kinetic energy operators for the nuclei and the electrons, respectively. The nucleus has a mass of $M_i$ at $\vec{R}_i$ and the electrons have a mass of $m_e$ at $\vec{r}_i$. The interaction between electrons and nuclei, between electrons and other electrons and between nuclei and other nuclei are described in the respective three last terms.

## II.3 Born-Oppenheimer approximation

The Schrödinger equation's solution is simplified using a number of approximations, the first of which is the Born-Oppenheimer approximation. By distinguishing between nuclear and electronic motions, it simplifies the overall molecular problem [3]. As the mass of a nucleus is often millions of times greater than that of an electron, this approximation is reasonable. The electrons respond almost instantly to changes in nuclear location because they move much more slowly than nuclei do. As a result, rather than the nuclei's velocities, the electron distribution inside a molecular system depends on the locations of the nuclei.

To put it another way, electron motion can be thought of as taking place in a field of fixed nuclei since the nuclei appear fixed to the electrons. The first term vanishes, the nuclei stop moving and their kinetic energy is zero (see the Hamiltonian equation above). The final component becomes a constant which is supposed equal to zero. We are left with the potential energy resulting from electron-electron interactions, the potential energy of the electrons in the (now external) potential of the nuclei and the kinetic energy of the electron gas. The following is how the Hamiltonian equation is expressed:

$$\hat{H} = \hat{T} + \hat{V} + \hat{V}_{ext}. \quad \text{(II.2)}$$

The first and the second terms are adequate for describing the electrons system. The third term describes the interaction between the electrons cloud and the external nuclear potential.

## II.4 Density functional theory (DFT)

The quantum many body problem is converted, using the Born-Oppenheimer approximation, to a dependent electrons system subjected to an external nuclear potential, which is still far too difficult to solve. The Hartree-Fock method is among several methods used to simplify equation (II.2) which describes effectively atoms and molecules. The more powerful method

which is called Density Functional Theory (DFT) is more modern compared to the HF method. DFT has been forged in 1964 by two theorems introduced by Hohenberg and Kohn [4].

### II.4.1 Theorems of Hohenberg and Kohn

**"First theorem:** There is a one-to-one correspondence between the ground-state density $\rho(\vec{r})$ of a many-electron system (solid) and the external potential $V_{ext}$. An immediate consequence is that the ground-state expectation value of any observable $\hat{O}$ is a unique functional of the exact ground-state electron density" [4]:

$$\langle\psi|\hat{O}|\psi\rangle = O[\rho]. \tag{II.3}$$

**"Second theorem:** For $\hat{O}$ being the Hamiltonian $\hat{H}$, the ground-state total energy functional $H[\rho] = E_{Vext}[\rho]$ is of the form" [4] :

$$E_{Vext}[\rho] = \langle\psi|\hat{T} + \hat{V}|\psi\rangle + \langle\psi|\hat{V}_{ext}|\psi\rangle = F_{HK}[\rho] + \int \rho(\vec{r})\, V_{ext}(\vec{r}) d\vec{r}, \tag{II.4}$$

where $F_{HK}[\rho]$ is the Hohenberg-Kohn density functional which is universal and restricted only to describe a many electron system.

### II.4.2 Kohn-Sham equations

The equations of Kohn and Sham were published in 1965 [5]. These equations are very important equations to extract correlation and exchange contributions from a dependent-electrons gas. The correlation energy functional $V_c$ is defined as the difference in kinetic energy functional between an interacting and a non-interaction electron gas:

$$V_c = T - T_0, \tag{II.5}$$

where $T$ and $T_0$ are the exact kinetic energy functional for a dependent-electrons gas and the kinetic energy functional for an independent-electrons gas respectively.

The exchange energy functional $V_x$ is defined as the difference in potential energy functional between an interacting and a non-interaction electron gas:

$$V_x = V - V_H, \tag{II.6}$$

where $V$ and $V_H$ are the exact potential energy functional for a dependent-electrons gas and the Hartree potential energy functional for an independent-electrons gas respectively.
The Hohenberg-Kohn functional is written as follows:

$$F_{HK} = T + V = T_0 + V_H + V_c + V_x = T_0 + V_H + V_{xc}. \quad \text{(II.7)}$$

$V_{xc}$ is the exchange-correlation energy functional. The ground state density can now be calculated using the second Hohenberg-Kohn theorem. Due to the nuclei, exchange and correlation contributions, the electron gas system transforms into a classical, non-interacting electron gas that is susceptible to external potentials. The Kohn-Sham Hamiltonian takes then the following form:

$$\hat{H}_{KS} = \hat{T}_0 + \hat{V}_H + \hat{V}_{xc} + \hat{V}_{ext}. \quad \text{(II.8)}$$

The functional derivative provides the exchange-correlation potential:

$$\hat{V}_{xc} = \frac{\delta V_{xc}[\rho]}{\delta \rho}. \quad \text{(II.9)}$$

Now, the Kohn and Sham theorem can be expressed in the following way.
An N-electron system's precise ground-state density is:

$$\rho(\vec{r}) = \sum_{i=1}^{N} \phi_i^*(\vec{r})\, \phi_i(\vec{r}), \quad \text{(II.10)}$$

where the single-particle wave functions $\phi_i(\vec{r})$ are the N lowest-energy solutions of the Kohn Sham equation:

$$\hat{H}_{KS}\phi_i = \epsilon_i \phi_i \quad \text{(II.11)}$$

The $\hat{V}_H$ and $\hat{V}_{xc}$ terms vary with the density $\rho(\vec{r})$ which depends on the $\phi_i$. This creates a self-consistency issue because the original equation ($V_H$ and $V_{xc}$ in $H_{KS}$) is determined by the solves $\phi_i$, and the equation cannot be expressed and solved before its solution is known.To escape from this paradox an iterative procedure is required (Fig. II.1).

This procedure is started by a guessed density $\rho_0$ from which a hamiltonian $H_{KS1}$is devised. The eigenvalue problem is solved, and results in a set of $\phi_1$ from which a density $\rho_1$ can be derived. In most cases, the initial $\rho_0$ will differ from the calculated $\rho_1$. This $\rho_1$ is then used to construct $H_{KS2}$, which will yield a new value $\rho_2$, etc. The procedure can be set up in such a way that this series will converge to a final density $\rho_f$which generates a $H_{KSf}$ which yields as solution $\rho_f$ again: this final density is then consistent with the Hamiltonian.

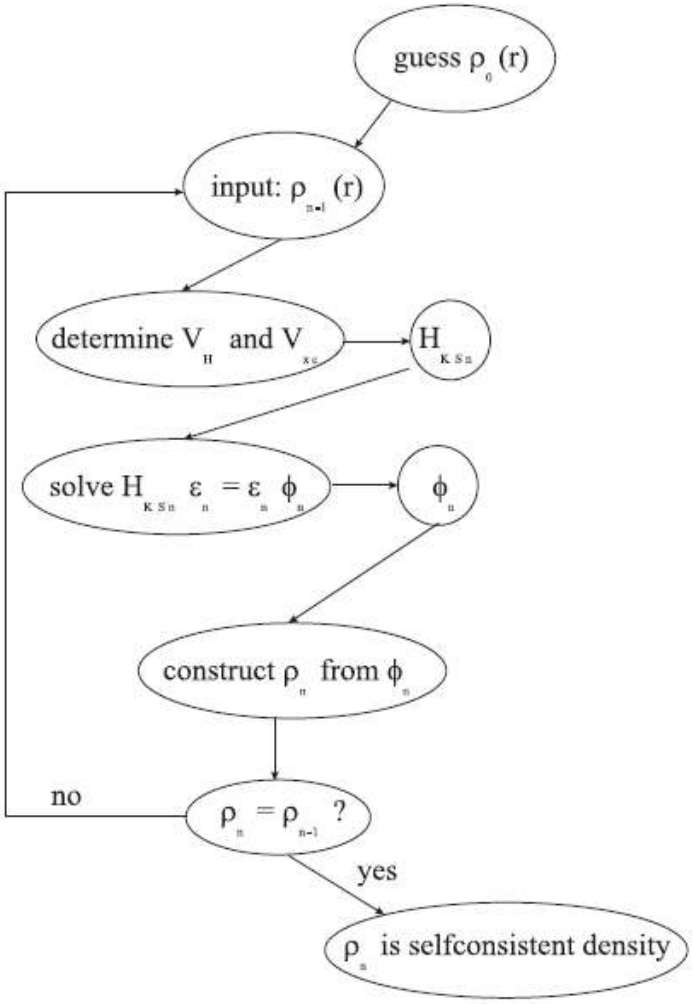


**Figure II.1:** The n[th] iteration in the self-consistent procedure to solve Kohn-Sham equations.

## II.3.2 Exchange-correlation functional

An approximation should be set about the exchange-correlation functional which is unknown. The exchange-correlation functional of a common approximation known as the Local Density Approximation (LDA) takes the following form:

$$E_{xc}^{LDA} = \int \rho(\vec{r})\epsilon_{xc}(\rho(\vec{r}))d\vec{r} \quad \text{(II.12)}$$

In LDA, the material is locally partitioned to infinitesimally small volumes with a constant density. Each volume contributes an amount equal to the exchange-correlation energy of a volume filled with a homogeneous electron gas to the overall exchange-correlation energy. The next improvement to LDA is to make each infinitesimal volume's exchange-correlation contribution dependent on both its surrounding volumes' densities as well as its own local density. This approximation is called the Generalized Gradient Approximation (GGA) which exists in several versions.

## II.4 Solving the equations

Based on the DFT approximation and an infinite base set, the Schrödinger equations for one electron are given as follows:

$$\widehat{H}_{sp}\phi_m(\vec{r}) = \left(-\frac{\hbar^2}{2m_e}\vec{\nabla}_{\mathrm{m}}^2 + \frac{\mathrm{e}^2}{4\pi\epsilon_0}\int\frac{\rho(\vec{r})}{|\vec{r}-\vec{r}'|}d\vec{r}' + V_{xc} + V_{ext}\right)\phi_m(\vec{r}) = \epsilon_m\phi_m(\vec{r}), \quad \text{(II.13)}$$

where $m$ is an integer number that counts the members of the set. $\widehat{H}_{sp}$ is the single-particle Hamiltonian and the $\phi_m$ are single-particle orbitals (states). Solving the equations means finding the coefficients $c_p^m$ needed to express $\phi_m$ in a given basis set $\phi_p^b$:

$$\phi_m = \sum_{p=1}^{\boldsymbol{P}} c_p^m\,\phi_p^b. \quad \text{(II.14)}$$

The *P* index is in principle infinite and leads the wave functions to an infinite dimension. Having chosen a basis and hence a finite ***P*** value can take the equation (II.13) to an eigenvalue problem. Diagonalization of the Hamiltonian matrix will lead to ***P*** eigenvalues and ***P*** eigenfunctions in the chosen basis.

## II.5 Calculation methods

Calculation methods are based on the basis set used in the computations. The very important requirements for a basis set to be more practical in which we want to expand the eigenstates of the solid state Hamiltonian: the basis set should be **unbiased** (it should not in a hidden way force

the solution into a built-in direction i.e. it does not assume any preconceptions in the form of the problem) and **efficient** (dimension of the basis set should be as low as possible).

### II.5.1 Pseudopotential method

The basis set used in this method is the plane wave which is simple, unbiased and independent of atomic positions. The theorem of Bloch says that any eigenfunction $\psi_{\vec{k}}^{n}$ of a periodic Hamiltonian can be expressed exactly in the plane basis set by means of an infinite set of coefficients $c_{\vec{K}}^{n,\vec{k}}$:

$$\psi_{\vec{k}}^{n}(\vec{r}) = \sum_{\vec{K}} c_{\vec{K}}^{n,\vec{k}} e^{i(\vec{k}+\vec{K}).\vec{r}} = \sum_{\vec{K}} c_{\vec{K}}^{n,\vec{k}} \phi_{\vec{K}}^{\vec{k}}(\vec{r}), \qquad \text{(II.15)}$$

where $\vec{k}$ is a vector in the first Brillouin zone, $\vec{K}$ is a reciprocal lattice vector and $n$ indicates the number of the Brillouin zone (also called the band index). One basis set for $\psi_{\vec{k}}^{n}(\vec{r})$ is:

$$\phi_{\vec{K}}^{\vec{k}}(\vec{r}) = \left|\vec{K}\right\rangle = e^{i(\vec{k}+\vec{K}).\vec{r}} \qquad \text{(II.16)}$$

All eigenstates $\psi_{\vec{k}}^{n}(\vec{r})$ that have the same k but a different n will be expressed in the basis set with this specific value of k. This basis set is $\vec{k}$-dependent. A different basis set utilizing that other $\vec{k}$ must be employed for eigenstates with another $\vec{k}$. In practice such an infinite basis set is not welcome and one should be limiting this basis set to all $\vec{K}$ with $K \leq K_{max}$.
This is equivalent to a sphere of radius $K_{max}$ that is centered at the reciprocal space origin. The basis set includes all reciprocal lattice vectors contained within this sphere.
Because rather than $K_{max}$,, the cut-off energy- also known as the free electron energy - corresponding to $K_{max}$ is frequently specified:

$$E_{cut} = \frac{\hbar^2 K_{max}}{2m_e} \qquad \text{(II.17)}$$

The hamiltonian matrix can be diagonalized to provide $P$ eigenvalues and $P$ sets of coefficients, each of which expresses a different $P$ eigenfunction in the given basis with the same $\vec{k}$ band index. The eigenfunction approximation improves with increasing $P$, although diagonalizing the Hamiltonian matrix takes longer. This process has to be repeated for many $\vec{k}$-points that are in

the first Brillouin zone and is needed for a dense enough sample. The plane wave basis set needs a few plane waves to be efficient. In the areas close to the nucleus, the number of the plane waves is too high, which is much more powerful than even supercomputers. The potential in these interior areas can therefore be replaced with a pseudopotential that is continuous and evolves to the true potential in the outer regions of atoms [6]. Two criteria are used to judge whether the pseudopotential method is good: softness and transferability. A pseudopotential is called soft when just a few plane waves are needed. It is called transferable when it can be used in various environments (molecule, cluster, solid, surface, insulator, metal, …).

### II.5.2 Augmented Plane Wave (APW) method

The search for a basis set that does not introduce a pseudopotential and uses functions other than plane waves. This basis set will have to be more efficient and unbiased. The first example basis set will be the Augmented Plane Wave (APW) [7]. The APW method itself has no practical use anymore today but, for didactical reasons, it is useful to discuss the APW method first, before going to its successors, the LAPW and APW+lo methods. In the APW basis set, the space is divided into two regions: around each atom a sphere (let's call it $S_\alpha$) with radius $R_\alpha$ is called a muffin tin sphere. The part of space occupied by the spheres is the muffin tin region, the remaining space outside the spheres is called the interstitial region (let's call it $I$) (see Fig II.2).

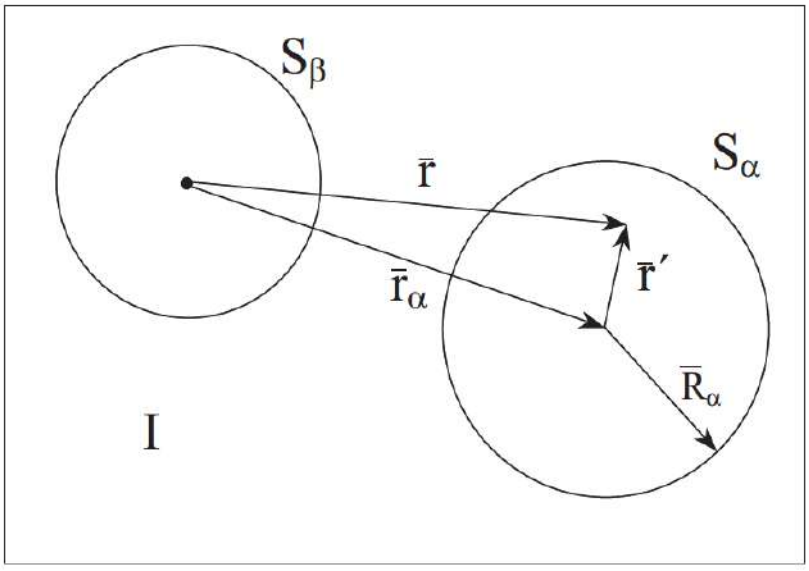


**Figure II.2:** A unit cell of a case with two atoms divided in muffin tin regions and interstitial region.

The expansion of $\psi_{\vec{k}}^{n}(\vec{r})$ in the APW basis set is defined by:

$$\phi_{\vec{K}}^{\vec{k}}(\vec{r},E)=\begin{cases}\frac{1}{\sqrt{V}}e^{i(\vec{k}+\vec{K}).\vec{r}} & \vec{r}\in I\\ \sum_{\ell,m}A_{\ell m}^{\alpha,\vec{k}+\vec{K}}\;u_{\ell}^{\alpha}(r',E)\;Y_{m}^{\ell}(\hat{r}') & \vec{r}\in S_{\alpha}\end{cases} \qquad \text{(II.18)}$$

The symbols $\vec{k}$, $\vec{K}$ and $\vec{r}$ keep their usual meaning, $.V$ is the unit cell volume. The APW basis set is $\vec{k}$-dependent. The position inside the spheres is given with respect to the center of each sphere by $\vec{r}'=\vec{r}-\vec{r}_{\alpha}$ (Fig. II.3). Spherical coordinates used are $\vec{r}'$ and $\hat{r}'$ (which indicating the angles $\theta'$ and $\varphi'$ of the direction $\vec{r}'$). The $A_{\ell m}^{\alpha,\vec{k}+\vec{K}}$ are yet undetermined parameters, as is $E$. The latter has the dimension of energy. The $Y_{m}^{\ell}(\hat{r}')$ are spherical harmonics. The $u_{\ell}^{\alpha}(r',E)$ are solutions to the radial part of the Schrodinger equation for a free atom $\alpha$ at the energy $E$. In order to describe an eigenstate $\psi_{\vec{k}}^{n}(\vec{r})$ accurately with APW basis set, one has to set $E$ equal to eigenvalue (or band enegy) $\epsilon_{\vec{k}}^{n}$ of that state. Due to the $E$, the diagonalization of the Hamiltonian in the APW basis set is needed for every eigenvalue, while with a plane wave one eigenvalue is found by single diagonalization. This makes the APW method inherently slow, much slower than the pseudopotential method.

### II.5.3 Linearized Augmented Plane Wave (LAPW) method

To calculate the electronic structure of crystals, one of the most accurate techniques is the linearized augmented plane wave (LAPW) method. For the treatment of exchange and correlation, it is based on density functional theory and employs techniques like the local spin density approximation (LSDA). The literature has several types of LSDA potentials, but more recent enhancements utilizing the generalized gradient approximation (GGA) are also accessible [11-14]. In order to describe, in LAPW basis set, the $\psi_{\vec{k}}^{n}(\vec{r})$ that has a predominating $p$-charater ($l=1$) for atom $\alpha$, it is better to choose $E$ near the center of the $p$–band. This argument can be repeated for every physically important (s, p, d and f states) and for every atom. The final definition of a LAPW basis set is:

$$\phi_{\vec{K}}^{\vec{k}}(\vec{r})=\begin{cases}\frac{1}{\sqrt{V}}e^{i(\vec{k}+\vec{K}).\vec{r}} & \vec{r}\in I\\ \sum_{\ell,m}\left(A_{\ell m}^{\alpha,\vec{k}+\vec{K}}\;u_{\ell}^{\alpha}\left(r',E_{1,\ell}^{\alpha}\right)+B_{\ell m}^{\alpha,\vec{k}+\vec{K}}\;\dot{u}_{\ell}^{\alpha}\left(r',E_{1,\ell}^{\alpha}\right)\right)Y_{m}^{\ell}(\hat{r}') & \vec{r}\in S_{\alpha}\end{cases} \qquad \text{(II.19)}$$

With the $E_{1,\ell}^{\alpha}$ being fixed, the basis functions can be calculated once and for all as used for the plane wave basis set. One digonalization will yield $P$ different band energies for this $\vec{k}$.

The plane wave basis set and LAPW basis set do not have the same criteria for the accuracy. The accuracy of the plane wave basis set was determined by $K_{max}$, while the LAPW one was by the product $R_{\alpha}^{min}K_{max}$ between the smallest muffin tin radius and $K_{max}$. If the smallest muffin tin radius is increased, less plane waves are needed.

$K_{max}$ can be decreased and it is a good idea to keep the product $R_{\alpha}^{min}K_{max}$ constant to maintain equal accuracy. Because matrix diagonalization is very expensive, decreasing $K_{max}$ entails decreasing the size of the matrices, which can result in a significant reduction in calculation time. On the other hand, $R_{\alpha}^{min}$ cannot be too large since the wave functions in the region far from the nucleus cannot be described by spherical harmonics.

### II.5.4 Linearized Augmented Plane Wave + Local Orbital (LAPW+LO) method

Which electron states are calculated using the LAPW approach has not yet been made clear.. There are some electrons extremely well bound to the nucleus and will behave almost as if they were in free atoms. Such states are called core states. One atom's core state needs to be completely contained inside the muffin tin sphere since it cannot interact chemically with other atoms directly. There are also states leaking out of the muffin tin sphere, called valence states which participate in chemical bonds. LAPW deals with valence states. Core states are handled as if they were free atoms, yet they are susceptible to the outside potential that originated in the valence states. According to this definition all states having the same *l* but a different principal quantum number *n* are treated as valence states. Therefore, it results in a problem of the chosen value of $E_{1,\ell}^{\alpha}$ as indicated in LAPW basis set. The valence states can be divided to low-lying states, called valence semi-core states, and upper-lying states, called valence states. In some cases, we found two states close to each other one in valence semi-core states and the other in valence states (upper states) having the same *l*-character but a different *n*. Hence, a dilemma was created as to which $E_{1,\ell}^{\alpha}$ is chosen for the lower or the upper valence state. This dilemma is solved by adding another type of basis function to the LAPW basis set, called a local orbital (LO) [8]. A local orbital is defined as:

$$\phi_{\alpha,LO}^{\ell m}(\vec{r}) = \begin{cases} 0 & \vec{r} \notin S_{\alpha} \\ \sum_{\ell,m}\left(A_{\ell m}^{\alpha,LO}u_{\ell}^{\alpha}(r',E_{1,\ell}^{\alpha}) + B_{\ell m}^{\alpha,LO}\dot{u}_{\ell}^{\alpha}(r',E_{1,\ell}^{\alpha}) + C_{\ell m}^{\alpha,LO}u_{\ell}^{\alpha}(r',E_{2,\ell}^{\alpha})\right) Y_{m}^{\ell}(\hat{r}') & \vec{r} \in S_{\alpha} \end{cases} \quad \text{(II.20)}$$

The local basis set is defined for a particular *l* and *m* and for a particular atom $\alpha$. In the muffin tin sphere of atom $\alpha$, $u_\ell^\alpha\left(r', E_{1,\ell}^\alpha\right)$ and $\dot{u}_\ell^\alpha\left(r', E_{1,\ell}^\alpha\right)$ are used as in the LAPW basis set, with a linearization energy $E_{1,\ell}^\alpha$ a value suitable for the highest of the valence states. The lower valence state is treated by a single radius function $u_\ell^\alpha\left(r', E_{2,\ell}^\alpha\right)$ at the energy $E_{2,\ell}^\alpha$. Local orbitals have no $\vec{k}$--dependence because they are not associated with plane waves in the interstitial region. The LAPW basis set size is increased by including local orbitals. Local orbitals are usually employed since the little longer computation time is a minor price to pay for the significantly greater precision they provide.

### II.5.5 Augmented Plane Wave + local orbital (APW+lo) method

The basis set will continue to be the same size and be energy independent in the APW+lo approach. Thus, APW+lo combines the positive aspects of APW and LAPW+LO. There are two types of functions in the APW+lo basis set. First, there are APWs, which have a predetermined set of energies $E_{1,\ell}^\alpha$ :

$$\phi_{\vec{K}}^{\vec{k}}(\vec{r}) = \begin{cases} \frac{1}{\sqrt{V}} e^{i(\vec{k}+\vec{K}).\vec{r}} & \vec{r} \in I \\ \sum_{\ell,m} A_{\ell m}^{\alpha,\vec{k}+\vec{K}}\ u_\ell^\alpha\left(r', E_{1,l}^\alpha\right) Y_m^\ell\left(\hat{r}'\right) & \vec{r} \in S_\alpha \end{cases} \qquad \text{(II.21)}$$

Local orbitals, the second category of functions, come in a different variety from the one associated with the LAPW approach. These functions are described as follows:

$$\phi_{\alpha,lo}^{\ell m}(\vec{r}) = \begin{cases} 0 & \vec{r} \notin S_\alpha \\ \sum_{\ell,m}\left(A_{\ell m}^{\alpha,lo} u_\ell^\alpha\left(r', E_{1,\ell}^\alpha\right) + B_{\ell m}^{\alpha,lo} \dot{u}_\ell^\alpha\left(r', E_{1,\ell}^\alpha\right)\right) Y_m^\ell\left(\hat{r}'\right) & \vec{r} \in S_\alpha \end{cases} \qquad \text{(II.22)}$$

The APW+lo basis set appears to need a size that is less than in the LAPW+LO approach and comparable to the APW method in order to get correct results.

### II.5.6 Mixed LAPW/APW+lo basis set

There are a few states which can be treated by the APW+lo method, but hard for the LAPW one. These are:

- The d- and f-states of valence
- Atomic states with muffin-tin-sized spheres that are significantly smaller than those of other spheres in the unit cell.

When using APW+lo as a state, this basis is increased by 2l+1 local orbitals per atom. The latter will become for the same $R_{\alpha}^{min}K_{max}$ considerably larger than the LAPW basis set, but useful for exceptional states (mentioned above). Such a technique is very effective in a mixed basis set of LAPW/APW+lo: Equation II.19 is utilized for atoms and values l [9, 10]. With **WIEN2k**, such a mixed basis set is the suggested option.

## II.6 WIEN2k package

The WIEN2k package is made up of a number of separate Fortran 90 (F90) routines that are connected by C-shell scripts. The WIEN2k is based on the Full Potential (FP) and the Linearized Augmented Plane Wave (LAPW) method which is one of the most precise approaches in density functional theory for computing the electronic structure of solids. The first copyrighted version was called **WIEN** and it was published by: P. Blaha, K. Schwartz, P. Sorantin and S. B. Trickey, in Comput. Phys. Commun. 59 (1990) 399. The newest version of this code is WIEN2k edition 2021. Each "case" runs in his own directory (./case). The master input file is called (case.struct). Fig. II.3 shows how the various programs operate and flow.

### II.6.1 Initialization programs

"Execution initialize calc." is used to initialize the computation after the basic input file has been produced. Running a number of quick auxiliary programs that produce the inputs for the main programs constitutes initialization. The upper part of Fig. II.3 shows the programs of the initialization. One begins by defining the master file **case.struct** in the corresponding **Case**/subdirectory. Initialization entails starting:

**NN:** a program that helps in calculating the atomic sphere radii by showing the nearest neighbor distances up to a defined limit. Also, it is a very helpful extra check of your **case. struct** file (equivalency of atoms).

**SGROUP:** decides what spacegroup the structure in the **case.struct** file belongs to.

**SYMMETRY:** a raw **case. struct** file is used to generate. The local rotation matrices, point groups for each individual atomic site, LM expansion for the lattice harmonics and space group symmetry operations are all determined by the struct file.

**LSTART:** creates free atomic densities and decides whether to treat the various orbitals as core or band states, with or without orbitals, in band structure computations.

**KGEN:** creates a k-mesh in the Brillouin zone's irreducible region.

**DSTART:** creates a beginning density for the SCF cycle by superimposing the LSTART-

generated atomic densities.

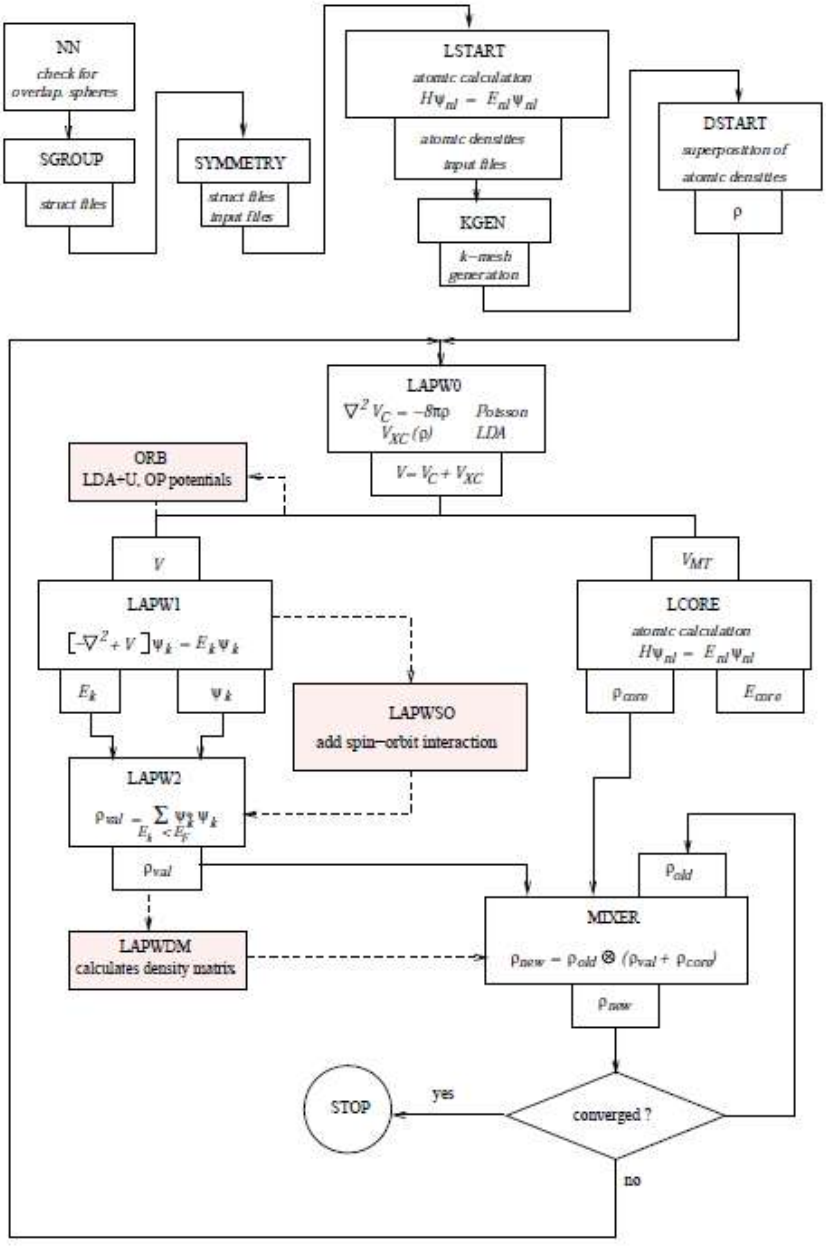


**Figure II.3:** Programs flow in WIEN2k.

The table II.1 describes input and output files for initialization programs.

**Table II.1:** Input and output files of the initialization programs.

| Program | Needs | | Generates | |
|---|---|---|---|---|
| | **necessary** | **optional** | **necessary** | **optional** |
| **NN** | nn.def<br>case.struct | | case.outputnn | case.struct_nn |
| **SGROUP** | case.struct | | case.outputsgroup | case.struct_sgroup |
| **SYMMETRY** | Symmetry.def<br>case.struct | case.in2_st | case.outputs<br>case.in2_st | case.struct_st |
| **LSTART** | lstart.def<br>case.struct<br>case.inst | | case.outputst<br>case.rsp<br>case.in0_st<br>case.in1_st<br>case.in2_st<br>case.inc_st<br>case.inm_st<br>case.inm_restart | case.rspup/dn<br>case.rsigma<br>case.vsp_st<br>case.vspdn_st<br>case.sigma<br>case.potup/dn<br>case.sptup/dn |
| **KGEN** | Kgen.def<br>case.struct | case.ksym | case.outputkgen<br>case.klist<br>case.kgen | |
| **DSTART** | dstart.def<br>case.struct<br>case.rsp(up)<br>case.in0<br>case.in1<br>case.in2 | case.inpd | case.outputd<br>case.clmsum (up)<br>dstart.error<br>case.in0_std | new_super.clmsum(up)<br>case.clmsc(up)<br>case.r2v_half(dn) |

### II.6.2 Self-Consistent Field (SCF) cycle programs

It starts the self-consistent field cycle and keeps going till the convergence criteria are satisfied. (lower part of Fig. II.3). The **run-lapw** script can be used to start this cycle, which goes through the following steps:

**LAPW0:** Potential is created from density by (POTENTIALS).

**LAPW1:** (BANDS) determines the valence bands (eigenvalues and eigenvectors).

**LAPW2:** Valence densities are calculated via (RHO) using eigenvectors.

**LCORE:** computes the core densities and states.

**MIXER:** input and output densities are combined

Table II.2 describes input and output files for SCF cycle programs.

**Table II.2:** Input and output files of the SCF cycle programs.

| Program | Needs | | Generates | |
|---|---|---|---|---|
| | **necessary** | **optional** | **necessary** | **optional** |
| **LAPW0** | lapw0.def<br>case.struct<br>case.in0<br>case.clmsum | case.clmup/dn<br>case.vrespsum/up/dn<br>case.inm<br>case.r2v_half(dn) | case.output0<br>case.scf0<br>case.vsp(up/dn)<br>case.vns(up/dn) | case.r2v<br>case.vcoul<br>case.vtotal |
| **LAPW1** | lapw1.def<br>case.struct<br>case.in1<br>case.vsp<br>case.klist | case.vns<br>case.vorb<br>case.vector.old | case.output1<br>case.scf1<br>case.vector<br>case.energy | case.nsh(s)<br>case.nmat_only |
| **LAPW2** | Lapw2.def<br>case.struct<br>case.in2<br>case.vector<br>case.vsp<br>case.energy | case.kgen<br>case.nsh<br>case.weight<br>case.recprlist | case.output2<br>case.scf2<br>case.clmval | case.qtl<br>case.weight<br>case.help03*<br>case.vrespval<br>case.almblm<br>case.radwf<br>case.dmat |
| **LCORE** | lcore.def<br>case.struct<br>case.inc<br>case.vsp | Case.vns | case.outputc<br>case.scfc<br>case.clmcor<br>lcore.error | case.corewf |
| **MIXER** | mixer.def<br>case.struct<br>case.inm<br>case.clmval<br>case.inc | case.clmsum_old<br>case.clmsc<br>case.clmcor<br>case.scf<br>case.broyd1<br>case.broyd2<br>case.dmat | case.outputm<br>case.scfm<br>mixer.error | case.broyd* |
| After **MIXER** the file **case.scfm** is appended to **case.scf**, so that after an iteration is completed, the two essential files are **case.clmsum** and **case.scf**. | | | | |

### II.6.3 Calculating properties

The following equilibrium properties can be calculated when the SCF cycle has converged:Energy band structure

- Density of states (DOS)
- Electron density
- X-ray spectra
- Optics

## II.7 References of the chapter II

[1] Kaltsoyannis N, McGrady JE. Principles and applications of density functional theory in inorganic chemistry. Springer; 2004.

[2] Iqbal MA, Ashraf N, Shahid W, Afzal D, Idrees F, Ahmad R. Fundamental of density functional theory: recent developments, challenges and future horizons. Academic editor, IntechOpen; 2022.

[3] Born M; J. R. Oppenheimer JR. "Zur Quantentheorie der Molekeln" (On the Quantum Theory of Molecules). Annalen der Physik (in German) 1927;389(20): 457–484.

[4] P. Hohenberg P, Kohn W. Inhomogenous electron gas. Physical Review 1964;136(3B):864

[5] Kohn W, Sham LJ. Self-consistent equations including exchange and correlation effects. Physical Review A 1965;140:1133.

[6] Cottenier S. Density Functional Theory and the Family of (L)APW-methods: a step-by-step introduction; Institut for nuclear and radiation physcis, Ku Leuven, Belgium; 2013.

[7] Slater JC. Wave functions in a periodic potential. Phys Review 1937;51:846.

[8] Singh DJ, Ground-state properties of lanthanum: treatment of extended-core states. Physical Review B 1991;43, 6388.

[9] Madsen GKH, Blaha P, Schwarz K, Sjöstedt E, Nordström L. Efficient linearization of the augmented plane-wave method. Phys Review B 2001:64:195134.

[10] Sjöstedt E, Nordström L, Singh DJ. An alternative way of linearizing the augmented plane-wave method. Solid state communications 2000;114:15-20.

[11] Andersen OK. Linear methods in band theory. Phys Review B 1975;12:3060-3068.

[12] Mattheis LF, Hamaan DR. Linear augmented-plane-wave calculation of the structural properties of bulk Cr, Mo, a,d W. (1986). Phys Review B 1986;33:823-828.

[13] Schwarz K, Blaha P. Description of an LAPW DF program (WIEN95).Lecture Notes in Chemistry book series Springer Link 1996;67:139-153.

[14] Singh DJ, Nordström L. Plane waves, Pseudopotentials and LAPW method. Second edition Springer, Berlin; 2006.

# Chapter III: Results and discussions

## III.1 Introduction

Conventional energy sources, such as nuclear power and fossil fuels, are bad for the environment because they cause permanent harm [1]. Fossil fuel burning is the primary source of atmospheric pollution. The release of greenhouse gases like nitrous oxide and carbon dioxide into the atmosphere is attributed to the combustion of coal and petroleum [2]. In the near future, hydrogen will gradually replace petroleum products as a source of alternative energy since it can store and deliver energy in forms that can be used. The energy density of hydrogen ranges from 120 MJ/kg (lower heating value, LHV) to 142 MJ/kg (higher heating value, HHV), which are values that are around three times higher than the energy density of petroleum [3-5].

However, the development of hydrogen-based systems, particularly for transportation applications, holds the greatest promise for employing hydrogen as an energy vector [3]. Furthermore, this green energy source still needs very sophisticated technology for producing hydrogen in a way that is safe, affordable and renewable, for lowering the cost of fuel cells, and most importantly, for storing hydrogen in a way that is safe, lightweight and compact. Using materials where hydrogen forms chemical bonds or adsorbing hydrogen onto them are two methods for doing this [6].

As a result, in recent years there has been a growing interest in technology that use hydrogen as a fuel. The hydrogen element bond in the periodic table can transition from an ionic to a covalent and back to an ionic state by travelling across a row from left to right [7].

Fuel cell technologies are employed in a variety of fixed, portable and mobile applications. The hydrides, whether alloy or intermetallic compounds, are generated by interaction between hydrogen and a metal [8]. The development of materials-based hydrogen storage is still being hampered by a number of problems, necessitating additional study before widespread commercialization can be anticipated [9]. The key characteristics of solid-state hydrogen storage materials include their cost, reversibility, heat of adsorption/desorption, operational temperature range, volumetric and gravimetric capabilities and operating conditions [6].

The hydrides surpass 100 gH/l in a unit volume of solid state hydrogen storage, achieving a very high volumetric hydrogen storage density [10-12]. However, as these systems are often intended to store significant amounts of energy, strong reversibility in these hydrides is essential to ensure a lengthy system life cycle, and the cost per kWh of storage capacity should be as low as possible [6].

One of the most promising anode materials for next-generation energy storage devices is lithium, which has a modest mass [13]. LiH retains 12.7 wt% H2 (or 0.1 kg $H_2$/l) due to its density of

0.82 g/cm$^3$ and molecular weight of 7.95 g/mol [14–15]. Lithium hydride may be stored for a very long time without decomposing because of its excellent stability.

This surprising fact shows that lithium and hydrogen atoms interact quite strongly. At a temperature of roughly 850 °C, the lithium hydride partitions into its constituent parts [16].

The current work is mainly divided into many sections which are:

- Structural, electronic and stability properties of saline hydrides $LiH_n$ (n=1, 2, 4) were calculated in the hope of determining which one was more hydrogen reversible.
- The effect of the hydrostatic pressure on the LiH hydride (crystallized in 225 space group) was studied to determine the convenient pressure that could be utilized in hydrogen storage systems.
- The stability of the Li-based hydride is decreased and the hydrogen kinetics are improved by substituting a few lithium atoms with metal atoms. In order to select the most suitable atomic substitutions in Li7XH8 (X (AM) = Na, K, Rb and X (TM) = Ti, V, Cr), which stores and releases hydrogen comfortably and abundantly, the influence of alkali (AM) and transition metal (TM) atom substitutions is qualitatively examined. The hydrides LiH and $Li_7XH_8$'s structural and electronic properties are established. The calculated formation energy values and electron properties allow for the determination of the impact of alkali and transition metal atom replacements on the stability of the hydrides $Li_7XH_8$. In order to find the appropriate and acceptable atomic replacement and achieve both a high storage capacity and a good reversibility for the hydrogen, the gravimetric hydrogen storage parameter is compared with the stability of the hydrides $Li_7XH_8$.
- The same method, as in $Li_7XH_8$ hydrides, was applied on $Li_3XH_4$ (X (AM) = Na, K, Rb and X (TM) = Ti, V, Cr) to compare, qualitatively and quantitatively, between the two hydride systems.

The FP-LAPW method [17–19] is used for all DFT computations in this work, and the generalized gradient approximation (GGA 96) [20] as implemented in the WIEN2k [21] tool is used to approximate the exchange-correlation potential. The valence electron orbits of the basic elements Li, H, Na, K, Rb, Ti, V and Cr are as follows: Li ($1s^2\ 2s^1$), H ($1s^1$), Na ($2s^2\ 2p^6 3s^1$), K ($3s^2 3p^6 4s^1$), Rb ($4s^2 3d^{10} 4p^6 5s^1$), Ti ($3s^2 3p^6 4s^2 3d^2$), V ($3s^2 3p^6 4s^2 3d^3$) and Cr ($3s^2 3p^6 4s^2 3d^4$). The muffin-tin radii (RMT) are 1.8 Bohr for a metal and 1.2 Bohr for hydrogen. For all Li based

hydrides, we took an energy convergence criterion of $10^{-4}$ Ry and optimized RmtKmax and the k-points number parameters to be 7 and 1000, respectively (see convergence tests in Appendix A). The nonspin polarized approximation was used for all calculations. The non-linear Murnaghan equation of state is fitted to the total energy vs volume data to determine the volume optimization. [22, 23]. The formula of Murnaghan's equation of state is given by:

$$E(V) = E_0 + \frac{B}{B'(B'-1)}\left[V\left(\frac{V_0}{V}\right)^{B'} - V_0\right] + \frac{B}{B'}(V - V_0), \qquad \text{(III.1)}$$

where $E_0$ and $V_0$ are the energy and the volume at a ground state, $B$ and $B'$ are the bulk modulus and its first derivative with respect to the pressure. The volume optimizations for all hydrides were shown in Appendix B.

## III.2 Li metal and $LiH_n$ (n=1, 2, 4) hydrides

Li_229 metal, as a host metal, crystallizes in a bcc structure and a space group N° 229 (Fig. III.1). $LiH_n$ (n=1, 2, 4) hydrides crystallize in six crystal structures (Fig. III.2), one of them is LiH_225 which has a NaCl-like structure and a space group N° 225 (Fig. III.2.a). The LiH_225 hydride is well known by experimentalists and its crystal parameters are available in the literature. The other hydrides LiH_221, $LiH_2$_191, $LiH_2$_194, $LiH_4$_215 and $LiH_4$_221 have been developed theoretically as a function of hydrogen storage, even though they have not been synthesized experimentally.

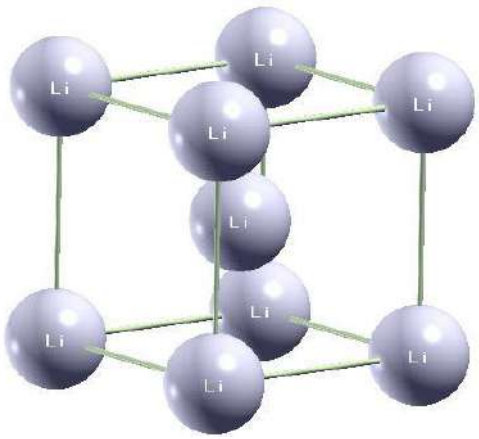


**Figure III.1:** Structure of the Li_229 metal.

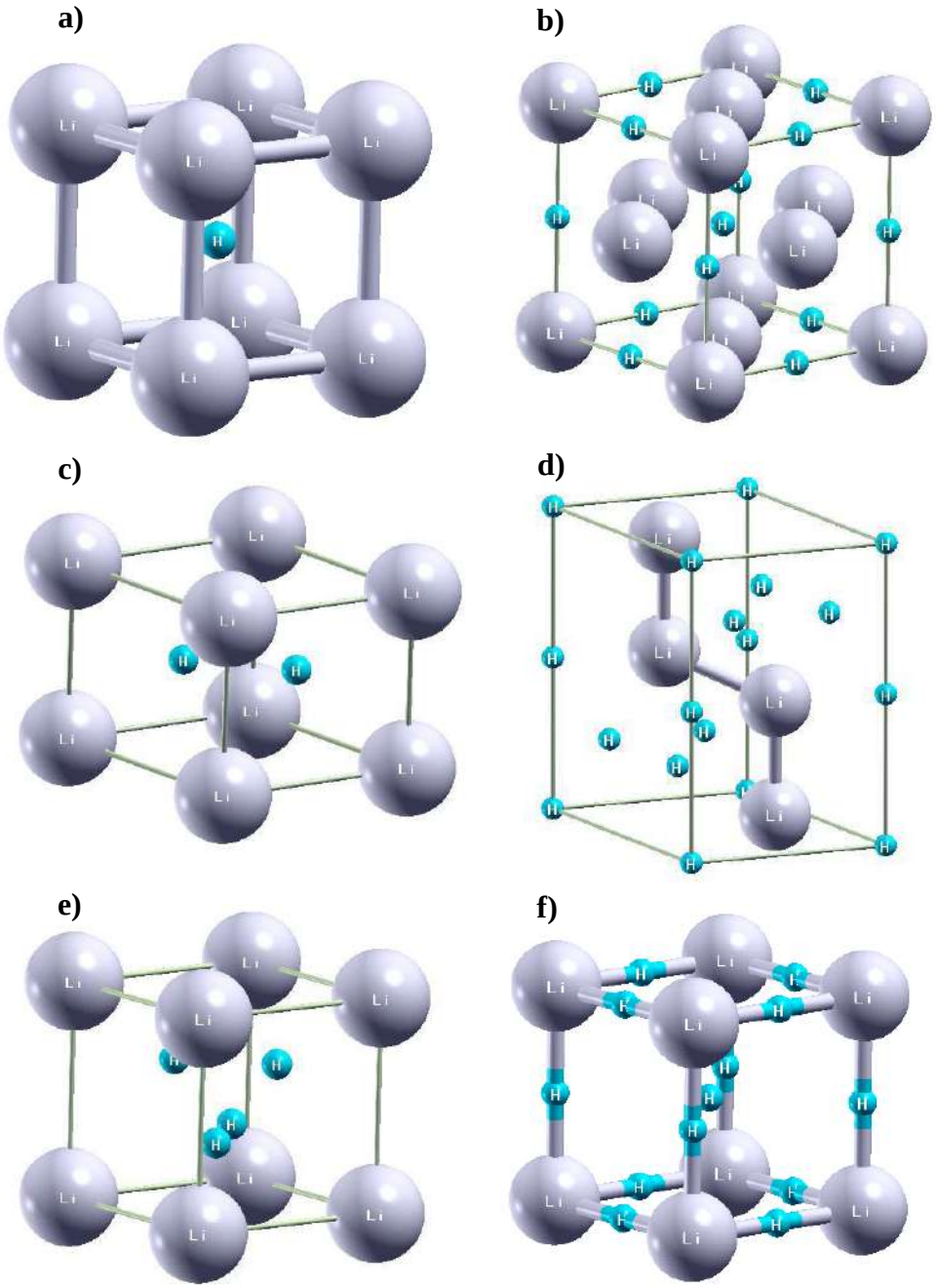


**Figure III.2:** Structures of a) LiH_221 and b) LiH_225 in cubic lattice, c) $LiH_2$_191 and d) $LiH_2$_194 in hexagonal lattice, e) $LiH_4$_215 and $LiH_4$_221 in cubic lattice.

## III.2.1 Structural properties of the Li metal and $LiH_n$ (n=1, 2, 4) hydrides

Table III.1 shows the input structural parameters of calculations for Li_229, LiH_225, LiH_221, $LiH_2$_191, $LiH_2$_194, $LiH_4$_215 and $LiH_4$_221. These parameters are the compounds, the lattice, the spatial group, the Wyckoff positions and the Li and H coordinates.

In order to determine structure properties of the Li metal and saline $LiH_n$ hydrides at a ground state, a volume optimization has been done where the volume has been changed towards by compression and expansion to find the equilibrium volume.

Calculated lattice parameters, bulk modulus, pressure derivative B' and total energy of Li_229, LiH_225, LiH_221, $LiH_2$_191, $LiH_2$_194, $LiH_4$_215 and $LiH_4$_221 are shown in table III.2 (for the related figures, see Appendix B). The lattice parameters of LiH_225 are close to the theoretical and experimental ones [24, 25]. In cubic lattice hydrides, the LiH_221 hydride has smaller lattice parameters than the LiH_225, the $LiH_4$_215 and the $LiH_4$_221 hydride. In hexagonal lattice hydrides, lattice parameters in the $LiH_2$_191 hydride are smaller than in the $LiH_2$_194 hydride. The relative volumetric variation (volumetric density) of saline hydrides referred to Li_229 metal is calculated by this equation:

$$D_V = \frac{V_{hydride} - V_{Li\,metal}}{V_{Li\,metal}} \qquad \text{(III.2)}$$

**Table III.1:** Input structural parameters of calculations for Li_229, LiH_225, LiH_221, $LiH_2$_191, $LiH_2$_194, $LiH_4$_215 and $LiH_4$_221.

| Compounds | Lattice | Spatial group | Wyckoff positions | | Li coordinates | H coordinates |
|---|---|---|---|---|---|---|
| | | | Li | H | | |
| Li_229 | Cubic | 229, Im-3m | 2a | / | (0, 0, 0) | / |
| LiH_225 | Cubic | 225, Fm-3m | 4a | 4b | (0, 0, 0) | (1/2, 1/2, 1/2) |
| LiH_221 | Cubic | 221, Pm-3m | 1a | 1b | (0, 0, 0) | (1/2, 1/2, 1/2) |
| $LiH_2$_191 | hexagonal | 191, P6/mmm | 1a | 2d | (0, 0, 0) | (1/3, 2/3, 1/2)<br>(2/3, 1/3, 1/2) |
| $LiH_2$_194 | hexagonal | 194, $P6_3/mmc$ | 4f | 2a | (1/3, 2/3, 0.062)<br>(2/3, 1/3, 0.562)<br>(2/3, 1/3, 0.938)<br>(1/3, 2/3, 0.438) | (0, 0, 0), (0, 0, 1/2) |
| | | | | 6h | | (0.833, 0.666, 1/4)<br>(0.334, 0.167, 1/4)<br>(0.833, 0.167, 1/4)<br>(0.167, 0.334, 3/4)<br>(0.666, 0.833, 3/4)<br>(0.167, 0.833, 3/4) |
| $LiH_4$_215 | Cubic | 215, P-43m | 1a | 4e | (0, 0, 0) | (0.333, 0.333, 0.333)<br>(0.667, 0.667, 0.333)<br>(0.667, 0.333, 0.667)<br>(0.333, 0.667, 0.667) |
| $LiH_4$_221 | Cubic | 221, Pm-3m | 1a | 3d | (0, 0, 0) | (1/2, 0, 0), (0, 1/2, 0), (0, 0, 1/2) |
| | | | | 1b | | (1/2, 1/2, 1/2) |

**Table III.2:** Calculated lattice parameters, bulk modulus, pressure derivative B' and total energy of Li_229, LiH_225, LiH_221, $LiH_2$_191, $LiH_2$_194, $LiH_4$_215 and $LiH_4$_221.

| Compounds | Lattice | B (GPa) | B' | $E_0$ (Ry) | Lattice parameters (Å) | | |
|---|---|---|---|---|---|---|---|
| | | | | | a | b | c |
| Li_229 | Cubic | / | / | -15.0442 | 3.491 | 3.491 | 3.491 |
| LiH_225 | Cubic | 40.6832 | 3.0216 | -16.2716 | 4.004 | 4.004 | 4.004 |
| LiH_225 [24][a] | Cubic | / | / | -16.2300 | 4.069 | 4.069 | 4.069 |
| LiH_225 [25][b] | Cubic | / | / | / | 4.083 | 4.083 | 4.083 |
| LiH_221 | Cubic | 33.4331 | 5.5495 | -16.2376 | 2.507 | 2.507 | 2.507 |
| $LiH_2$_191 | hexagonal | 43.2657 | 6.9275 | -17.3191 | 2.949 | 2.949 | 2.514 |
| $LiH_2$_194 | hexagonal | 45.7687 | 5.2253 | -17.2693 | 3.968 | 3.968 | 5.446 |
| $LiH_4$_215 | Cubic | 32.5880 | 8.5858 | -19.2729 | 3.023 | 3.023 | 3.023 |
| $LiH_4$_221 | Cubic | 47.1320 | 5.0112 | -19.3733 | 3.252 | 3.252 | 3.252 |
| a: VASB Calculations<br>b: Experimental | | | | | | | |

The gravimetric hydrogen storage density of saline hydrides is determined as following:

$$G\ (wt.\%) = \frac{\text{H atoms number} * M_H}{\text{H atoms number} * M_H + \text{Li atoms number} * M_{Li}} \quad \text{(III.3)}$$

$M_H$ (1.0079 g/mol) and $M_{Li}$ (6.941 g/mol) represent molar masses of hydrogen and lithium, respectively. Table III.3 show both volumetric density and gravimetric hydrogen density of saline hydrides. For hydrogen storage materials, we need to have materials with less volumetric variation and high gravimetric hydrogen storage density. Results in table III.3 display a higher relative volumetric reduction from Li_229 metal to LiH_221 hydride of -62.96% compared to others. $LiH_2$_191, $LiH_4$_215 and $LiH_4$_221 hydrides exhibit a similar volumetric reduction of -55.49, -35.06 and -19.16 %, respectively. A volumetric augmentation of 50.88 % has been observed from Li_229 metal to LiH_225 hydride, and of 74.54% from Li_229 metal to $LiH_2$_194 hydride.

**Table III.3:** Volumetric variation and gravimetric hydrogen density of saline hydrides LiH_225, LiH_221, $LiH_2$_191, $LiH_2$_194, $LiH_4$_215 and $LiH_4$_221.

| Hydrides | Lattice | Volumetric variation (%) | Gravimetric storage density of H (wt. %) |
|---|---|---|---|
| LiH_225 | Cubic | 50.88 | 12.67 |
| LiH_221 | Cubic | - 62.96 | 12.67 |
| $LiH_2$_191 | hexagonal | - 55.49 | 22.50 |
| $LiH_2$_194 | hexagonal | 74.54 | 22.50 |
| $LiH_4$_215 | Cubic | - 35.06 | 36.74 |
| $LiH_4$_221 | Cubic | - 19.16 | 36.74 |

Generally, all of these saline hydrides have very good gravimetric storage densities of hydrogen compared to Mg based hydrides which are considered as acceptable hydrogen storage materials with a hydrogen gravimetry equal to ~7% (wt.) [26].

There is another important parameter to understand the behavior of hydrides and the reversibility of the hydriding/dehydriding reactions. This parameter is the hydride stability which is the key to rationally investigate and design potential hydrogen-storage materials [1].

## III.2.2 Electronic properties of the Li metal and $LiH_n$ (n=1, 2, 4) hydrides

Fig. III.3 displays the total densities of states of Li metal and saline hydrides $LiH_n$ (n=1, 2 and 4). It shows a semi-conductor character for LiH_221 ($E_g$=0.74eV), an insulator character for LiH_225 and a metallic character for Li, $LiH_2$_191, $LiH_2$_194, $LiH_4$_221 and $LiH_4$_215.

Partial densities of states are displayed in Fig. III.4. In the valence band, both 2p Li and 2s H orbitals present the same behavior in energy and geometry, indicating a high hybridization between them for saline hydrides $LiH_n$ (n=1, 2, 4).

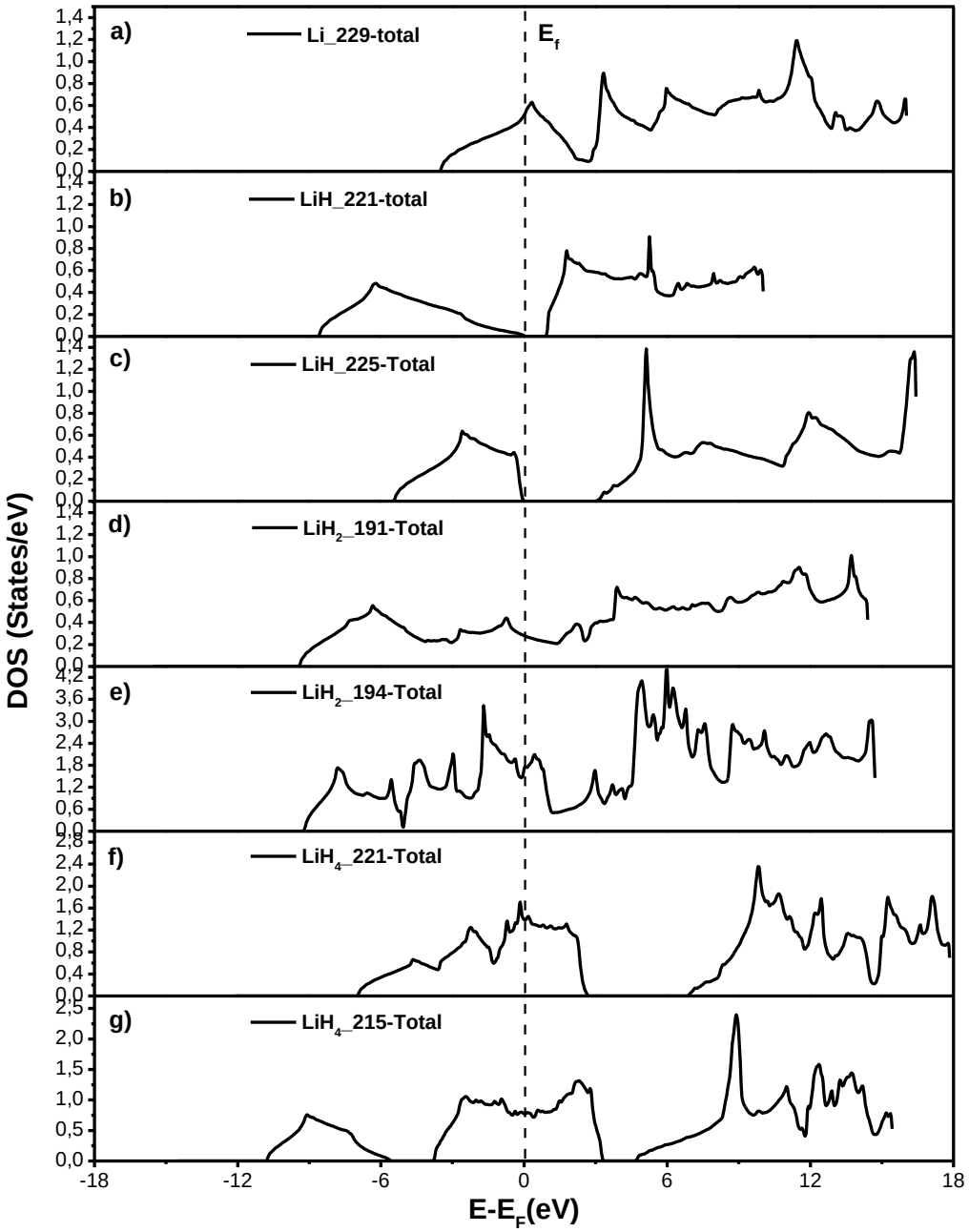


**Figure III.3:** Total densities of states of a) Li_229, b) LiH_221, c) LiH_225, d) $LiH_2$_191, e) $LiH_2$_194, f) $LiH_4$_221 and g) $LiH_4$_215.

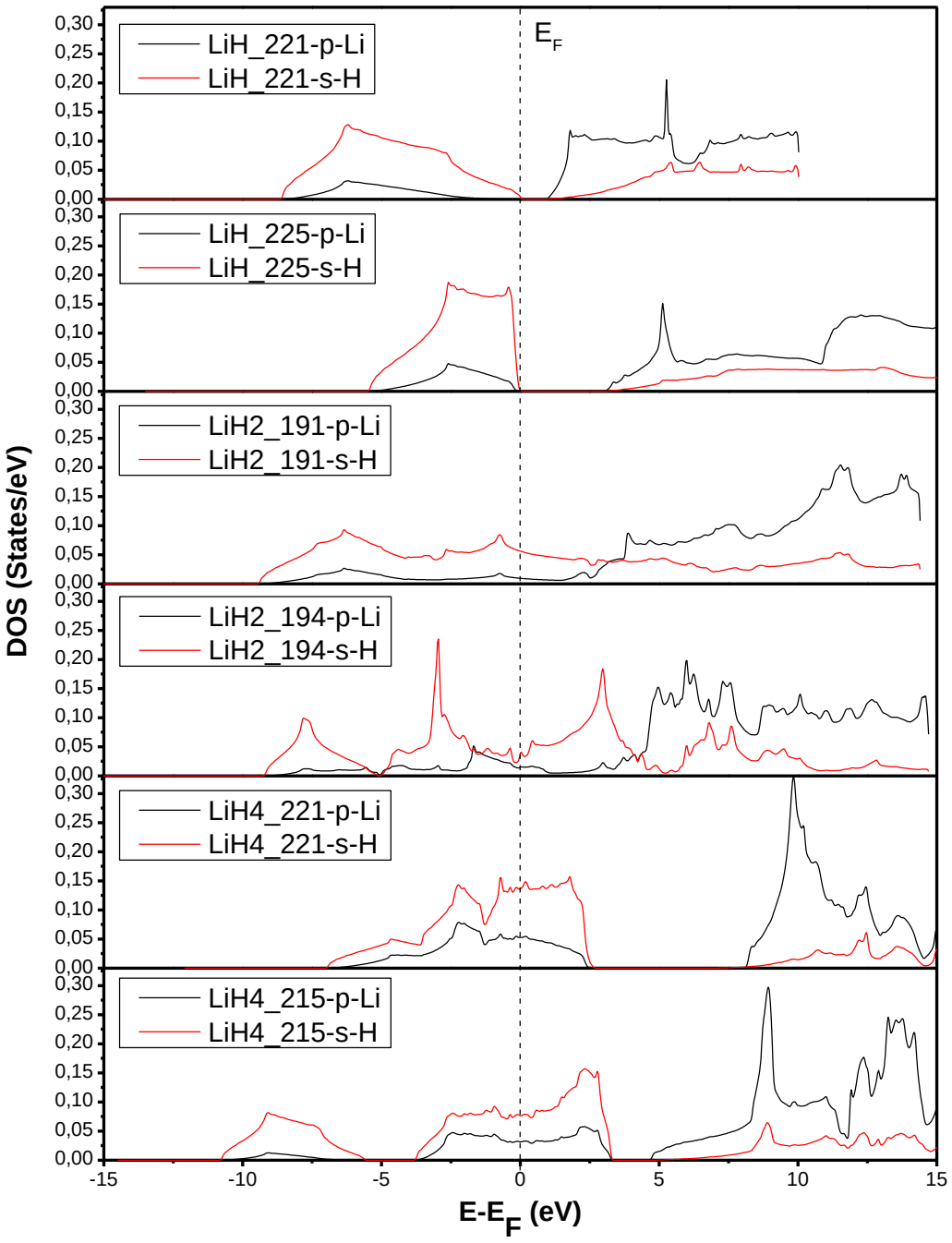


**Figure III.4:** Partial densities of states of $LiH_n$ (n=1, 2 and 4).

## III.2.3 Cohesive energy of saline hydrides $LiH_n$ (n=1, 2, 4)

The cohesive energy or the bonding energy is considered as an important parameter for stability investigations. In order to calculate the cohesive energy of saline hydrides $LiH_n$ (n=1, 2, 4), we can use the following formula:

$$E_{coh}\ (LiH_n) = E_{crystal}(LiH_n) - E_{atom}(Li) - n \times E_{atom}(H). \qquad \text{(III.4)}$$

Calculated cohesive energy values of saline hydrides $LiH_n$ (n=1, 2, 4) are revealed in Table III.4 and Fig III.5. From these results of the cohesive energy, we can find a different stability of these saline hydrides. The most stable hydride which has the strongest bonding energy is the $LiH_4$_221. The less stable hydride is LiH_221 which has the lowest cohesive energy. The latter hydride could probably be used for hydrogen storage.

**Table III.4:** Cohesive energy values of saline hydrides $LiH_n$ (n=1, 2, 4).

| **Hydrides** | **$E_{Coh}$ (Ry)** |
|---|---|
| LiH_225 | -0.37 |
| LiH_221 | -0.34 |
| $LiH_2$_191 | -0.46 |
| $LiH_2$_194 | -0.41 |
| $LiH_4$_215 | -0.48 |
| $LiH_4$_221 | -0.58 |

## III.2.4 Conclusion

Structural, electronic and stability properties of saline hydrides $LiH_n$ (n=1, 2, 4) have been studied using DFT and FP-LAPW approximations. The lattice parameters of LiH_225 are close to the theoretical and experimental ones. In cubic lattice hydrides, the LiH_221 hydride has smaller lattice parameters than LiH_225, $LiH_4$_215 and $LiH_4$_221 hydrides. In hexagonal lattice hydrides, lattice parameters are smaller in the $LiH_2$_191 hydride than in the $LiH_2$_194 hydride. Results display a higher relative volumetric reduction of -62.96% in going from Li_229 metal to LiH_221 hydride. $LiH_2$_191, $LiH_4$_215 and $LiH_4$_221 hydrides exhibit a similar volumetric reduction of -55.49, -35.06 and -19.16 %, respectively. A volumetric augmentation of 50.88 %

has been observed in going from Li_229 metal to LiH_225 hydride, and of 74.54% in going from Li_229 metal to $LiH_2$_194 hydride. Generally, all of these saline hydrides have very good gravimetric storage densities of hydrogen compared to Mg based hydrides which are considered as acceptable hydrogen storage materials with a hydrogen gravimetry equal to ~7% (wt.). We find a semi-conductor character for LiH_221, an insulator character for LiH_225 and a metallic character for Li, $LiH_2$_191, $LiH_2$_194, $LiH_4$_221 and $LiH_4$_215. In the valence band, both 2p Li and 2s H orbitals present the same behavior in energy and geometry, indicating a high hybridization for saline hydrides $LiH_n$ (n=1, 2, 4). The most stable hydride which has the strongest bonding energy is the $LiH_4$_221. The less stable hydride is LiH_221 which has the lowest cohesive energy. The latter hydride could probably be used for hydrogen storage.

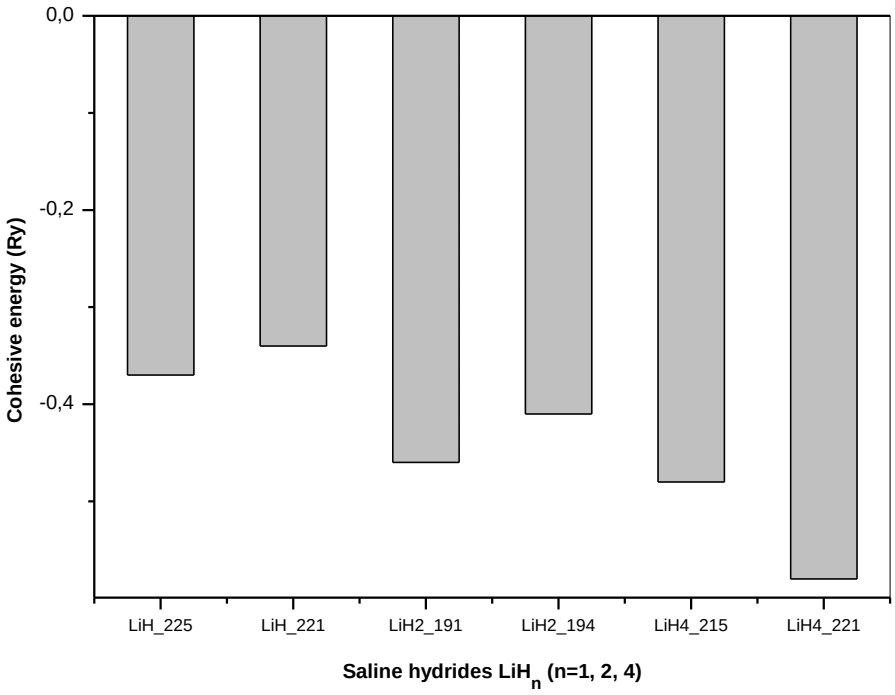


**Figure III.5:** Cohesive energy values of saline hydrides $LiH_n$ (n=1, 2, 4).

## III.3 Effect of the hydrostatic pressure on the LiH_225 hydride

The hydrostatic pressure as a function of hydride stability is one of the important parameters. In order to determine the convenient pressure that could be utilized in hydrogen storage systems, it is crucial to study structural parameters and densities of states as a function of hydrostatic pressure.

### III.3.1 Structural parameters

Eleven different volumes points of LiH_225 are chosen from a volume optimization at ground state (0K). Table III.5 shows total energy, hydrostatic pressure, volume and lattice parameters values of LiH_225.

**Table III.5:** Total energy, hydrostatic pressure, volume and lattice parameters values of LiH_225.

| Point | Hydrostatic pressure (GPa) | Total energy (Ry) | Volume $(Bohr)^3$ | Lattice parameter a (Å) |
|---|---|---|---|---|
| 1 | 3.464 | -16.270810 | 100.3056 | 3.902 |
| 2 | 4.661 | -16.270209 | 98.0641 | 3.873 |
| 3 | 5.972 | -16.269329 | 95.8227 | 3.843 |
| 4 | -0.394 | -16.271584 | 109.2715 | 4.015 |
| 5 | 0.450 | -16.271600 | 107.0300 | 3.988 |
| 6 | 1.369 | -16.271486 | 104.7886 | 3.960 |
| 7. (Equilibrium state) | -1.356 | -16.271670 | 108.2975 | 4.004 |
| 8 | 2.371 | -16.271242 | 102.5471 | 3.931 |
| 9 | -1.371 | -16.271381 | 112.0733 | 4.050 |
| 10 | -2.227 | -16.271108 | 114.8752 | 4.083 |
| 11 | -2.865 | -16.270747 | 117.1166 | 4.109 |

Fig. III.6 shows a curve of total energy versus volume of LiH_225 according to a Murnaghan equation fitting. The total energy of LiH_225 as a function of the hydrostatic pressure is displayed in Fig. III.7. A variation of the unit cell volume of LiH_225 with the hydrostatic pressure is exhibited in Fig. III.8.

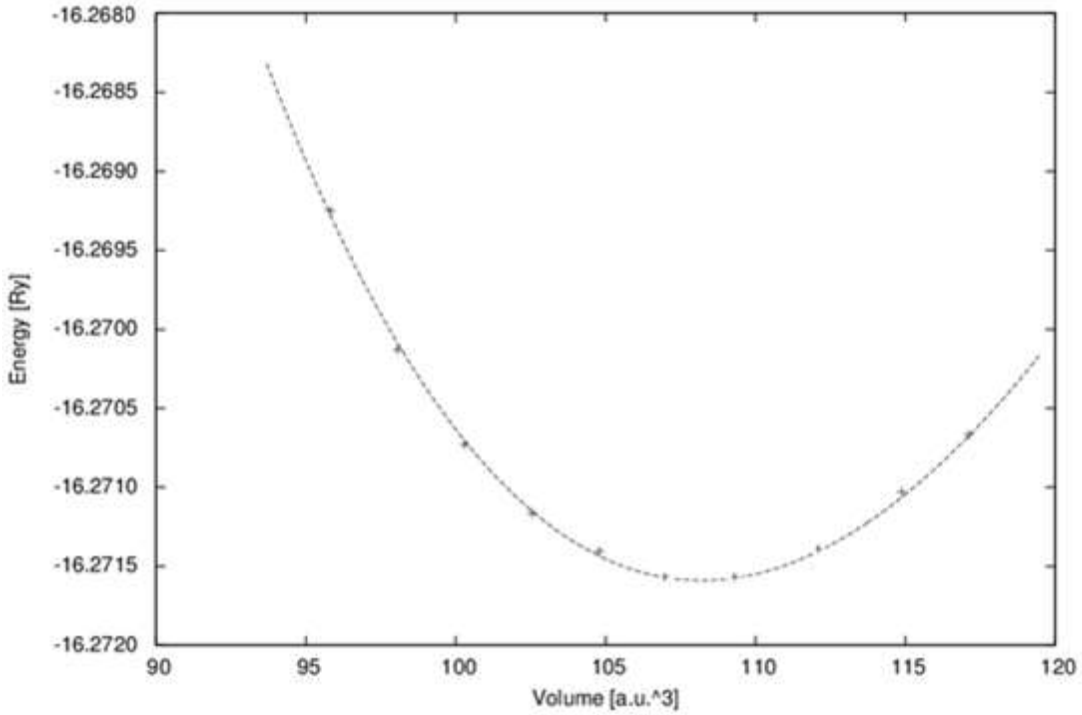


**Figure III.6:** Total energy of LiH_225 versus volume.

These results show:

- Equilibrium point corresponds to a hydrostatic pressure of $P_{eq} = -1.356$ GPa, a unit cell volume of $V_{eq} = 108.2975\ (Bohr)^3$ **,** a total energy of $E_{eq} = -16.271670$ Ry and a lattice parameter of $a = 4.004$ Å
- The curve in Fig.III.6 is divided into two parts: first one [95.822-107.030 $(Bohr)^3$] where volumes are lower than equilibrium volume and the second [109.271-117.117 $(Bohr)^3$] where volumes are bigger than equilibrium volume, which are describing the compression and the expansion state, respectively.
- In expansion states (points: 4, 9, 10 and 11) relatively to the equilibrium point (point 7), the pressure takes negative values whose directions are towards the inside of the cell. In this case, the unit cell volume increases with increasing pressure (Fig.III.7). Other points indicating compression states have positive pressure values whose directions are towards the outside of the cell. In this case, the unit cell volume decreases with increasing pressure

(Fig.III.7). The value and direction of a hydrostatic pressure is directly associated with its distance from the equilibrium point.

- The equilibrium point has the highest total energy. With the exception of the equilibrium point, the total energy decreases gradually with increasing hydrostatic pressure (Fig.III.8).

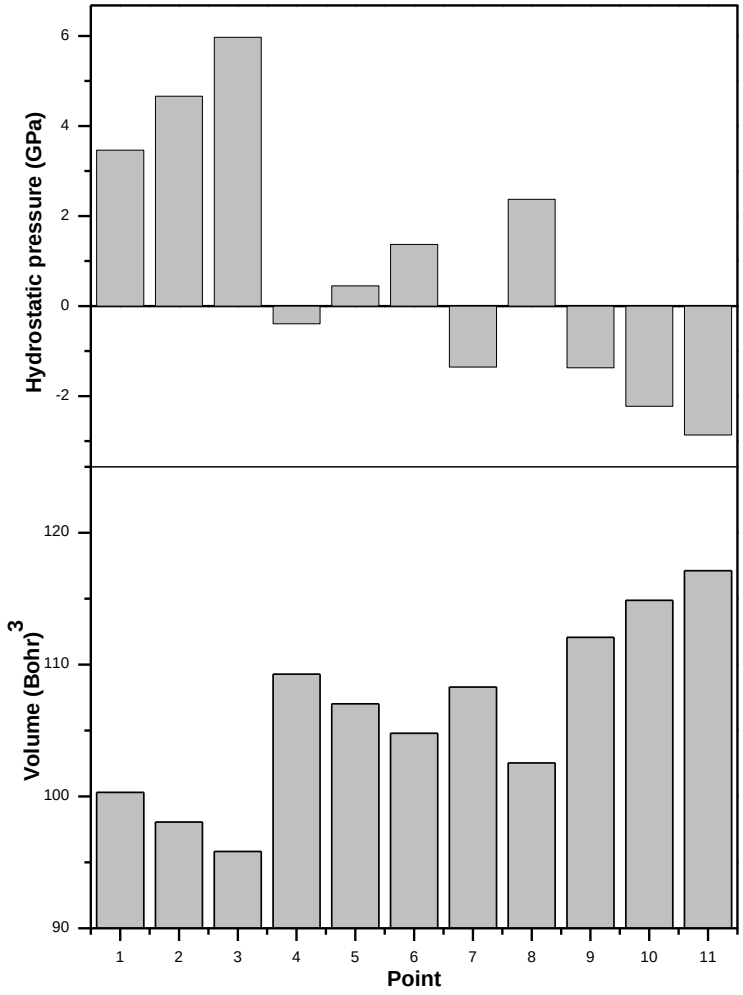


**Figure III.7:** Unit cell volume of LiH_225 versus hydrostatic pressure.

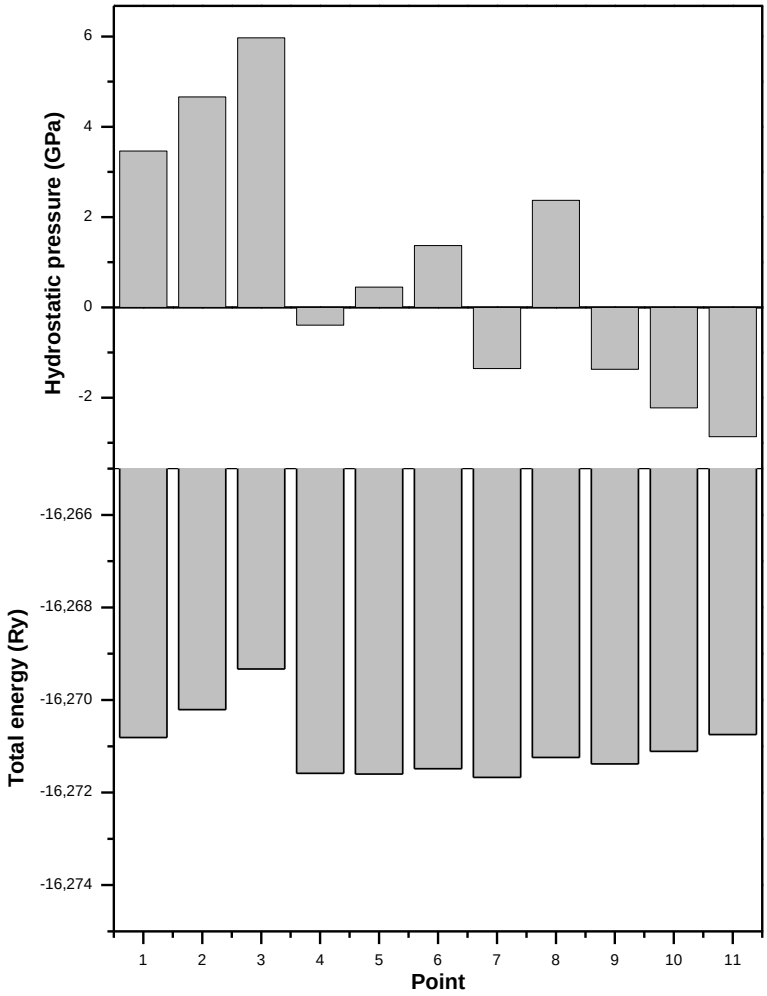


**Figure III.8:** Total energy of LiH_225 versus hydrostatic pressure.

The formation energy for all hydrostatic pressure points is calculated by this formula:

$$E_f = 2E_{LiH\_225} - 2E_{Li} - E_{H_2} \quad \text{(III.5)}$$

$E_{LiH\_225}$, $E_{Li}$ and $E_{H_2}$ are total energies of LiH_225, Li and $H_2$, respectively. Fig. III.9 shows the variation of formation energy of LiH_225 as a function of hydrostatic pressure. As the formation energy (in absolute value) increases, the stability of the hydride increases and vice versa.

The equilibrium point (N° 7), corresponding to $P_{eq} = -1.356$ GPa, shows the highest stability compared to others pressure values. The point N° 3, corresponding to P=5.972 GPa, exhibit the lowest stability compared to others pressure values. Therefore, at the equilibrium state, hydrogen

reversibility and hydrogen storage are more difficult. The best point for hydrogen storage applications among these points is the point N° 3. In addition, the latter has the smallest lattice parameters, which is satisfactory for hydrogen storage systems.

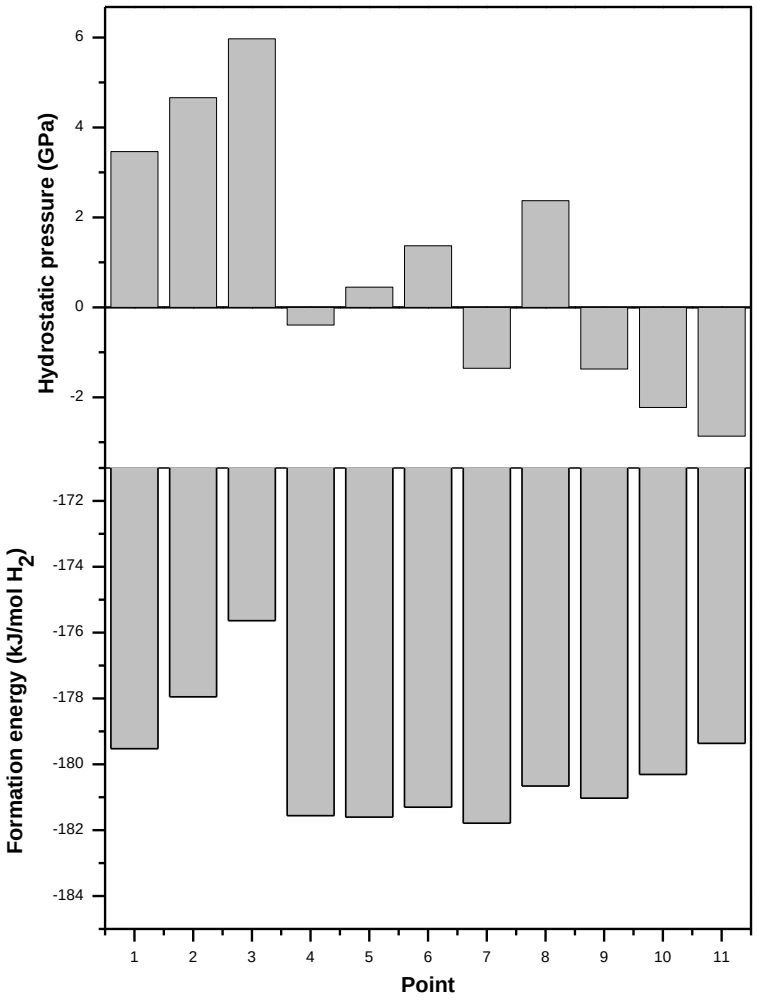


**Figure III.9:** Formation energy of LiH_225 versus hydrostatic pressure.

## III.3.2 Density of states

Total and partial densities of states for LiH_225 with respect to hydrostatic pressures are given in Fig. III.10 and Fig. III.11, respectively. Fig.III.10 shows that different hydrostatic pressures do not have an influence on the insulating character of LiH_225 hydride. For better understanding of the tendency of reaction between orbitals (states), it is needed to further study the partial density of states. Fig. III.11 shows the reaction between 2p Li orbital and 1s H orbital in the valence band as a function of different hydrostatic pressures. In the valence band, various

pressures influence the shape of 1s H orbitals more than that of 2p Li orbitals. Densities of states at two peaks of 1s H orbitals corresponding to point N° 3 are lower than the others. Therefore, in this point, there is a weak hybridization between 2p Li and 1s H orbitals, indicating lower stability and higher hydrogen kinetic reversibility.

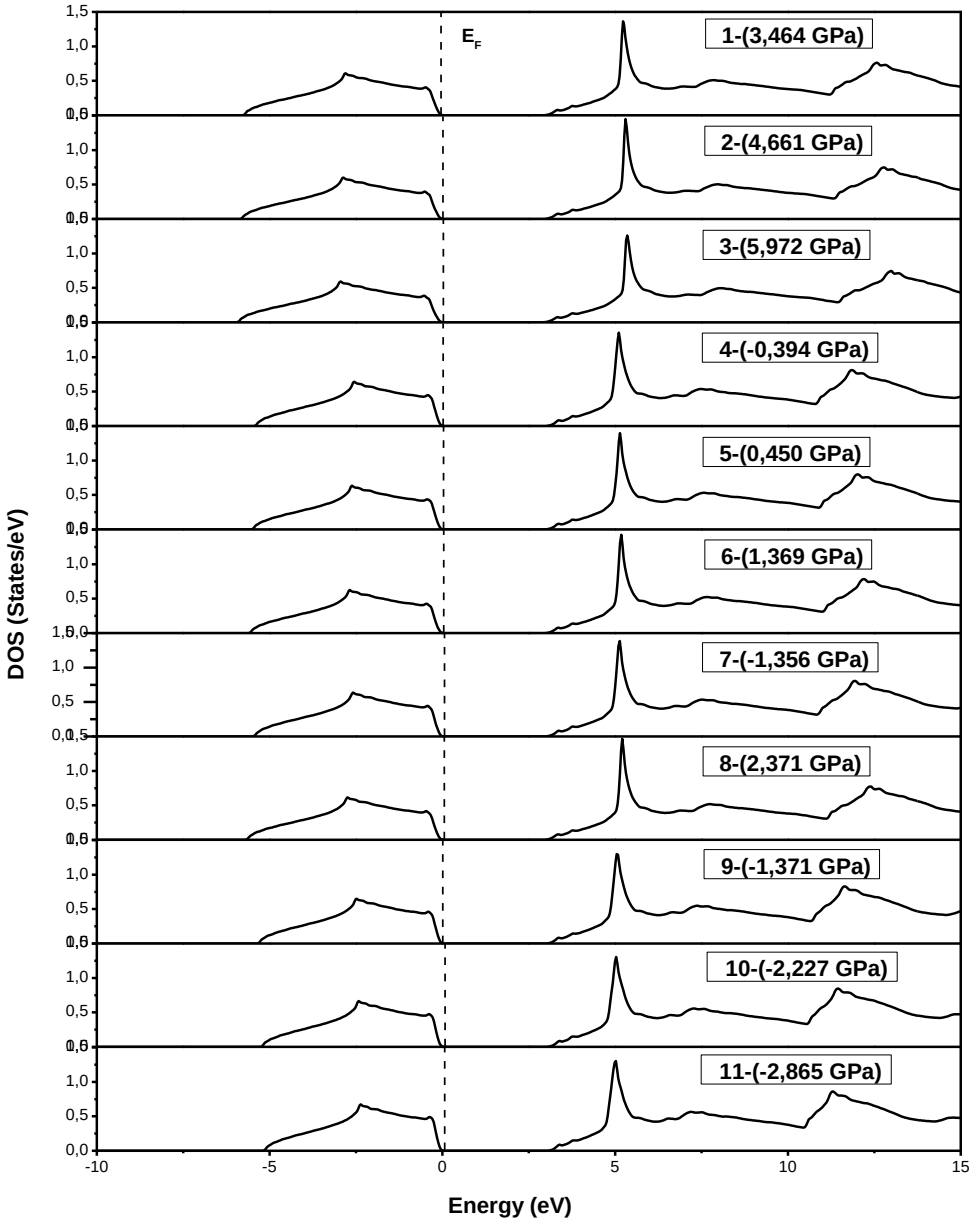


**Figure III.10:** Total density of states of LiH_225 versus hydrostatic pressure.

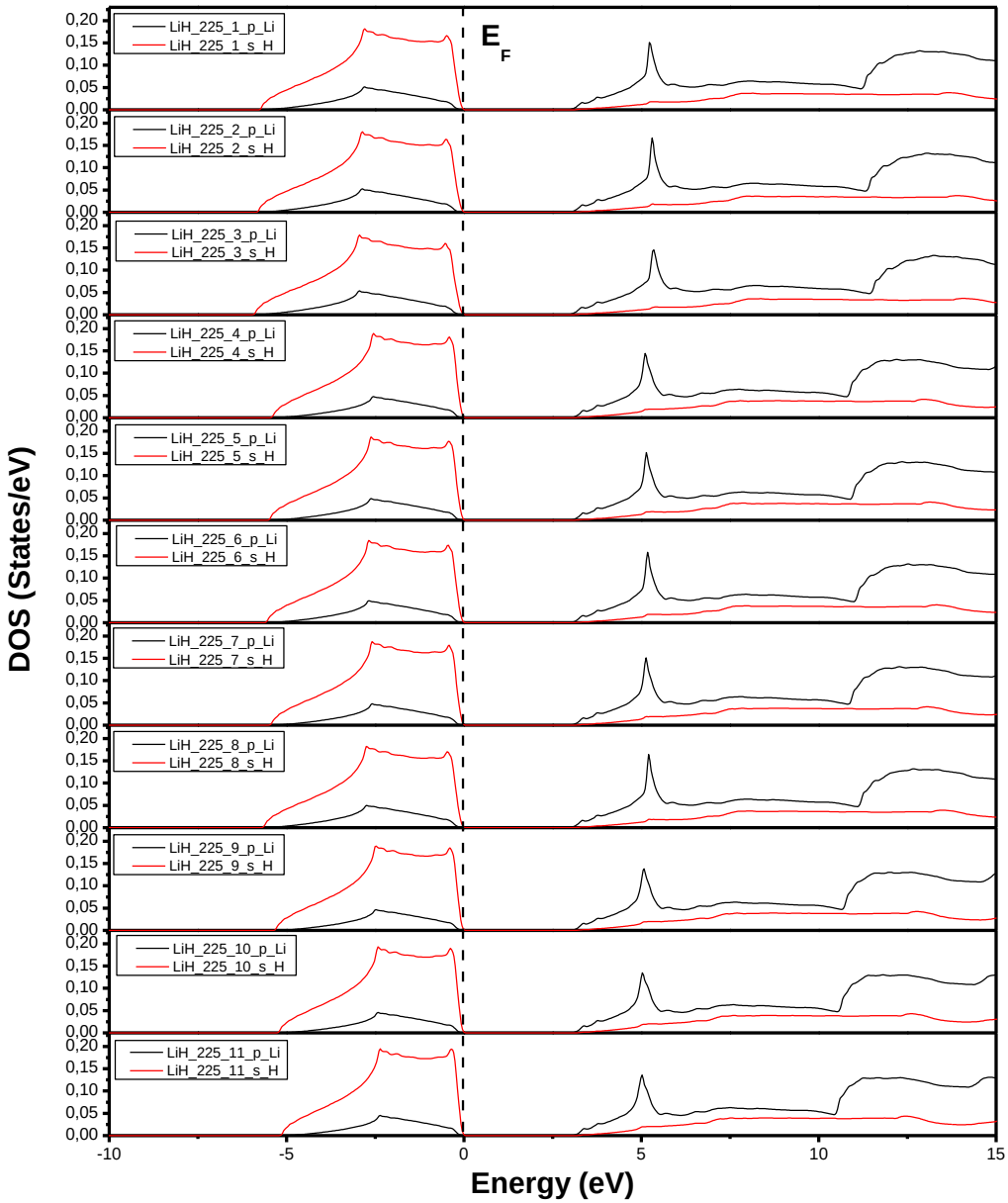


**Figure III.11:** Partial density of states of LiH_225 versus hydrostatic pressure.

## III.3.3 Conclusion

Based on DFT and FP-LAPW approximations, the effect of the hydrostatic pressure on the LiH hydride (crystallized in 225 space group) was studied to determine the convenient pressure that could be utilized in hydrogen storage systems. The equilibrium point corresponds to a hydrostatic pressure of $P_{eq} = -1.356$ GPa, a unit cell volume of $V_{eq} = 108.2975\ (Bohr)^3$, a total energy of $E_{eq} = -16.271670$ Ry and a lattice parameter of $a = 4.004$ Å. Compression and expansion states are relatively dependent on the equilibrium point. The value and direction of a hydrostatic pressure is directly associated with its distance from the equilibrium point.

With the exception of the equilibrium point, which has the highest total energy value, the total energy decreases gradually with increasing hydrostatic pressure.

The equilibrium point (N° 7), corresponding to $P_{eq} = -1.356$ GPa, shows the highest stability compared to other pressure values. The point N° 3, corresponding to P=5.972 GPa, exhibits the lowest stability compared to others pressure values. Therefore, at the equilibrium state, hydrogen reversibility and storage are more difficult. The best point for hydrogen storage applications among these points is point N° 3. In addition, the latter has the smallest lattice parameters, which is satisfactory for hydrogen storage systems.

DOS analysis shows that, in the valence band, various pressures influence the shape of 1s H orbitals more than that of 2p Li orbitals. Densities of states at the two peaks of 1s H orbitals corresponding to point N° 3 are lower than others. Therefore, in this point, there is a weak hybridization between 2p Li and 1s H orbitals, indicating lower stability and higher hydrogen kinetic reversibility.

## III.4 Effect of metal atom substitutions in $Li_7XH_8$ (X (AM) = Na, K, Rb and X (TM) = Ti, V, Cr) hydrides for hydrogen storage

Lithium-based hydride stability is decreased and hydrogen kinetics are improved by substituting a few lithium atoms with metal atoms. To select the most appropriate atomic substitutions in $Li_7XH_8$ (X (AM) = Na, K, Rb and X (TM) = Ti, V, Cr), which stores and releases hydrogen comfortably and abundantly, the influence of alkali (AM) and transition metal (TM) atom substitutions in Li-based hydrides is examined in the current work. The hydrides LiH and $Li_7XH_8$'s electronic and structural properties are identified. Calculated values for the formation energy and electron characteristics are used to determine how substitutions for alkali and transition metal atoms affect the stability of the hydrides $Li_7XH_8$. The adequate and acceptable atomic substitution is determined by comparing the gravimetric hydrogen storage parameter with the stability of the hydrides $Li_7XH_8$ in order to simultaneously achieve a large storage capacity and a good reversibility for the hydrogen.

The structure of lithium hydride is similar to that of NaCl (Fig. III.12 (a)). We employ a primitive supercell with dimensions equal to 1x1x2 of the initial LiH unit cell in order to examine the impact of alkali and transition metal atom substitutions. Alkali metal metal atoms (Na, K, Rb) and transition metal atoms (Ti, V, Cr) take the place of the Li atom at position (0, 0, 0) in this arrangement. The new hydride is $Li_7XH_8$ (Fig. III.12 (b)), where X is Na, K, Rb, Ti, V, or Cr. Table III provides a list of the relaxed lattice constants in the ground state (for related figures, see Appendix B). These constants nearly match earlier experimental and theoretical values for the LiH hydride (see Table III.6). There is a progressive reduction in the lattice parameters when the transition metal atoms in the $Li_7XH_8$ go from Ti to Cr. Comparing $Li_7XH_8$ to $Li_8H_8$ hydride, the alkali metal atom substitutions resulted in varied degrees of an increase in the value of the lattice parameters.

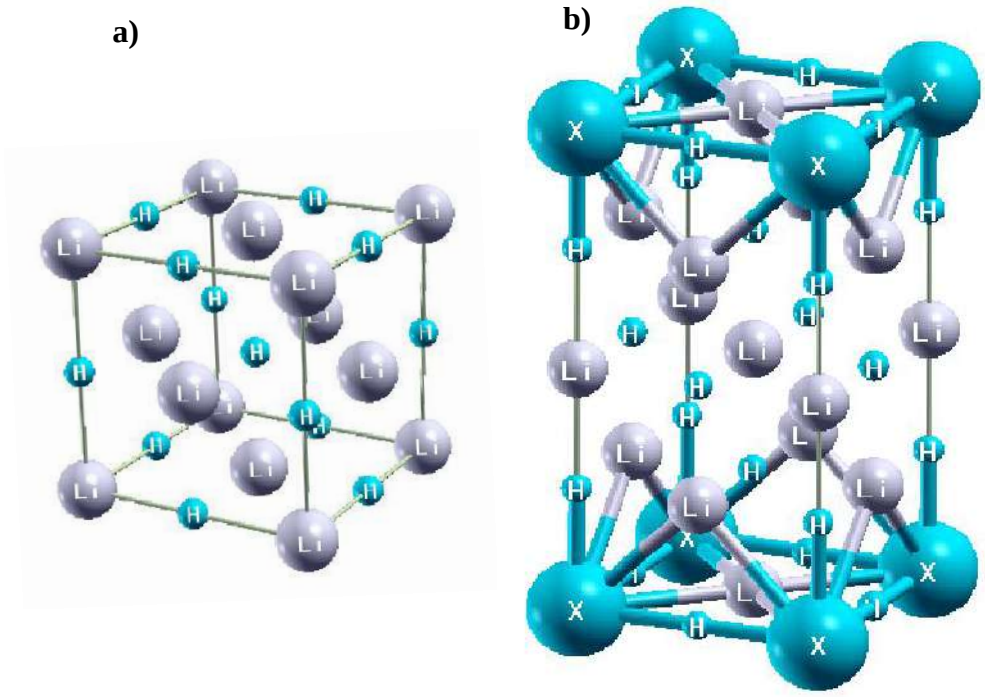


**Figure III.12:** Structure of a) LiH and b) $Li_7XH_8$ where X = Na, K, Rb, Ti, V or Cr.

**Table III.6:** Total energies of LiH and $Li_7XH_8$ as well as optimized structural parameters.

| **Hydride** | **a (Å)** | **b ( Å )** | **c ( Å )** | **$E_0$ (Ry)** |
|---|---|---|---|---|
| LiH[a] | 4.004 | 4.004 | 4.004 | -16.27 |
| LiH [25][b] | 4.083 | 4.083 | 4.083 | / |
| LiH [24][c] | 4.0695 | 4.0695 | 4.0695 | -16.23 |
| LiH [27][d] | 3.98 | 3.98 | 3.98 | / |
| $Li_8H_8$[a] | 4.004 | 4.004 | 8.008 | -130.17 |
| $Li_7NaH_8$[a] | 4.155 | 4.155 | 8.31 | -439.91 |
| $Li_7KH_8$[a] | 4.574 | 4.574 | 9.148 | -1319.15 |
| $Li_7RbH_8$[a] | 4.410 | 4.410 | 8.82 | -6077.57 |
| $Li_7TiH_8$[a] | 4.05 | 4.05 | 8.10 | -1822.58 |
| $Li_7VH_8$[a] | 3.96 | 3.96 | 7.92 | -2013.55 |
| $Li_7CrH_8$[a] | 3.92 | 3.92 | 7.84 | -2216.65 |

**a** Our work
**b** Experimental.
**c** VASP calculations.
**d** Ultrasoft pseudopotential method calculations.

### III.4.1 Formation energy

The formation energy is one of the most crucial thermodynamic parameters for researching hydrogen storage systems. This amount enables stability predictions for the systems under study. The $Li_7XH_8$ hydrides' formation energies were calculated using the following reaction formula:

$$\frac{7}{4}Li + \frac{1}{4}X + H_2 \rightarrow \frac{1}{4}Li_7XH_8 \quad \text{(III.5)}$$

The hydrides' acquired formation energies were established by:

$$E_f = \frac{1}{4}E_{Li_7XH_8} - \frac{7}{4}E_{Li} - \frac{1}{4}E_X - E_{H_2} \quad \text{(III.6)}$$

The previous chemical reaction coefficients were standardized to quantify the production energy per 1 mole of molecular $H_2$ in order to make comparisons easier. In these computations, molecular hydrogen has a total energy of 2.32 Ry [28-34]. The lattice parameters found in Ref. [35] have been used to calculate the total energies of the simple metallic elements. The impact of the alkali metal atom replacements in $Li_7XH_8$ on the formation energy is depicted in Fig. III.13. $Li_8H_8$ was found to have a formation energy value of -181.78 kJ/mol $H_2$, which is not significantly different from the value of -181 kJ/mol $H_2$ measured experimentally [36]. We can see from the graph that from Na to Rb, the formation energies of $Li_7XH_8$ (X=Li, Na, K, or Rb) rapidly decrease. $Li_8H_8$ has a much higher formation energy than other hydrides, making hydrogen storage and restitution more challenging and energy-intensive than other substitutes. The hydride formed by the substitution of a Rb atom, $Li_7RbH_8$, has the lowest formation energy. As a result, this hydride stores and releases hydrogen more quickly than the hydrides $Li_8H_8$, $Li_7NaH_8$ and $Li_7KH_8$. Fig. III.14 shows how the substitution of a transition metal atom for $Li_7XH_8$ (where X=Li, Ti, V, or Cr) affects the formation energy. The formation energy is reduced as a result of the metal substitutions from Ti to Cr. Although $Li_7CrH_8$ is the least stable hydride in comparison to the others, it offers the best hydrogen storage and restitution.

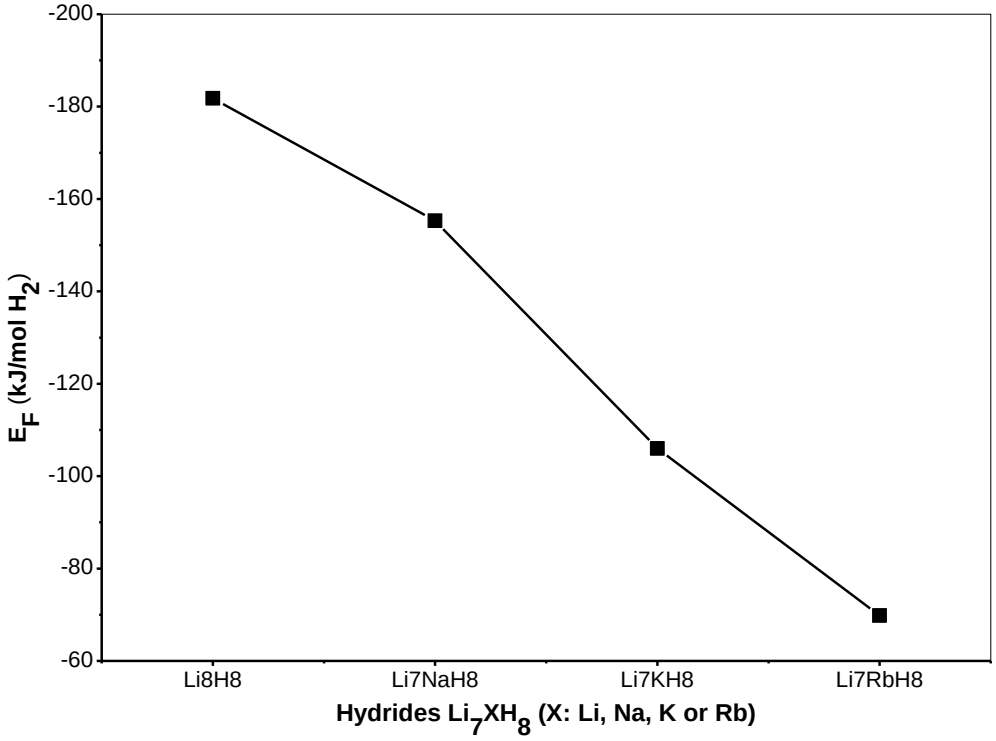


**Figure III.13:** Variation of the formation energy as a function of the alkali metal atom substitutions in $Li_7XH_8$.

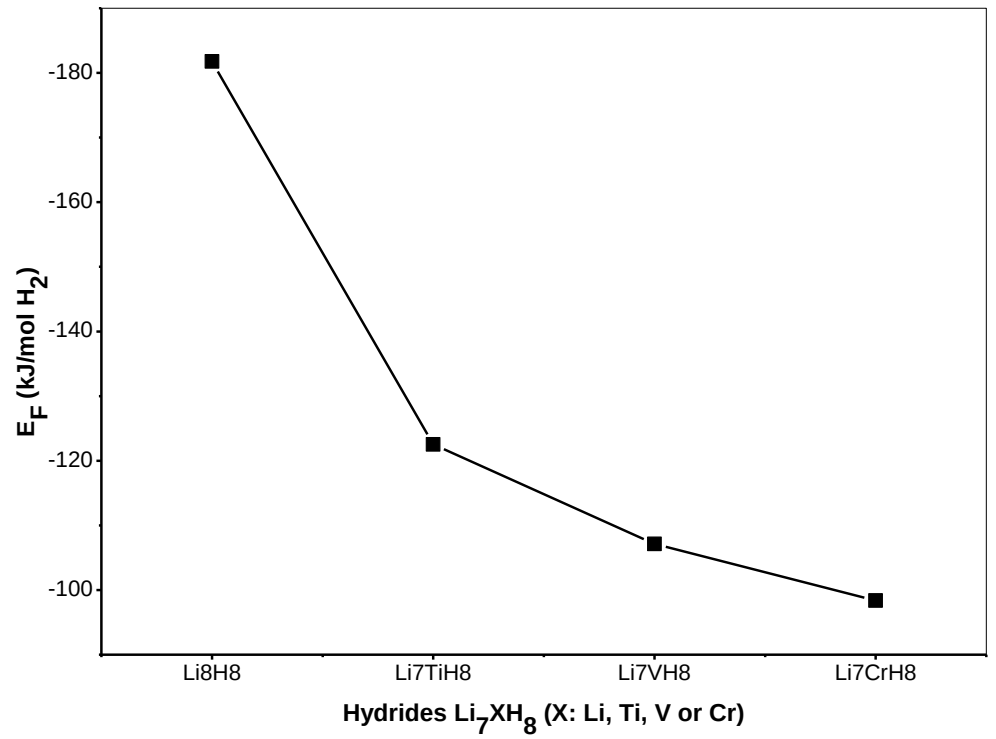


**Figure III.14:** Variation of the formation energy as a function of the transition metal atom substitutions in $Li_7XH_8$.

### III.4.2 Gravimetric hydrogen storage density

The hydrogen ratios contained in the hydrides $Li_7XH_8$ are computed using the following formula to establish their gravimetric storage density of hydrogen:

$$\text{Gravimetry (wt.\%)} = \frac{8M_H}{8M_H+7M_{Li}+M_X} \quad \text{(III.7)}$$

$M_X$, $M_{Li}$ and $M_H$ stand for the molar masses of the X metal, lithium and hydrogen, respectively. The gravimetric hydrogen storage density falls as a function of the replacement from Na to Rb, as seen in Fig. III.15. $Li_8H_8$ holds 12.5 wt. % of the most hydrogen. From the Ti substitution to the Cr one, the gravimetric hydrogen storage density declines at a somewhat slow rate (Fig. III.16). $Li_7CrH_8$, the least stable of the transition metal substituted hydrides, has a hydrogen gravimetry of 7.42 wt. %, which is comparable to $Li_7VH_8$'s and $Li_7TiH_8$'s respective values of 7.49 and 7.71 wt. %. While having a similar relative fall in formation energy, the transition metal substituted hydrides exhibit a smaller relative decline in the gravimetric hydrogen storage density than the alkali metal substituted ones. In terms of hydrogen gravimetric density, $Li_7CrH_8$ is comparable to magnesium hydride ($MgH_2$), which has a high gravimetric density (7.65 wt%) and is one of the most promising materials for applications involving hydrogen solid storage [26]. The same findings about the relative decrease in gravimetric hydrogen storage density for the system doped with 6.25% transition metals ($Mg_{15}MH_{32}$ where M = Ti, Sc and Zn) were made [26].

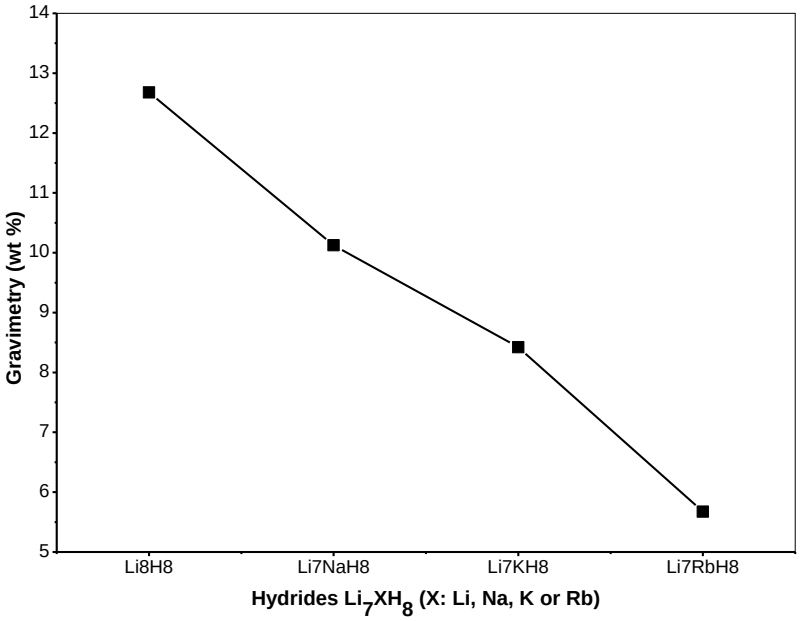


**Figure III.15:** Gravimetric hydrogen storage density versus $Li_7XH_8$ hydride (X=Li, Na, K or Rb).

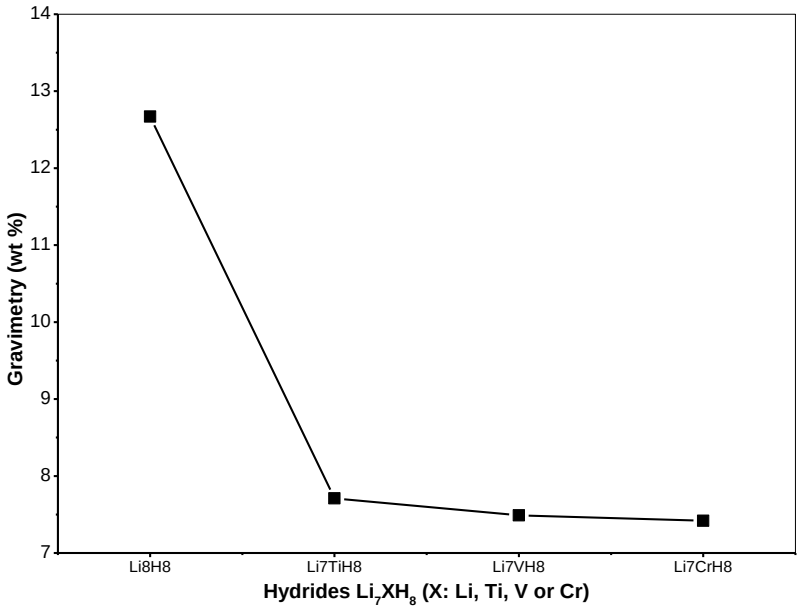


**Figure III.16:** Gravimetric hydrogen storage density versus $Li_7XH_8$ hydride (X=Li, Ti, V or Cr).

### III.4.3 Density of states

Density of states analysis could also be used to comprehend how the metal atom substitutions in the $Li_7XH_8$ hydride improved hydrogenation performance. Figs. III.17-III.20 provide the partial and total densities of states for the Li8H8 and $Li_7XH_8$ hydrides. In the valence band of the Li8H8 hydride, the 2p Li and 1s H orbitals are highly hybridized, whereas the 2s Li and 1s H orbitals are weakly hybridized (Fig. III.17 (a)). In comparison to 3s, 4s, and 5s X (AM) and 1s H orbitals,

it was discovered that the high hybridization between 3p, 4p, and 5p X (AM) and 1s H orbitals (shown in Fig. III.17) was more significant (not shown here). The calculated energy gap of the $Li_8H_8$ was determined to be $E_g$ = 3.207 eV, which is close to the predicted value $E_g$(LiH) = 3.02 eV, according to calculations made with the VASP programme [37]. Experimental results show that this band gap is 4.99 eV at 4.2 K [38]. The hybridization between 2p Li - 1s H and X (= 3p, 4p and 5p AM, 3d TM) - 1s H and X - 2p Li gradually decreases and gradually increases as a result of the atomic substitutions from Na to Rb and from Ti to Cr in these hydrides (Fig. III.17 and Fig. III.18). This suggests that the bonding between X 1s H and X 2p Li will stabilize, whereas the bond between X 1s H and X 2p Li will destabilize.

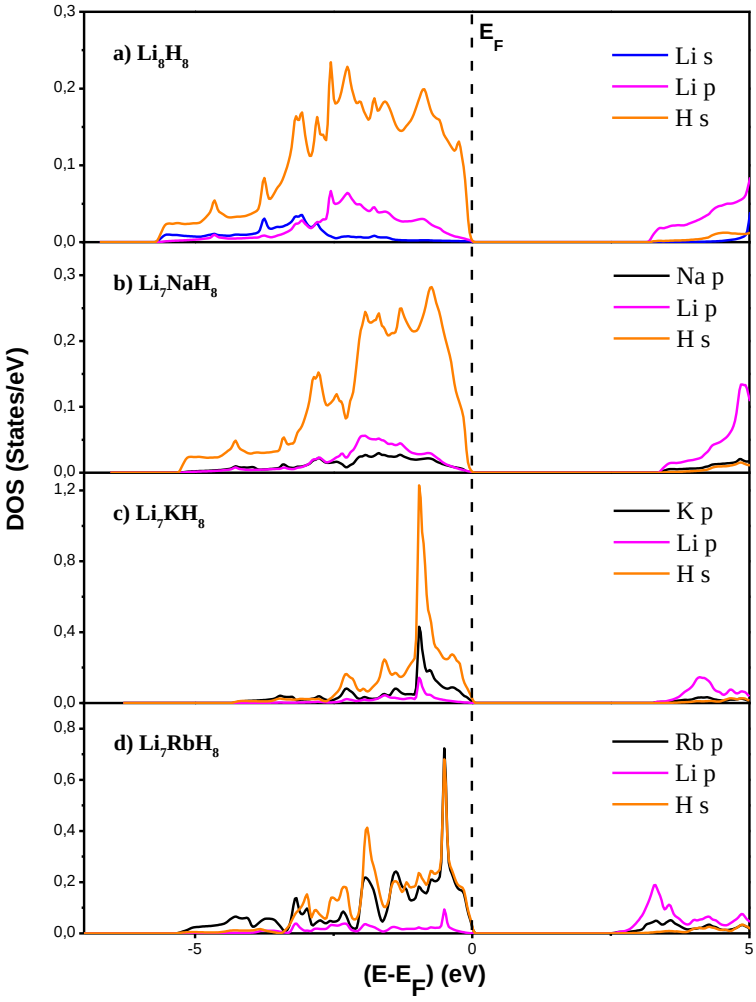


**Figure III.17:** Partial density of states for **a)** $Li_8H_8$, **b)** $Li_7NaH_8$, **c)** $Li_7KH_8$ and **d)** $Li_7RbH_8$.

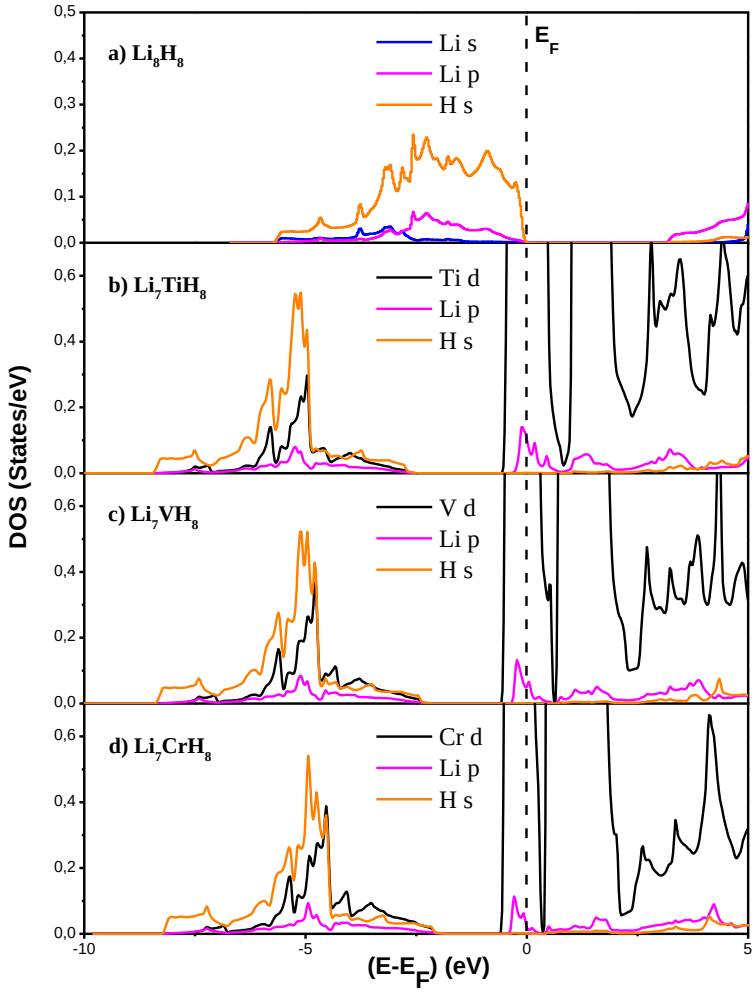


**Figure III.18:** Partial density of states of **a)** $Li_8H_8$, **b)** $Li_7TiH_8$, **c)** $Li_7VH_8$ and **d)** $Li_7CrH_8$.

$Li_8H_8$, $Li_7NaH_8$, $Li_7K_8$, $Li_7RbH_8$ and $Li_7KH_8$'s respective alkali metal substitution hydrides were discovered to have energy gaps of 3.207 eV, 3.399 eV, 3.306 eV and 2.507 eV. Since these gaps are greater than 1 eV, the hydrides $Li_8H_8$, $Li_7NaH_8$, $Li_7K_8$ and $Li_7RbH_8$ have an insulating character (Fig. III.19).

We see that the density of states (in the 2p Li and 1s H orbitals region of the valence band) gradually decreases as a result of the atomic substitution from Na to Rb for $Li_7XH_8$ (Fig. III.17). This decrease has an impact on the number of electrons that contribute to the Li-H bonds at absolute zero temperatures. The optimum hydride in this alkali family for storing and releasing hydrogen is $Li_7RbH_8$.

Due to a Fermi level that is present in the conduction band, the $Li_7TiH_8$, $Li_7VH_8$ and $Li_7CrH_8$ hydrides have a conducting nature (Fig. III.20). A gap in the valence band gradually gets smaller as a result of the atomic switch from Ti to Cr for $Li_7XH_8$ hydrides (below EF). It causes the

density of states in the valence band to gradually decline, especially in the 2p Li- 1s H orbital region (Fig. III.18). Although $Li_7CrH_8$ is less stable than the other transition metal atom substitution hydrides under study, it can store and release hydrogen more rapidly. The geometry of the conduction band, which includes the band gap, is also seen to shift towards lower energies for the $Li_8H_8$ hydride after transition metal substitutions. The insulating hydride $Li_8H_8$ was transformed into conducting hydrides as a result of the three transition metal substitutions.

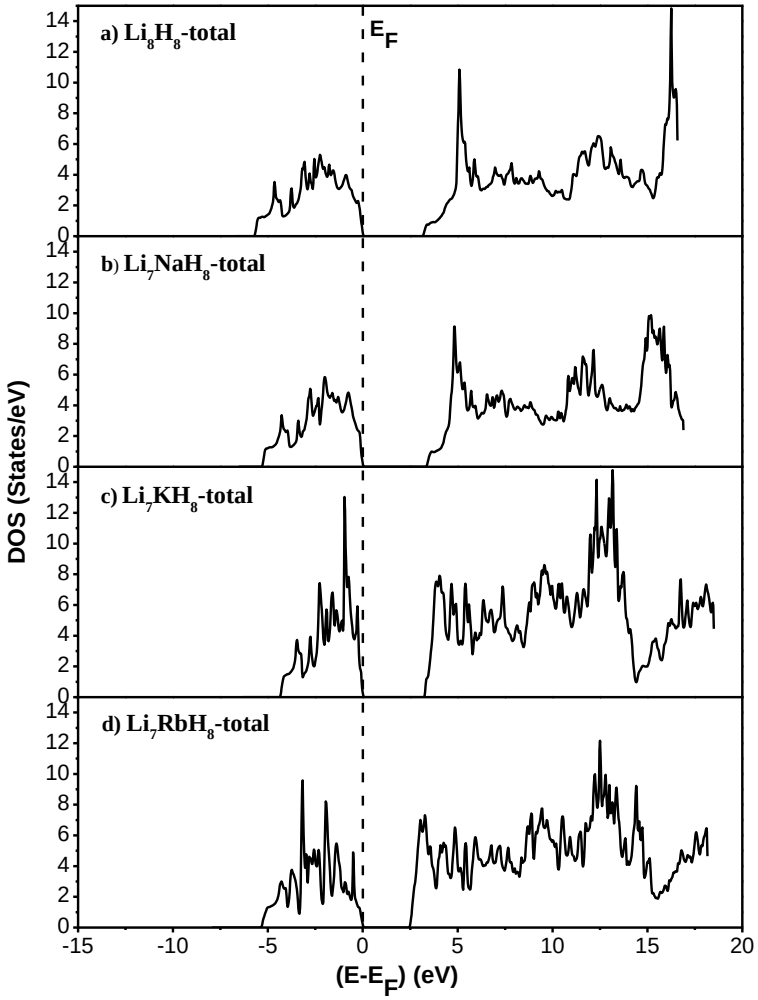


**Figure III.19:** Total density of states of **a)** $Li_8H_8$, **b)** $Li_7NaH_8$, **c)** $Li_7KH_8$ and **d)** $Li_7RbH_8$.

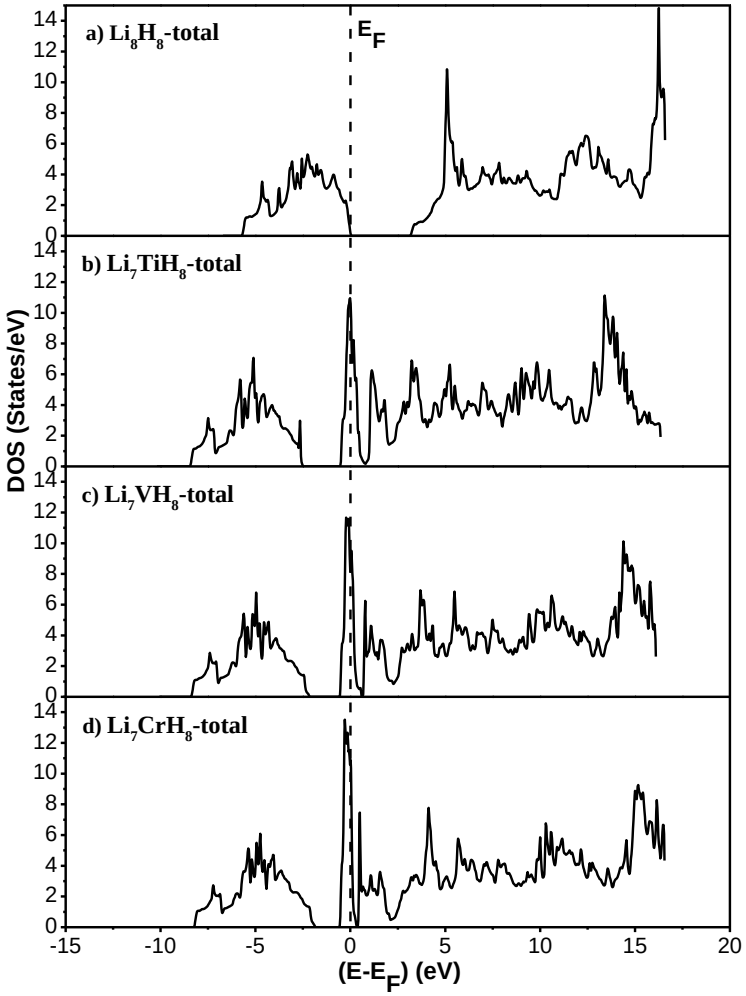


**Figure III.20:** Total density of states of **a)** $Li_8H_8$, **b)** $Li_7TiH_8$, **c)** $Li_7VH_8$ and **d)** $Li_7CrH_8$.

## III.4.4 Electron density

Fig. III.21 displays contour maps of the electron density distribution on the Li8H8 hydride's (001) and (100) atomic planes. Indicating that the interaction between lithium and hydrogen is ionic in nature, the electron density distributions on the planes show roughly spherical symmetric charge distributions around atomic sites. Figs. III.22 and III.23, respectively, show the contour maps of the electron density distribution on the (001) and (100) atomic planes of the $Li_7XH_8$ hydrides. In the alkali and transition metal substituted hydrides, respectively, the charge distributions between X (= AM or TM) and H rise steadily from Na to Rb and from Ti to Cr substitution. An improvement in the covalent nature of the ionic interaction between X and H accounts for this increase in electron density. While transitioning from Na to Rb and from Ti to

Cr substitution in the alkali and transition metal substituted hydrides, respectively, the ionic interaction between X-H and Li-H gradually deteriorates. The stability of these systems depends on the amount of charge that the hydrogen receives. The stability declines when the latter decreases [33]. As a result, the charge that H originally received from Li lowers and contributes to strengthening the partial covalent interaction between X and H. As a result, the relative stability of the alkali and transition metal substituted hydrides reduces from Na to Rb and from Ti to Cr substitution, respectively.

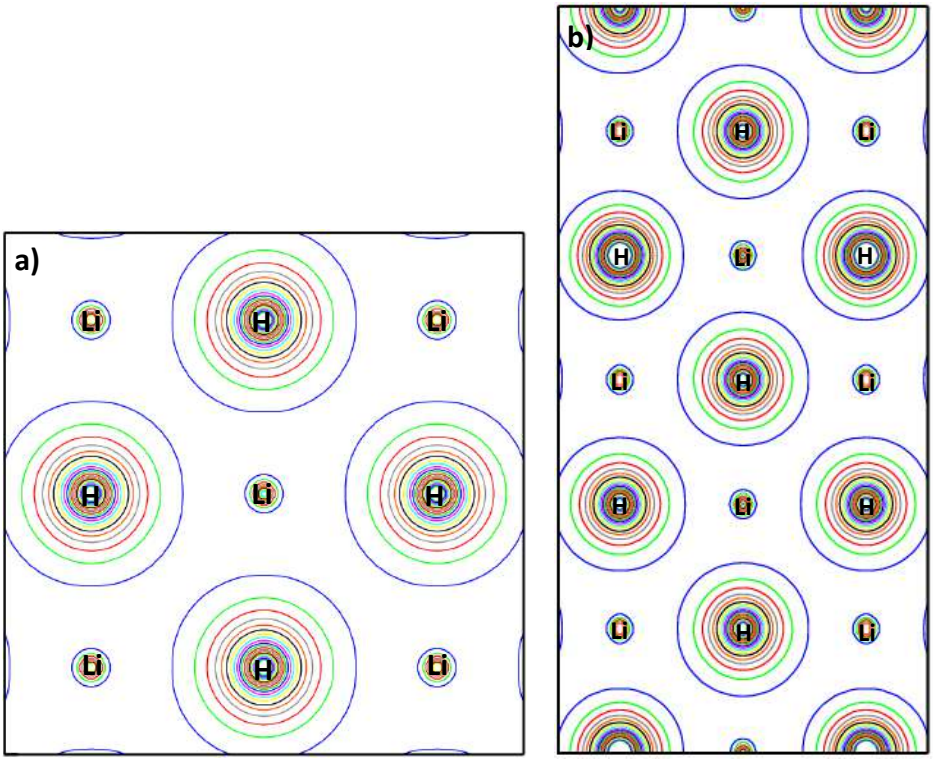


**Figure III.21:** Contour maps of the electron density distributions in the **a)** (001), **b)** (100) atomic planes of the $Li_8H_8$ hydride.

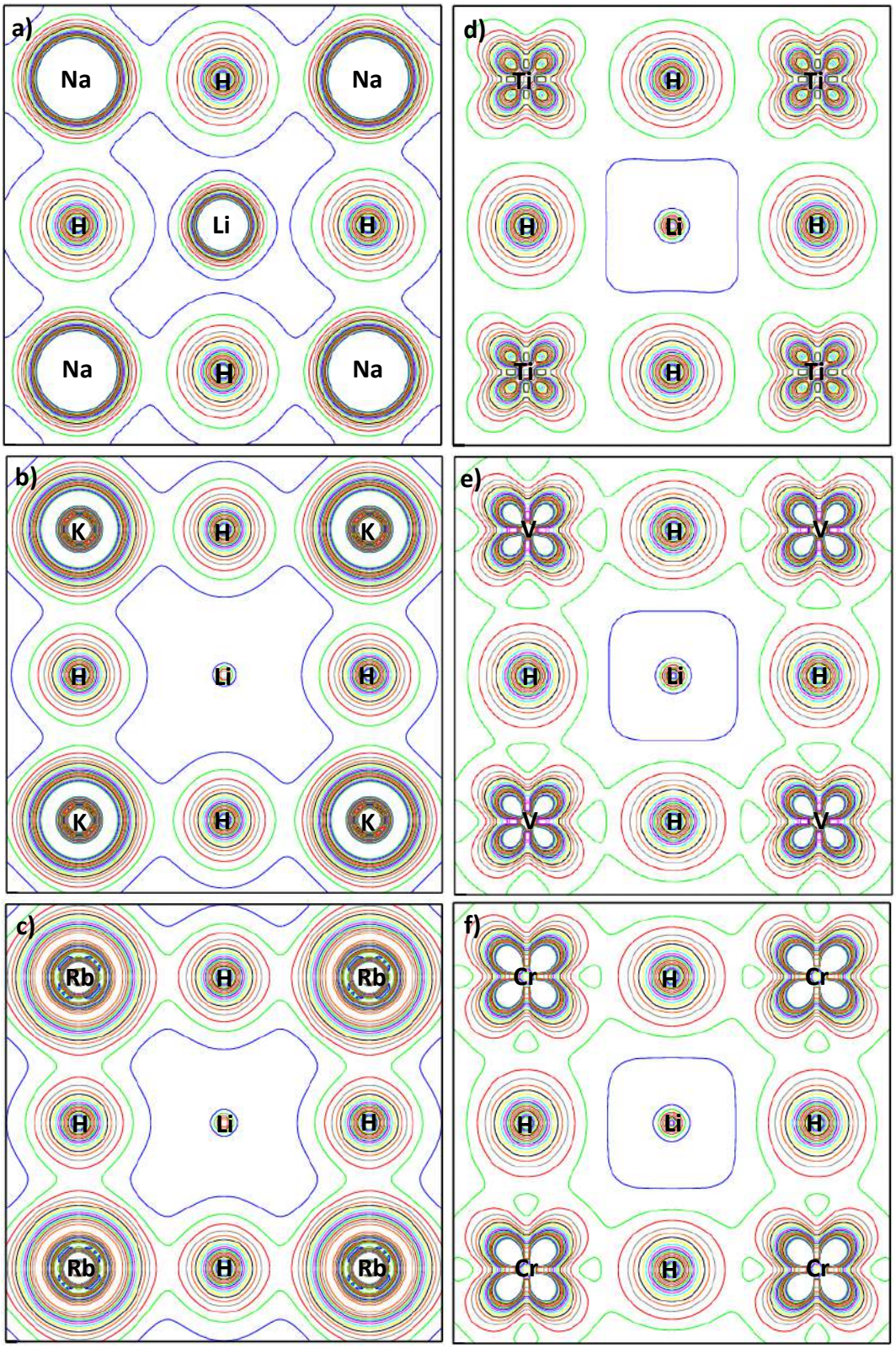


**Figure III.22:** Contour maps of the electron density distributions in the (001) atomic plane of the **a)** $Li_7NaH_8$, **b)** $Li_7KH_8$, **c)** $Li_7RbH_8$, **d)** $Li_7TiH_8$, **e)** $Li_7VH_8$ and **f)** $Li_7CrH_8$.

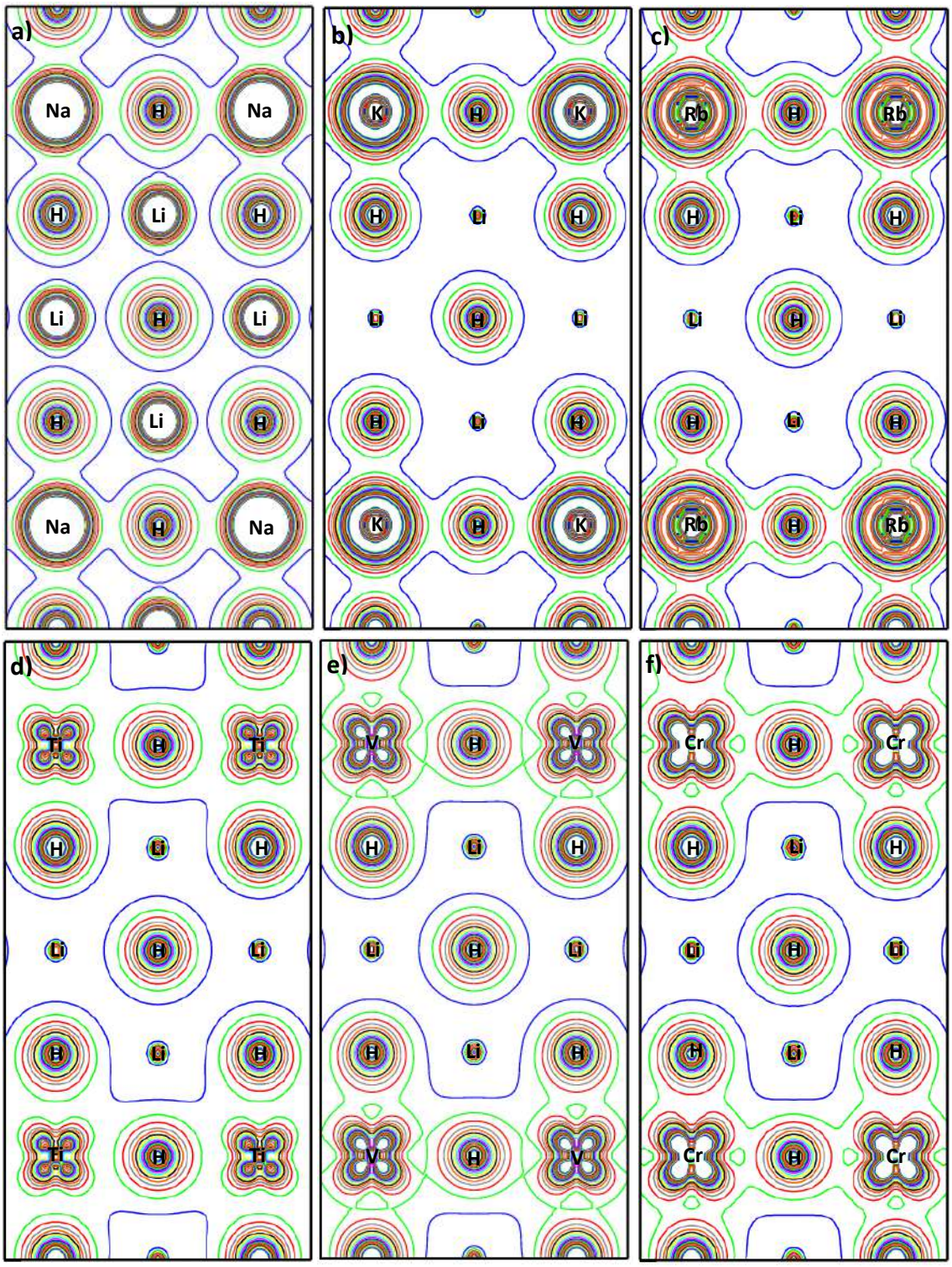


**Figure III.23:** Contour maps of the electron density distributions in the (100) atomic plane of the **a)** $Li_7NaH_8$, **b)** $Li_7KH_8$, **c)** $Li_7RbH_8$, **d)** $Li_7TiH_8$, **e)** $Li_7VH_8$ and **f)** $Li_7CrH_8$.

### III.4.5 Conclusion

In order to improve hydrogen storage capacity, the impact of alkali and transition metal atom substitutions in Li-based hydrides ($Li_7XH_8$ with X(AM) = Na, K, Rb and X(TM) = Ti, V, Cr) was examined in this section. The WIEN2k program, which is based on the DFT and FP-LAPW approach, was used to carry out this investigation. The LiH hydride's computed structural parameters were discovered to be within the margins of previously calculated theoretical and experimental values. Whereas the transition metal atom substitutions in the $Li_7XH_8$ have steadily reduced the lattice parameters compared to the $Li_8H_8$ hydride, the alkali metal atom substitutions have raised the lattice parameters in comparison to the $Li_8H_8$ hydride.

According to the computed formation energy estimates, the $Li_7XH_8$ hydride's stability gradually degrades as a result of the transition metal substitution from Ti to Cr and the alkali substitution from Na to Rb. $Li_7CrH_8$ has been shown to be the least stable phase among all alkali and transition metal atom exchanges. The Li7CrH8 hydride also exhibits decreased lattice parameters compared to the others. The gravimetric hydrogen storage density in the transition metal substituted hydrides diminishes at a rather slow rate from Ti to Cr substitution. While having a similar percentage fall in formation energy, the gravimetric hydrogen storage density of the transition metal substituted hydrides declines more slowly than that of the alkali metal substituted ones.

The explanation of our findings is supported by assessments of the electron density and density of states. The insulating Li8H8 hydride was transformed into conducting hydrides as a result of the three transition metal substitutions.

## III.5 Effect of metal atom substitutions in $Li_3XH_4$ (X (AM) = Na, K, Rb and X (TM) = Ti, V, Cr) hydrides for hydrogen storage

A similar study, as in $Li_7XH_8$ hydrides, was applied on $Li_3XH_4$ (X (AM) = Na, K, Rb and X (TM) = Ti, V, Cr) to compare, qualitatively and quantitatively, the $Li_7XH_8$ and $Li_3XH_4$ hydrides. The LiH_225 has fcc crystal lattice which contains four formula units (4/fu). The structure of $Li_3XH_4$ is similar to the LiH_225 structure excepting the Li (0, 0, 0) atom which is replaced by an X atom (Fig. III.24). Relaxed lattice parameters and total energies in the ground state are listed in Table III.7 (for related figures, see Appendix B). The alkali metal atom substitutions in the $Li_3XH_4$ show a gradual increase in the value of lattice parameters from Na to Rb substitution. The lattice parameters in alkali metal atom substitutions in the $Li_3XH_4$ hydrides are higher than those of $Li_4H_4$ hydride. The transition metal atom substitutions in the $Li_3XH_4$ from Ti to Cr show a gradual decrease in lattice parameters. The lattice parameters of both $Li_3VH_4$ and $Li_3CrH_4$ are lower than that of $Li_4H_4$ hydride. The same behavior was observed in lattice parameters of the $Li_3XH_4$ hydrides as well as in those of the $Li_7XH_8$ hydrides.

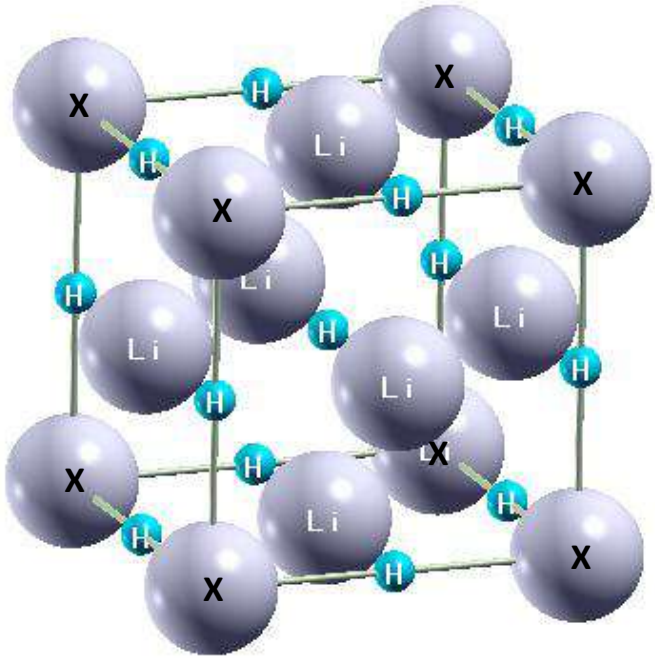


**Figure III.24:** Structure of $Li_3XH_4$ where X = Na, K, Rb, Ti, V or Cr.

**Table III.7:** Calculated structure parameters and total energies of $Li_3XH_4$.

| Hydride | a (Å) | b ( Å ) | c ( Å ) | $E_0$ (Ry) |
|---|---|---|---|---|
| $Li_4H_4$ | 4.004 | 4.004 | 4.004 | -65.0867 |
| $Li_3NaH_4$ | 4.284 | 4.284 | 4.284 | -374.8439 |
| $Li_3KH_4$ | 4.711 | 4.711 | 4.711 | -1254.1312 |
| $Li_3RbH_4$ | 4.945 | 4.945 | 4.945 | -6012.7782 |
| $Li_3TiH_4$ | 4.048 | 4.048 | 4.048 | -1757.5141 |
| $Li_3VH_4$ | 3.935 | 3.935 | 3.935 | -1948.4668 |
| $Li_3CrH_4$ | 3.865 | 3.865 | 3.865 | -2151.5666 |

### III.5.1 Formation energy

The formation energy values of the $Li_3XH_4$ hydrides were calculated using this chemical reaction:

$$\frac{3}{2}\mathrm{Li} + \frac{1}{2}\mathrm{X} + \mathrm{H_2} \rightarrow \frac{1}{2}\mathrm{Li_3XH_4} \qquad \text{(III.8)}$$

The obtained formation energies of the $Li_3XH_4$ hydrides were determined per 1 mole of $H_2$ by:

$$\mathrm{E_f} = \frac{1}{2}\mathrm{E_{Li_3XH_4}} - \frac{3}{2}\mathrm{E_{Li}} - \frac{1}{2}\mathrm{E_X} - \mathrm{E_{H_2}}. \qquad \text{(III.9)}$$

$E_{Li3XH4}$, $E_{Li}$, $E_X$ and $E_{H2}$ represent the total energy of $Li_3XH_4$ hydride, lithium metal, X metal and $H_2$ molecular, respectively. There is a uniform decrease in formation energy values for each type of atom substitution from the $Li_7XH_8$ to $Li_3XH_4$ hydride (Fig. III.25). In order to illustrate this uniform decrease in formation energy values which is happening when the effect of atomic substitution on a small number of atoms (3 Li and 4 H in $Li_3XH_4$) is much stronger than on a large number of atoms (7 Li an 8 H in $Li_7XH_8$). Increasing the substituted atoms number in hydrides leads obviously to an increasing effect on the remaining atoms. In addition, the type of substituted atoms has an effect on formation energy values. Therefore, the number and the type of substituted atoms have an effect on the stability and consequently on the hydrogen storage performance.

It is noted in the $Li_3XH_4$ a progressive decrease in formation energy values for alkali metal atom substitutions from Na to Rb and for transition metal atom substitutions from Ti to Cr. The most instable hydride suitable for hydrogen storage applications compared to others is $Li_3CrH_4$ which

has the lowest formation energy value (-11 kJ/mol $H_2$). The latter is less than that in the ideal formation energy range from -20 to -40 kJ/mol $H_2$ used in fuel cell applications [40-43]. The only two substitutions hydrides which fall in this range are the $Li_3RbH_4$ and $Li_3VH_4$ hydrides.

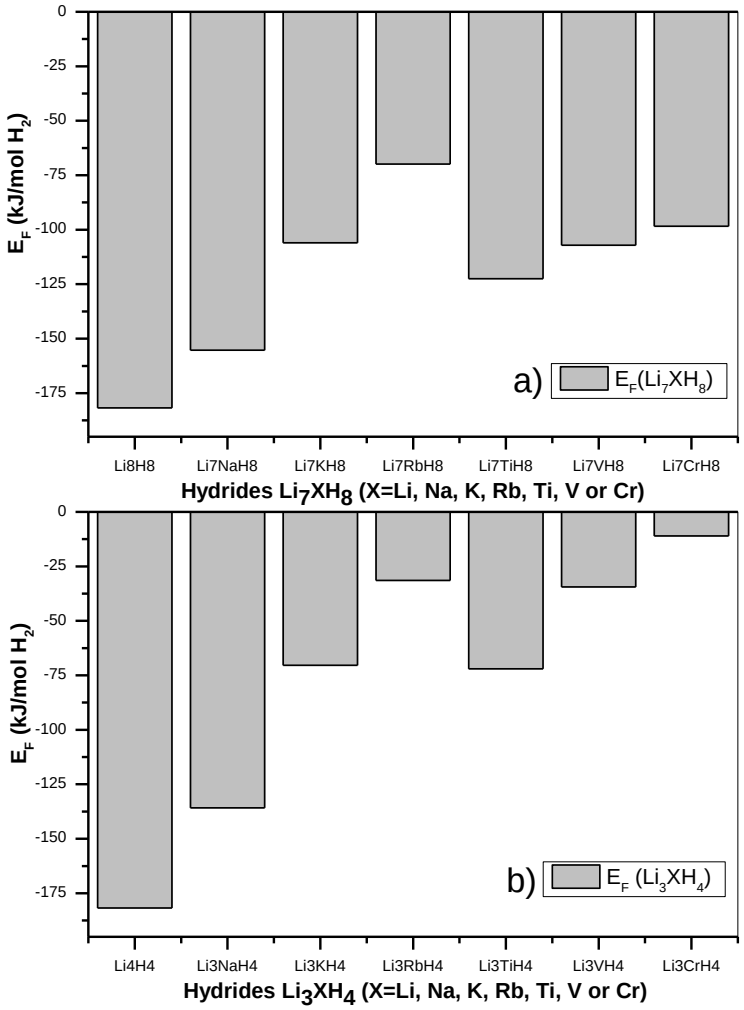


**Figure III.25:** Formation energies versus a) $Li_7XH_8$ and b) $Li_3XH_4$ hydrides (X=Li, Na, K, Rb, Ti, V or Cr).

### III.5.2 Gravimetric hydrogen storage density

For $Li_3XH_4$ the gravimetric storage of hydrogen is calculated by:

$$\text{Gravimetry (wt.\%)} = \frac{4M_H}{4M_H+3M_{Li}+M_X}, \quad \text{(III.10)}$$

where, respectively, $M_H$, $M_{Li}$ and $M_X$ denote the molar masses of hydrogen, lithium and the X metal. Fig. III.26 exhibits the gravimetric hydrogen storage for both $Li_7XH_8$ (a) and $Li_3XH_4$ (b) as a function of substitution from Na to Rb and from Ti to Cr, respectively. The gravimetric storage of hydrogen decreases uniformly from $Li_7XH_8$ to $Li_3XH_4$ for the alkali and transition metal atom substitutions. Excepting for this uniform decrease, the same behavior of the gravimetric storage of hydrogen in both $Li_7XH_8$ to $Li_3XH_4$ is noted for all metal atom substitutions.

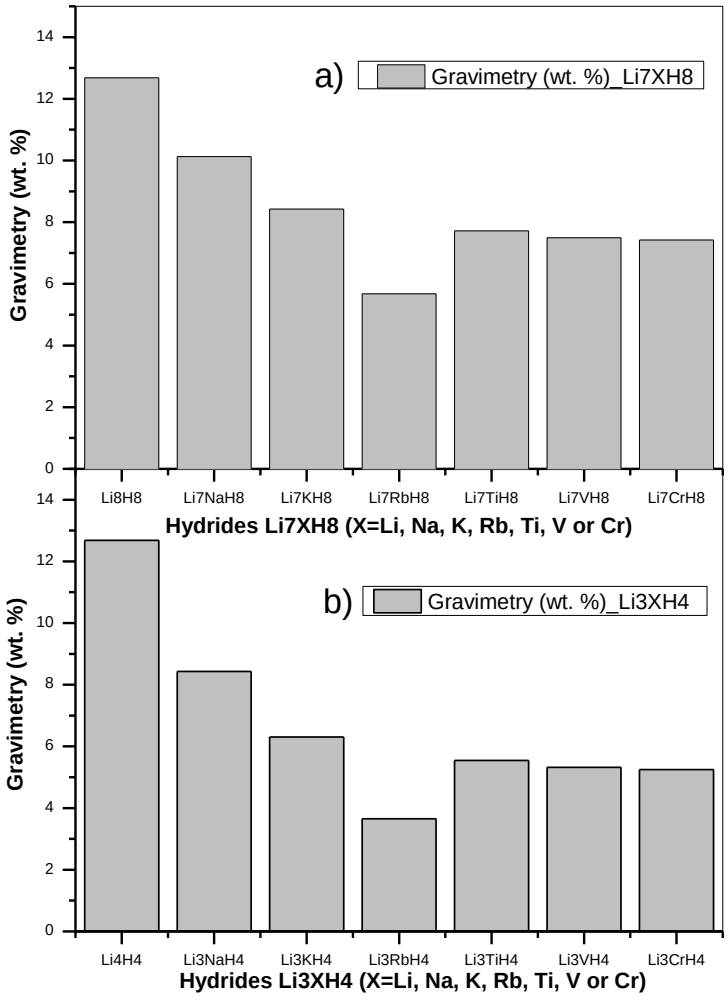


**Figure III.26:** Gravimetric hydrogen storage density versus a) $Li_7XH_8$ and b) $Li_3XH_4$ hydrides (X=Li, Na, K, Rb, Ti, V or Cr).

### III.5.3 Density of states

Total and partial densities of states for the $Li_4H_4$ and $Li_3XH_4$ hydrides are displayed in Figs. III.27, III.28 and III.29. $Li_3XH_4$ hydrides show the same electronic behavior as $Li_7XH_8$ hydrides, where $Li_4H_8$, $Li_3NaH_4$, $Li_3KH_4$ and $Li_3RbH_4$ have an insulating character while $Li_3TiH_4$, $Li_3VH_4$ and $Li_3CrH_4$ have a conducting character (Fig. III.27). Energy gaps of the alkali metal substitution hydride for $Li_3NaH_4$, $Li_3KH_4$ and $Li_3RbH_4$ were determined to be 3.808 eV, 3.090 eV and 2.537 eV, respectively. Partial densities of states for alkali substitution hydrides $Li_3XH_4$ in the valence band indicate an increasing hybridization between X (AM) and 1s H orbitals from Na to Rb substitution (Fig. III.28). The increase in hybridization between X (AM) and 1s H orbitals in $Li_3XH_4$ is relatively higher than that in $Li_7XH_8$. In addition, the density of p Li orbitals decreases in the valence band from Na to Rb substitution in $Li_3XH_4$ hydrides which is explained by a gradual decrease in hybridization between p Li and 1 s H orbitals.

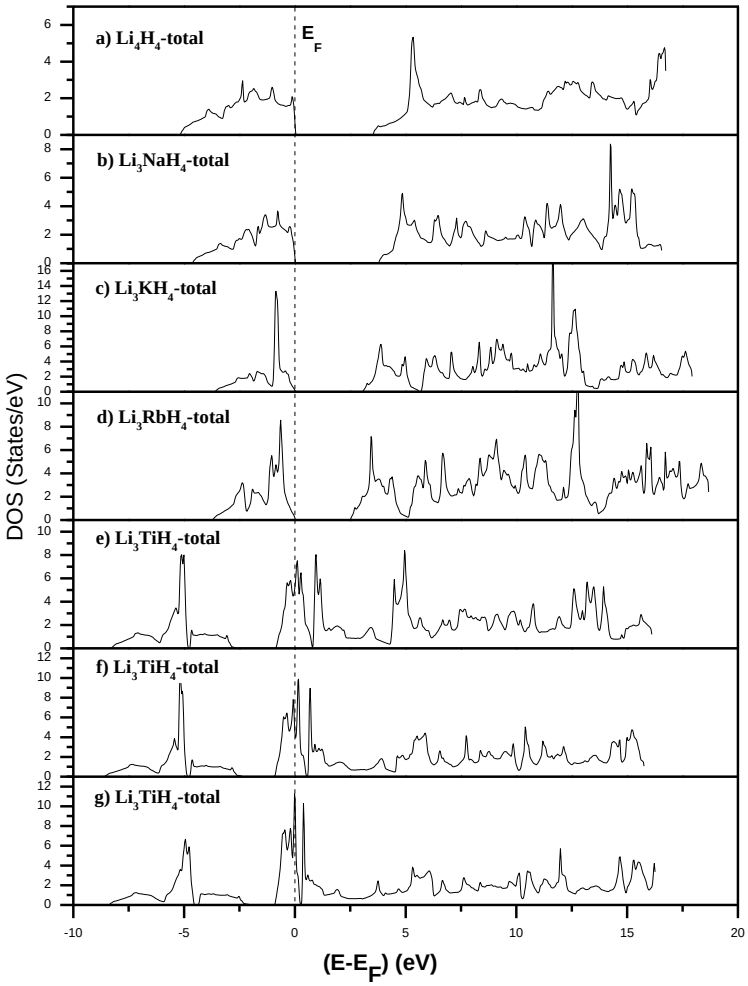


**Figure III.27:** Total density of states of **a)** $Li_4H_4$, **b)** $Li_3NaH_4$, **c)** $Li_3KH_4$, **d)** $Li_3RbH_4$, **e)** $Li_3TiH_4$, **f)** $Li_3VH_4$ and **g)** $Li_3CrH_4$.

As in the $Li_7XH_8$, transition metal substitution hydrides $Li_3XH_4$ display, in the valence band, a gradual increase in hybridization between X (TM) and 1s H orbitals and a gradual decrease in hybridization between p Li and 1s H orbitals from Ti to Cr substitution (Fig. III.29). In this case, both hybridization reactions in $Li_3XH_4$ hydrides are higher than those in $Li_7XH_8$ hydrides.

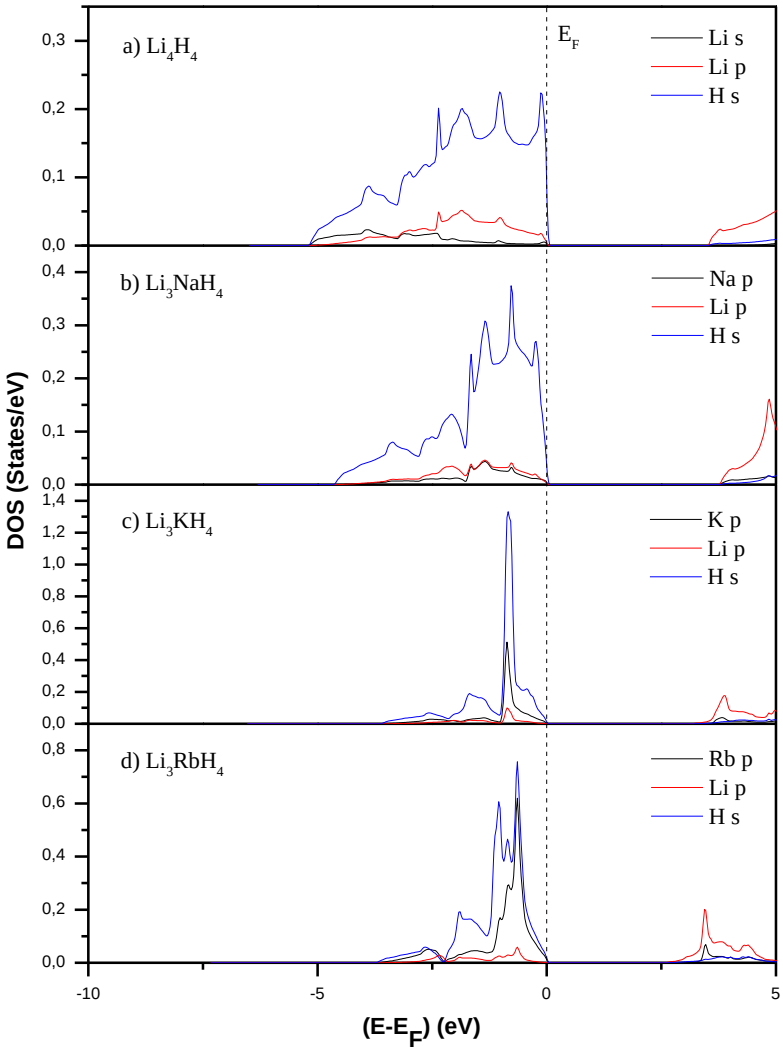


**Figure III.28:** Partial density of states for **a)** $Li_4H_4$, **b)** $Li_3NaH_4$, **c)** $Li_3KH_4$ and **d)** $Li_3RbH_4$.

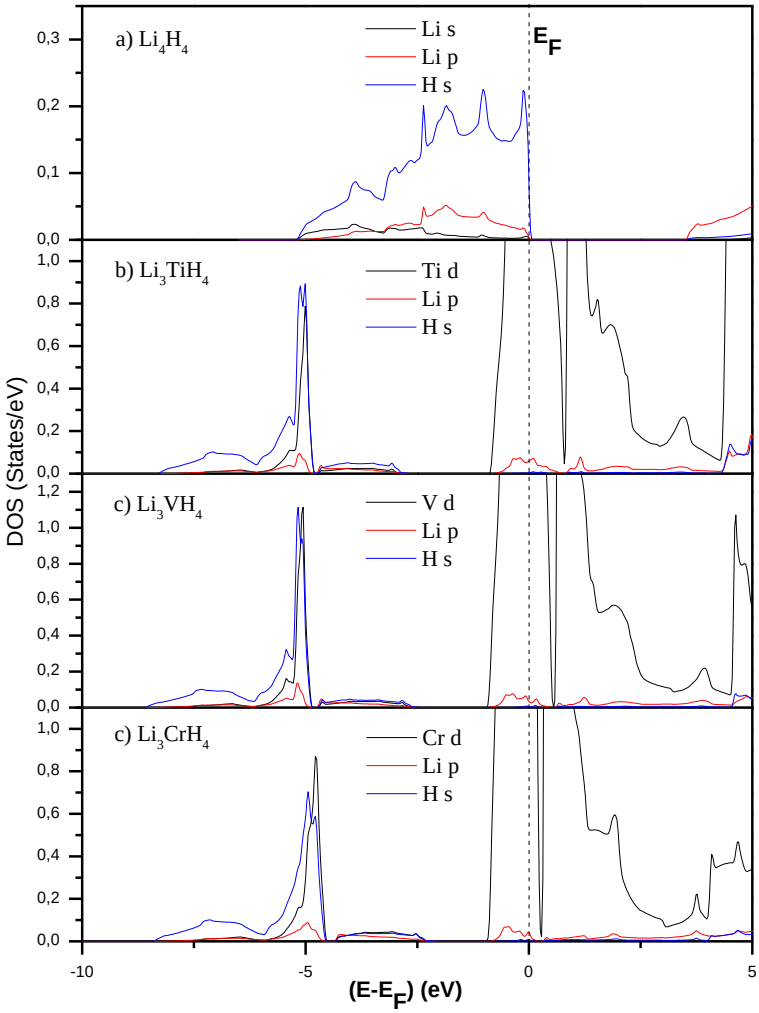


**Figure III.29:** Partial density of states of **a)** $Li_4H_4$, **b)** $Li_3TiH_4$, **c)** $Li_3VH_4$ and **d)** $Li_3CrH_4$.

### III.5.4 Electron density

For the $Li_4H_4$ hydride, contour pictures of the electron density distribution on the (100) atomic planes are shown in Fig. III.30. Ionic nature between lithium and hydrogen is indicated by the charge distribution on the plane, which displays roughly spherical symmetric distributions around atomic sites. For $Li_3XH_4$ hydrides, the contour maps of the electron density distribution on the (100) atomic plane are presented in Figs. III.31, III.32 with $\Delta\rho$=0.1 and $\Delta\rho$=0.05 respectively. In the alkali and transition metal substituted hydrides, respectively, the electron density distributions in the region between X (= AM or TM) and H steadily rise from Na to Rb and from Ti to Cr substitution. This modification in charge distribution is demonstrated by an increase of an existing covalent force bonding between X and Li and between X and H, which results in a decrease in an ionic force bond between Li and H. It seems that X atoms attract Li and H atoms in order to reduce the stress between Li and H atoms. The latter diminishes as the substitutions in the alkali and transition metal substituted hydrides, respectively, move from Na to Rb and from Ti to Cr. In a first approximation, the charge distributions on the (100) atomic plane look similar in both $Li_3XH_4$ and $Li_7XH_8$ hydrides.

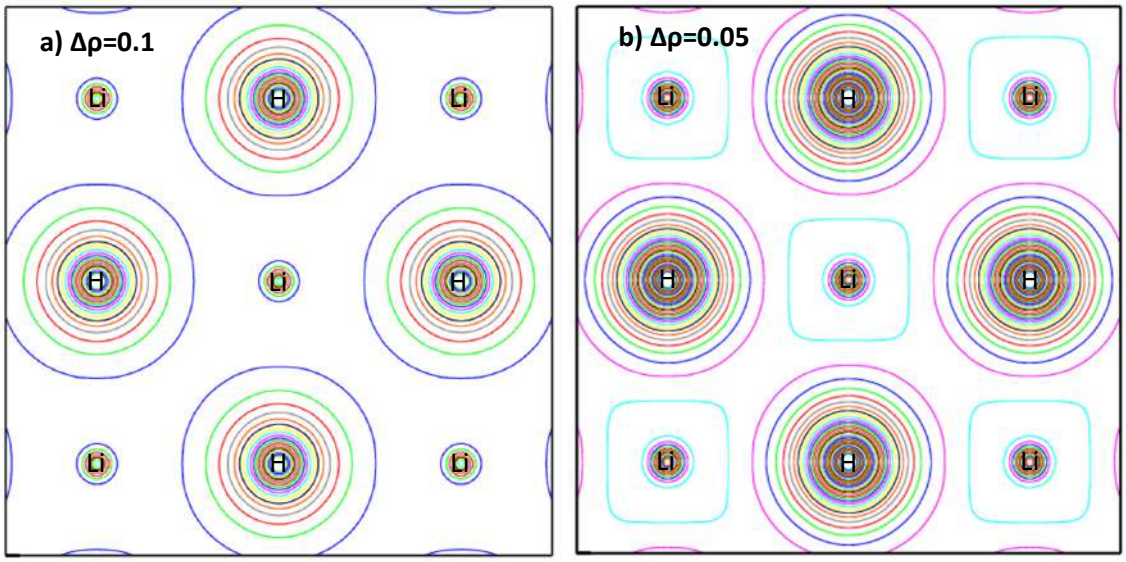


**Figure III.30:** Contour maps of the electron density distributions in the (100) atomic plane of the $Li_4H_4$ hydride for a) $\Delta\rho$=0.1 and b) $\Delta\rho$=0.05.

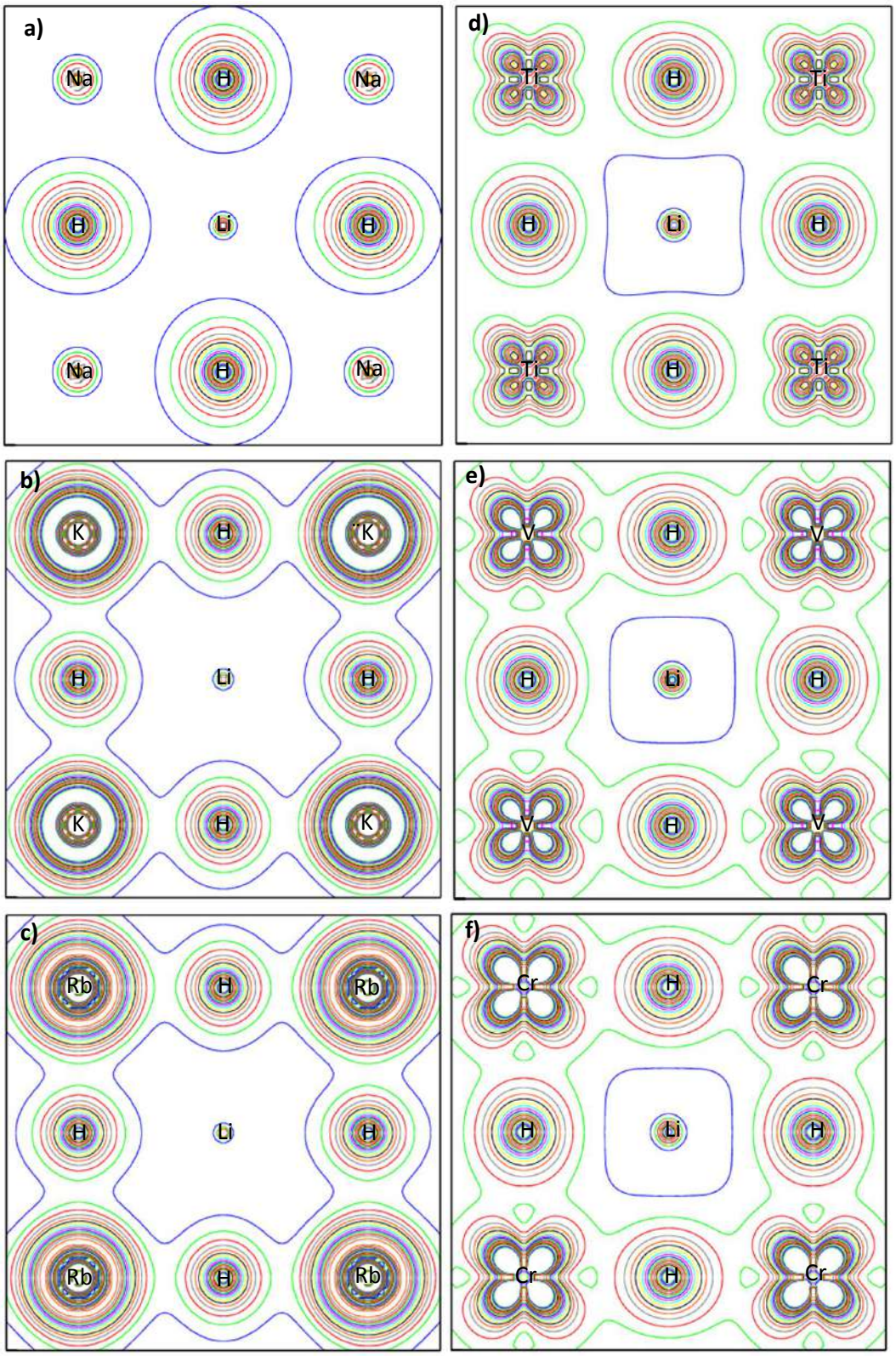


**Figure III.31:** Contour maps of the electron density distributions in the (100) atomic plane of the **a)** $Li_3NaH_4$, **b)** $Li_3KH_4$, **c)** $Li_3RbH_4$, **d)** $Li_3TiH_4$, **e)** $Li_3VH_4$ and **f)** $Li_3CrH_4$ for $\Delta\rho$=0.1.

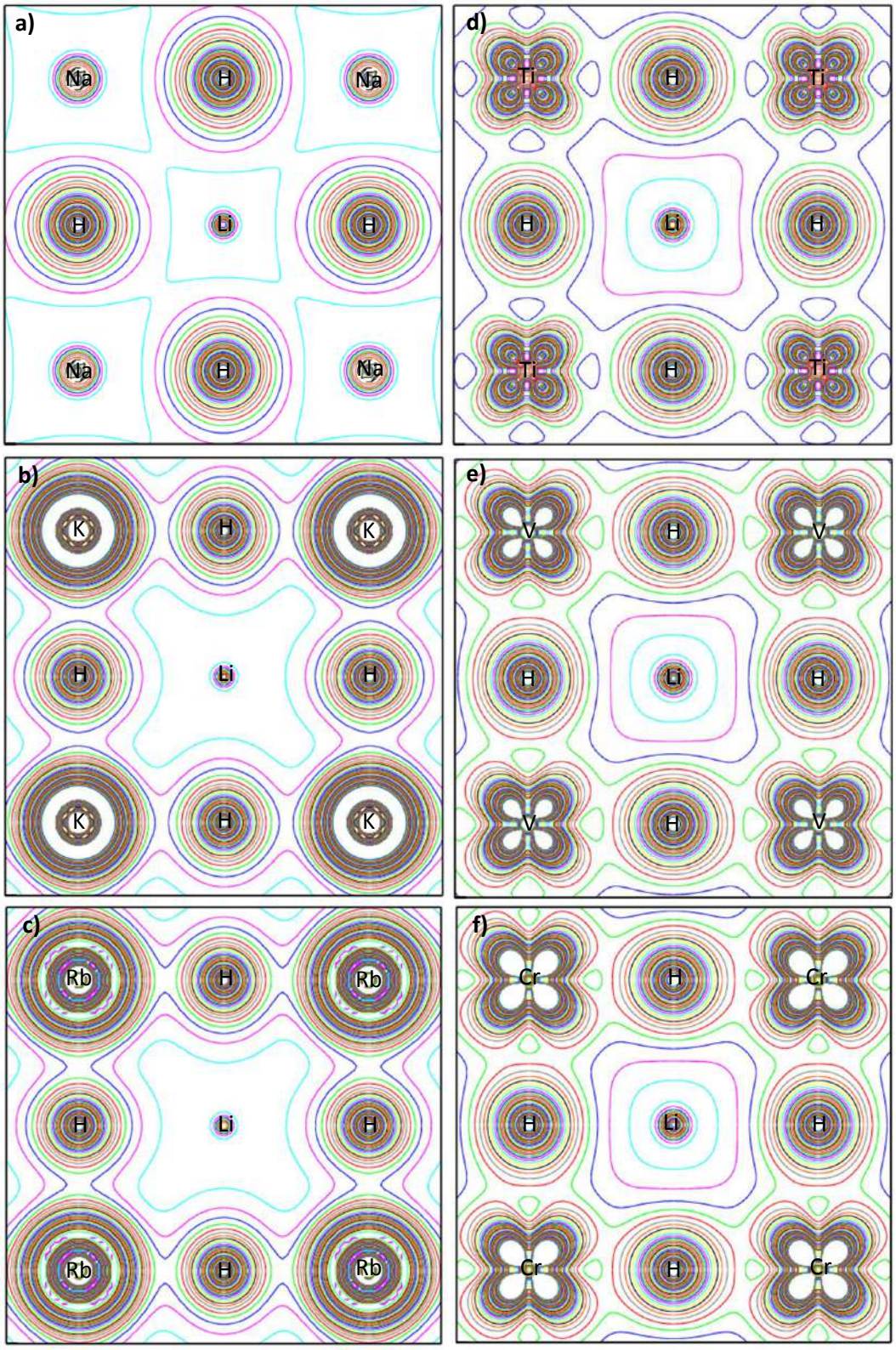


**Figure III.32:** Contour maps of the electron density distributions in the (100) atomic plane of the **a)** $Li_3NaH_4$, **b)** $Li_3KH_4$, **c)** $Li_3RbH_4$, **d)** $Li_3TiH_4$, **e)** $Li_3VH_4$ and **f)** $Li_3CrH_4$ for $\Delta\rho$=0.05.

### III.5.5 Conclusion

In order to compare $Li_3XH_4$ hydrides to $Li_7XH_8$ hydrides qualitatively and quantitatively in order to improve hydrogen storage properties, the effect of the alkali and transition metal atom substitutions in $Li_3XH_4$ hydrides (X(AM) = Na, K, Rb and X(TM) = Ti, V, Cr) on the structural and electronic properties was examined. This investigation was performed using the WIEN2k program, based on DFT and FP-LAPW methods.

The alkali metal atom substitutions in the $Li_3XH_4$ show a gradual increase in the value of lattice parameters from Na to Rb substitution. The lattice parameters in alkali metal atom substitutions in the $Li_3XH_4$ hydrides are higher than those of $Li_4H_4$ hydride. When the transition metal atoms in $Li_3XH_4$ go from Ti to Cr, the lattice parameters gradually degrade. The latter in both $Li_3VH_4$ and $Li_3CrH_4$ are lower than in $Li_4H_4$ hydride. The same behavior was observed in lattice parameters of the $Li_3XH_4$ hydrides as well as in those of the $Li_7XH_8$ hydrides.

There is a uniform decrease in formation energy values for each type of atom substitution from the $Li_3XH_4$ to $Li_7XH_8$ hydride. Of course, increasing the substituted atoms number in hydrides leads to an increasing effect on the remaining atoms. In addition, the type of substituted atom has an effect on formation energy values. Therefore, the number and the type of substituted atoms have an effect on the stability and, as a result, on the hydrogen storage performance. It is noted in the $Li_3XH_4$ a progressive decease in formation energy values for alkali metal atom substitutions from Na to Rb and for transition metal atom substitutions from Ti to Cr. The most instable hydride suitable for hydrogen storage applications compared to others is $Li_3CrH_4$ which has the lowest formation energy value (-11 kJ/mol $H_2$). The latter is less than that in the ideal formation energy range from -20 to -40 kJ/mol $H_2$ used in fuel cell applications [67-70]. The two substitution hydrides falling in this range are $Li_3RbH_4$ and $Li_3VH_4$ hydride.

The gravimetric storage of hydrogen decreases uniformly from $Li_7XH_8$ to $Li_3XH_4$ for the alkali and transition metal atom substitutions. Except for this uniform decrease, a similar behavior of the gravimetric storage of hydrogen in both $Li_7XH_8$ and $Li_3XH_4$ is observed for all metal atom substitutions. The reduction in gravimetric storage of hydrogen from $Li_7XH_8$ to $Li_3XH_4$ is not welcome in hydrogen storage applications.

$Li_3XH_4$ hydrides show the same electronic behavior as $Li_7XH_8$ hydrides, where $Li_4H_8$, $Li_3NaH_4$, $Li_3KH_4$ and $Li_3RbH_4$ have an insulating character while $Li_3TiH_4$, $Li_3VH_4$ and $Li_3CrH_4$ have a conducting character. Partial densities of states for both alkali and transition metal substitution hydrides $Li_3XH_4$ indicate, in the valence band, an increasing hybridization between X (AM) and 1s H orbitals from Na to Rb and from Ti to Cr substitution, respectively. The increase in

hybridization between X (AM or TM) and 1s H orbitals in $Li_3XH_4$ is relatively higher than that in $Li_7XH_8$. In addition, the density of p Li orbitals decreases, in the valence band, from Na to Rb and from Ti to Cr substitution in $Li_3XH_4$ hydrides, a fact explained by a gradual decrease in hybridization between p Li and 1 s H orbitals.

In the alkali and transition metal substituted hydrides, respectively, the electron density distributions in the region between X (= AM or TM) and H steadily rise from Na to Rb and from Ti to Cr substitution. The modification in charge distribution is proved by an increase of the covalent force bonding between X and Li and between X and H, resulting in a decrease of the ionic force bond between Li and H. It looks as though X atoms attract Li and H atoms in order to reduce the stress between Li and H atoms. The latter weakens when passing from Na to Rb and from Ti to Cr substitution in the alkali and transitions metal substituted hydrides, respectively. To first order, the charge distributions on the (100) atomic plane look similar in both $Li_3XH_4$ and $Li_7XH_8$ hydrides.

## III.6 References of the chapter III

[1] Napán R, Peltzer y Blancá EL. First-principles studies of lithium hydride series for hydrogen storage. Int J Hydrogen Energy 2012;37:5784-5789.

[2] Sirageldin I. Sustainable human development in the twenty-first century, Encyclopedia of life support systems. Eolss publisher Co. Ltd. Oxford; 2009.

[3] Rusman NAA, Dahari M. A review on the current progress of metal hydrides material for solid-state hydrogen storage applications. Int J Hydrogen Energy 2016;41:12108-12126.

[4] Ouyang LZ, Huang JM, Wang H, Wen YJ, Zhang QA, Sun DL, Zhu M. Excellent hydrolysis performances of $Mg_3RE$ hydrides. Int J Hydrogen Energy 2013;38:2973-2978.

[5] Thomas G. Overview of storage development DOE hydrogen program. Sandia National Laboratories. California; 2000.

[6] Lucas FC, Daniel RL, Leandro ILF, Tomaz TI. A scientometric review of research in hydrogen storage materials. Int J Hydrogen Energy 2020;45:5356-5366.

[7] Bocarsly A, Michael D, Mingos P. Fuel cells and hydrogen storage. Spinger Verlag Berlin Heidelberg; 2011, p. 177.

[8] Mykhaylo L, Ivan T, Yevgeniy K, Moegamat WD, Dana S, Vladimir L. Metal hydride hydrogen storage tank for fuel cell utility vehicles. Int J Hydrogen Energy 2020;45:7958-7967.

[9] Brutti S, Meggiolaro D, Paolone A, Reale P. Magnesium hydride as negative electrode active material in lithium cells: A review. Materials Today Energy 2017;3:53-59.

[10] Millet P. Hydrogen storage in hydride-forming materials. Advances in Hydrogen Production, Storage and Distribution 2014: 368-409.

[11] Lototskyy M, Yartys VA. Comparative analysis of the efficiencies of hydrogen storage systems utilising solid state H storage materials. J Alloy Comp 2015;645:365-373.

[12] Lototskyy MV, Tolj I, Pickering L, Sita C, Barbir F, Yartys V. The use of metal hydrides in fuel cell applications. Progress in Natural Science: Materials International 2017;27:3-20.

[13] Kisu K, Kim S, Oguchi H, Toyama N, Orimo SI. Interfacial stability between $LiBH_4$-based complex hydride solid electrolytes and Li metal anode for all-solid-state Li batteries. Journal of Power Sources 2019;436:226821.

[14] Bösenberg U. $LiBH_4$-$MgH_2$ composites for hydrogen storage. Hamburg/Germany: Technische Universität Hamburg-Harburg, Institute of Materials Physics and Technology, vol. PhD; 2009.

[15] Jepsen J, Milanese C, Girella A, Lozano GA, Pistidda C, Colbe JMBV, Marini A, Klassen T, Dornheim M. Compaction pressure influence on material properties and sorption behaviour of $LiBH_4$–$MgH_2$ composite. Int J Hydrogen Energy 2013;38:8357-8366.
[16] Messer CE. A Survey Report on Lithium Hydride. Office of Scientific and Technical Information. United States of America; 1960.
[17] Blaha P, Schwarz K, Sorantin P, Trickey SB. Full-potential, linearized augmented plane wave programs for crystalline systems. Comput Phys Commun 1990;59:399-415.
[18] Singh DJ. Plane waves, peudopotential and the LAPW method. Boston, Dortrecht, London: Kluwer Academic Publisher; 1994.
[19] Hohenberg P, Kohn W. Inhomogeneous electron gas. Phys Rev 1964;136:B864.
[20] Perdew JP, Burke K, Ernzerhof M. Generalized gradient approximation made simple. Phys Rev Lett 1996;77:3865.
[21] Blaha P, Schwarz K, Madsen GKH, Kvasnicka D, Luitz J. WIEN2k, an augmented plane wave and local orbital program for calculating crystal properties. Austria: Karlheinz Schwartz, Techn Universität Wien; 2001.
[22] Murnaghan FD. The Compressibility of Media under Extreme Pressures. Proc Natl Acad Sci USA 1944;30:244-7.
[23] Murnaghan FD. Finite Deformations of an Elastic Solid. Am J Math 1937;59(235-60).
[24] Herbst JF, Hector Jr LG. Energetics of the Li amide/Li amide hydrogen storage reaction. Phys Rev B 2005;72:125120.
[25] Fukai Y. The metal-hydrogen system, Springer Series in Material Science vol. 21. Berlin: Springer-Verlag; 1993.
[26] Bhihi M, ElKhatabi M, Lakhal M, Naji S, Labrim H, Benyoussef A, El Kenz A, Loulidi M. First principle study of hydrogen storage in doubly substituted Mg based hydrides. Int J Hydrogen Energy 2015;40:8356-8361.
[27] Miwa K, Ohba N, Towata S. First-principles study on lithium borohydride $LiBH_4$. Phys Rev B 2004;69:245120.
[28] Mohammedi L, Daoudi B, Boukraa A. Total and partial hydrogen restitution in TiFe-H Systems. Int J Hydrogen Energy 2015;40:2997-3000.
[29] Mohammedi L, Daoudi B, Boukraa A. *Ab-initio* structural and electronic properties of intermetallic compound $TiFeH_2$. Computational Condensed Matter 2015;2:11-15.
[30] Gunnarsson O, Johansson P. The spin-density-functional formalism for quantum mechanical calculations: test on diatomic molecules with an efficient numerical method. Int J Quantum Chem 1976;10:307.

[31] Nakamura H, Nguyen-Manh D, Pettifor G. Electronic structure and energetics of $LaNi_5$, a-$La_2Ni_{10}H$ and b-$La_2Ni_{10}H_{14}$. J Alloys Compd 1998;281:81-91.

[32] Shang CX, Bououdina M, Song Y, Guo ZX. Mechanical alloying and electronic simulations of ($MgH_2$ + M) systems (M = Al, Ti, Fe, Ni, Cu and Nb) for hydrogen storage. Int J Hydrogen Energy 2004;29:73-80.

[33] Son Y,Guo ZX,Yang R. Influence of selected alloying elements on the stability of magnesium dihydride for hydrogen storage applications: a first-principles investigation. Phys Rev B 2004;69:094205.

[34] Shelyapina MG, Fruchart D, Wolfers P. Electronic structure and stability of new FCC magnesium hydrides $Mg_7MH_{16}$ and $Mg_6MH_{16}$ (M: Ti, V, Nb): an ab initio study. Int J Hydrogen energy 2010;35:2025-2032.

[35] Kittel C. Introduction to solid state Physics. New York: Wiley; 1986.

[36] Abbas MA, Grant DM, Brunelli M, Hansen TC, Walker GS. Reducing the dehydrogenation temperature of lithium hydride through alloying with germanium. Phys Chem Chem Phys 2013;15:12139-12146.

[37] Hoang K, Van de Walle CG. LiH as a $Li^+$ and $H^-$ ion provider. Solid State Ionics. 2013;253:53-56.

[38] Kondo Y, Asaumi K. Effect of pressure on the direct energy gap of LiH. Journal of the Physical Society of Japan 1988;57:367-371.

[39] Calleja RD, Riande E. Electrical Properties of Polymers. Marcel Dekker, Inc, New York, USA; 2004, p. 575.

[40] Adit MT, Tanveer H, Rajeev A. Structural, electronic and thermodynamic properties of Aland Si-doped α-, γ-, and β-$MgH_2$: density functional and hybrid density functional calculations. Int J Hydrogen Energy 2012;37:9112-9122.

[41] Gremaud R, Broedersz CP, Borsa DM, Borgschulte A, Mauron P, Schreuders H, Rector JH, Dam B, Griessen R. Hydrogenography: An Optical Combinatorial Method To Find New Light-Weight Hydrogen-Storage Materials. Advanced Materials 2007;19:2813-2817.

[42] Satyapal S, Petrovic J, Read C, Thomas G, Ordaz G. The U.S.Department of energy's national hydrogen storage project:progress towards meeting hydrogen-powered vehicle requirements. Catal Today 2007;120:246-256.

[43] Kojima Y. Hydrogen storage materials for hydrogen and energy carriers. Int J Hydrogen Energy 2019;44:18179-19192.

# General conclusion

This work was carried out using the WIEN2k program, based on the DFT and FP-LAPW methods. The results are summarized as follows:

- Structural, electronic and stability properties of saline $LiH_n$ hydrides (n=1, 2, 4) have been studied. The lattice parameters of LiH_225 are close to the theoretical and experimental ones. In cubic lattice hydrides, the LiH_221 hydride has smaller lattice parameters than LiH_225, $LiH_4$_215 and $LiH_4$_221 hydrides. In hexagonal lattice hydrides, lattice parameters are smaller in the $LiH_2$_191 hydride than in the $LiH_2$_194 hydride. Results display a higher relative volumetric reduction of -62.96% in going from Li_229 metal to LiH_221 hydride. $LiH_2$_191, $LiH_4$_215 and $LiH_4$_221 hydrides exhibit a similar volumetric reduction of -55.49, -35.06 and -19.16 %, respectively. A volumetric augmentation of 50.88 % has been observed in going from Li_229 metal to LiH_225 hydride and of 74.54% in going from Li_229 metal to $LiH_2$_194 hydride. Generally, all of these saline hydrides have very good gravimetric storage densities of hydrogen compared to Mg based hydrides which are considered as acceptable hydrogen storage materials with a hydrogen gravimetry equal to ~7% (wt.). We find a semi-conductor character for LiH_221, an insulator character for LiH_225 and a metallic character for Li, $LiH_2$_191, $LiH_2$_194, $LiH_4$_221 and $LiH_4$_215. In the valence band, both 2p Li and 2s H orbitals present the same behavior in energy and geometry, indicating a high hybridization for saline hydrides $LiH_n$ (n=1, 2, 4). The most stable hydride which has the strongest bonding energy is the $LiH_4$_221. The less stable hydride is LiH_221 which has the lowest cohesive energy. The latter hydride could probably be used for hydrogen storage.
- The effect of the hydrostatic pressure on the LiH hydride (crystallized in 225 space group) was studied to determine the convenient pressure that could be utilized in hydrogen storage systems. The equilibrium point corresponds to a hydrostatic pressure of $P_{eq} = -1.356$ GPa, a unit cell volume of $V_{eq} = 108.2975\ (Bohr)^3$, a total energy of $E_{eq} = -16.271670$ Ry and a lattice parameter of $a = 4.004$ Å. Compression and expansion states are relatively dependent on the equilibrium point. The value and direction of a hydrostatic pressure is directly associated with its distance from the equilibrium point. With the exception of the equilibrium point, which has the highest total energy value, the total energy decreases gradually with increasing hydrostatic pressure. The equilibrium point (N° 7), corresponding to $P_{eq} = -1.356$ GPa, shows the highest stability compared to other pressure values. The

point N° 3, corresponding to P=5.972 GPa, exhibits the lowest stability compared to others pressure values. Therefore, at the equilibrium state, hydrogen reversibility and storage are more difficult. The best point for hydrogen storage applications among these points is point N° 3. In addition, the latter has the smallest lattice parameters, which is satisfactory for hydrogen storage systems. DOS analysis shows that, in the valence band, various pressures influence the shape of 1s H orbitals more than that of 2p Li orbitals. Densities of states at the two peaks of 1s H orbitals corresponding to point N° 3 are lower than others. Therefore, in this point, there is a weak hybridization between 2p Li and 1s H orbitals, indicating lower stability and higher hydrogen kinetic reversibility.

- In order to increase the performance of hydrogen storage, the impact of alkali and transition metal atom replacements in Li-based hydrides ($Li_7XH_8$ with X(AM) = Na, K, Rb and X(TM) = Ti, V, Cr) on the structural and electronic properties was examined. The LiH hydride's computed structural parameters were determined to be within the limitations of previously calculated theoretical and experimental values. Whereas the transition metal atom substitutions in the $Li_7XH_8$ have steadily reduced the lattice parameters compared to the $Li_8H_8$ hydride, the alkali metal atom substitutions have raised the lattice parameters in comparison to the $Li_8H_8$ hydride. According to the computed formation energy estimates, the $Li_7XH_8$ hydride's stability gradually degrades as a result of the transition metal substitution from Ti to Cr and the alkali substitution from Na to Rb. $Li_7CrH_8$ has been shown to be the least stable phase among all alkali and transition metal atom substitutions. The lattice parameters of the $Li_7CrH_8$ hydride are also less than those of the others. The gravimetric hydrogen storage density in the transition metal substituted hydrides falls from Ti to Cr substitution at a comparatively slow rate. While having a similar relative fall in formation energy, the transition metal substituted hydrides exhibit a smaller relative decline in the gravimetric hydrogen storage density than the alkali metal substituted ones. Analyses of the electron density and density of states lend support to the interpretation of our findings. The three transition metal substitutions caused the insulating $Li_8H_8$ hydride to change into conducting hydrides.
- The influence of the alkali and transition metal atom substitutions in $Li_3XH_4$ hydrides (X(AM) = Na, K, Rb and X(TM) = Ti, V, Cr) on the structural and electronic properties was also examined in order to compare them, qualitatively and quantitatively, with $Li_7XH_8$ hydrides with the aim of improving hydrogen storage properties. The alkali metal atom substitutions in the $Li_3XH_4$ show a gradual increase in the value of lattice parameters from Na to Rb substitution. The lattice parameters in alkali metal atom substitutions in the $Li_3XH_4$

hydrides are higher than of those of $Li_4H_4$ hydride. The transition metal atom substitutions in the $Li_3XH_4$ from Ti to Cr show a gradual decrease in lattice parameters. The latter in both $Li_3VH_4$ and $Li_3CrH_4$ are lower than in $Li_4H_4$ hydride. The same behavior observed in lattice parameters of the $Li_3XH_4$ hydrides as well as in those of the $Li_7XH_8$ hydrides. There is a uniform decrease in formation energy values for each type of atom substitution from the $Li_7XH_8$ to $Li_3XH_4$ hydride. Of course, increasing the substituted atoms number in hydrides leads to an increasing effect on the remaining atoms. In addition, the type of substituted atom has an effect on formation energy values. Therefore, the number and the type of substituted atoms have an effect on the stability and, as a result, on the hydrogen storage performance. It is noted in the $Li_3XH_4$ a progressive decease in formation energy values for alkali metal atom substitutions from Na to Rb and for transition metal atom substitutions from Ti to Cr. The less stable hydride suitable for hydrogen storage applications compared to others is $Li_3CrH_4$ which has the lowest formation energy value (-11 kJ/mol $H_2$). The latter is less than that in the ideal formation energy range from -20 to -40 kJ/mol $H_2$ used in fuel cell applications [67-70]. The two substitution hydrides falling in this range are $Li_3RbH_4$ and $Li_3VH_4$ hydride. The gravimetric storage of hydrogen decreases uniformly from $Li_7XH_8$ to $Li_3XH_4$ for the alkali and transition metal atom substitutions. Except for this uniform decrease, a similar behavior of the gravimetric storage of hydrogen in both $Li_7XH_8$ and $Li_3XH_4$ is observed for all metal atom substitutions. The reduction in gravimetric storage of hydrogen from $Li_7XH_8$ to $Li_3XH_4$ is not welcome in hydrogen storage applications. $Li_3XH_4$ hydrides show the same electronic behavior as $Li_7XH_8$ hydrides, where $Li_4H_8$, $Li_3NaH_4$, $Li_3KH_4$ and $Li_3RbH_4$ have an insulating character while $Li_3TiH_4$, $Li_3VH_4$ and $Li_3CrH_4$ have a conducting character. Partial densities of states for both alkali and transition metal substitution hydrides $Li_3XH_4$ indicate, in the valence band, an increasing hybridization between X (AM) and 1s H orbitals from Na to Rb and from Ti to Cr substitution, respectively. The increase in hybridization between X (AM or TM) and 1s H orbitals in $Li_3XH_4$ is relatively higher than that in $Li_7XH_8$. In addition, the density of p Li orbitals decreases, in the valence band, from Na to Rb and from Ti to Cr substitution in $Li_3XH_4$ hydrides, a fact explained by a gradual decrease in hybridization between p Li and 1 s H orbitals. The electron density distributions in the region between X (= AM or TM) and H increase gradually from Na to Rb and from Ti to Cr substitution in the alkali and transition metal substituted hydrides, respectively. The modification in charge distribution is proved by an increase of the covalent force bonding between X and Li and between X and H, resulting in a decrease of the ionic force bond between Li and H. It looks as though X atoms attract Li and H atoms in order to reduce the stress between Li and H

atoms. The latter weakens when passing from Na to Rb and from Ti to Cr substitution in the alkali and transitions metal substituted hydrides, respectively. To first order, the charge distributions on the (100) atomic plane look similar in both $Li_3XH_4$ and $Li_7XH_8$ hydrides.

First-principles calculations are a great technique to identify new hydrogen storage compounds or to gather knowledge about metal hydrides that is challenging to acquire experimentally.

This work is open a way to others researchers in the Laboratory of Development of New and Renewable Energies in Arid and Saharian Zones to work on the other type of substitutions and on other different hydrides.

# Appendix A

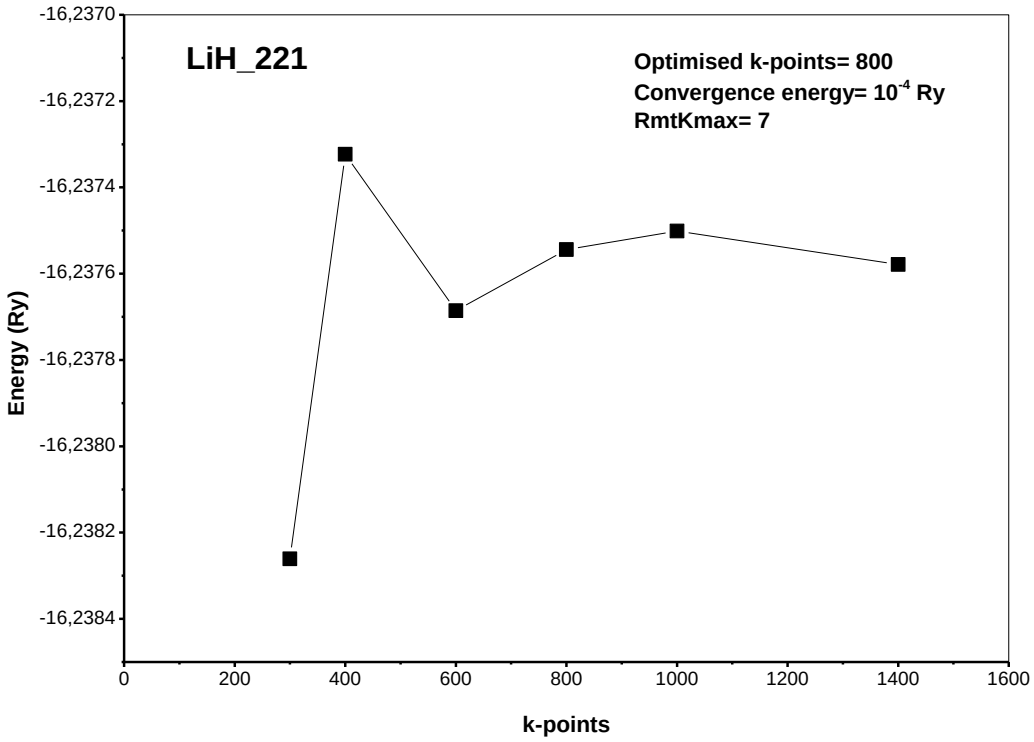


**Figure A.A1:** Total energy of LiH_221 versus k-points.

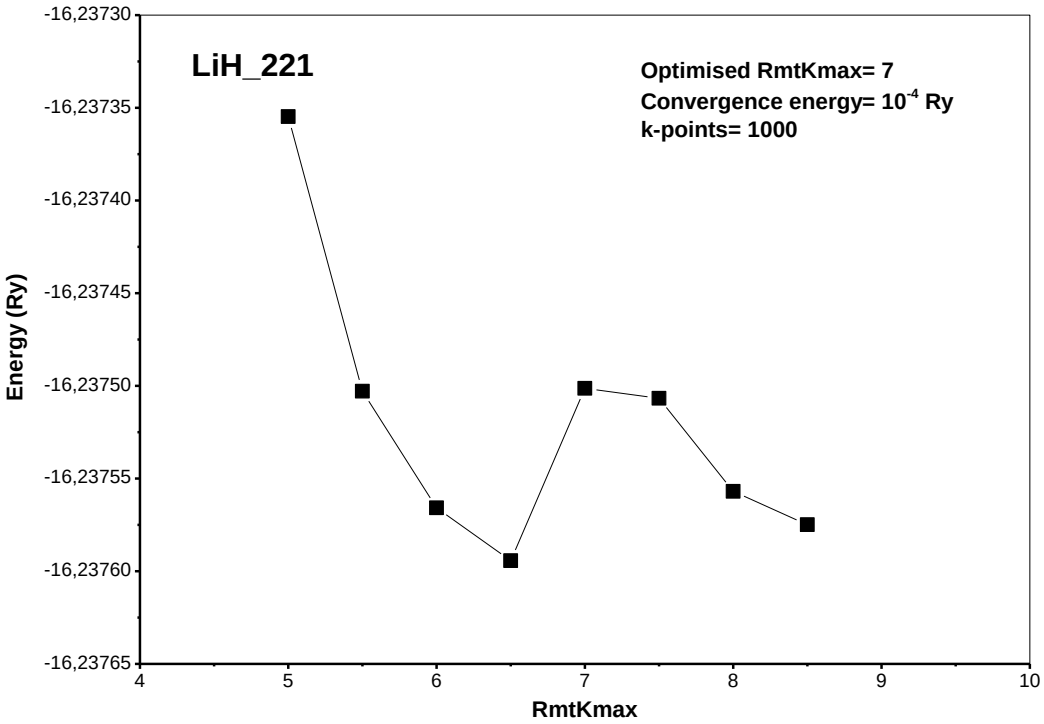


**Figure A.A2:** Total energy of LiH_221 versus RmtKmax.

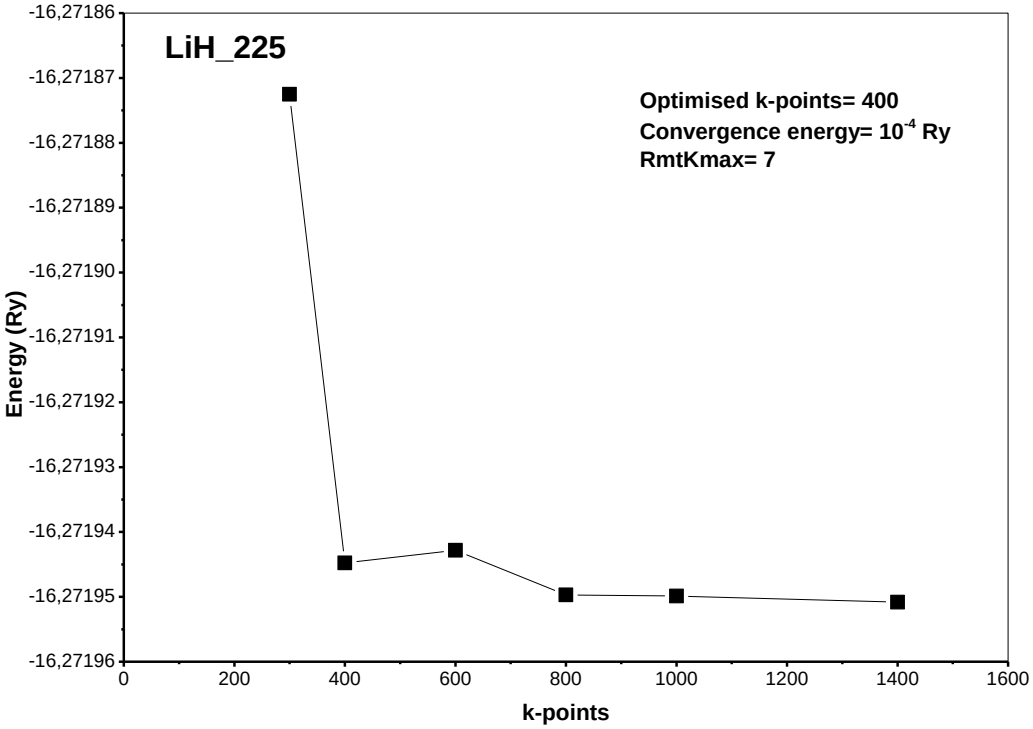


**Figure A.A3:** Total energy of LiH_225 versus k-points.

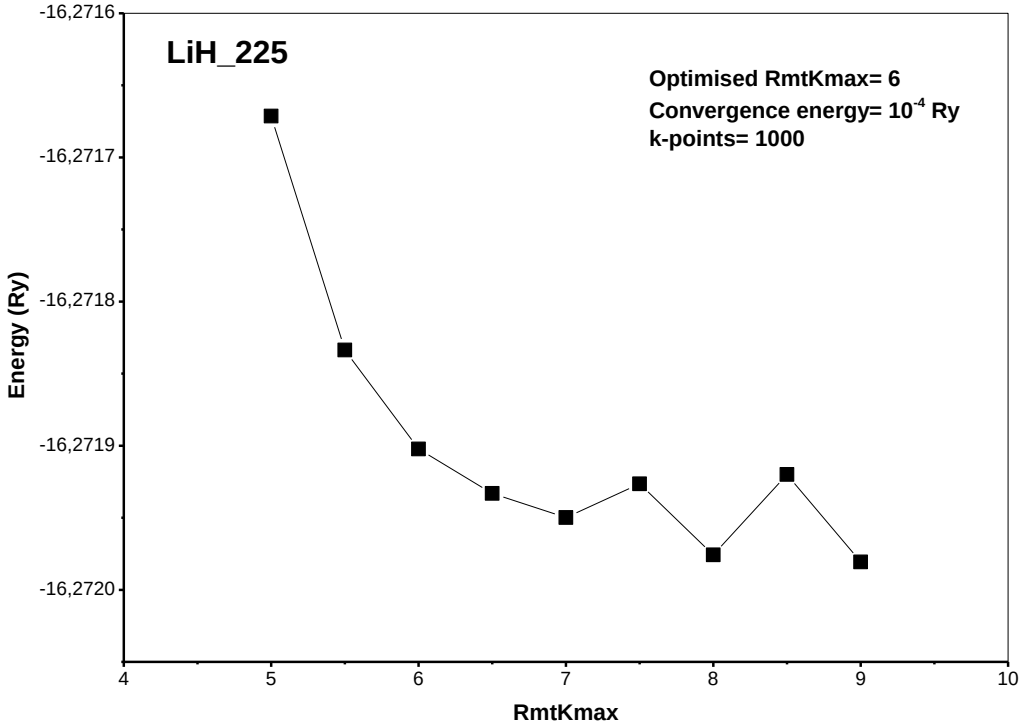


**Figure A.A4:** Total energy of LiH_225 versus RmtKmax.

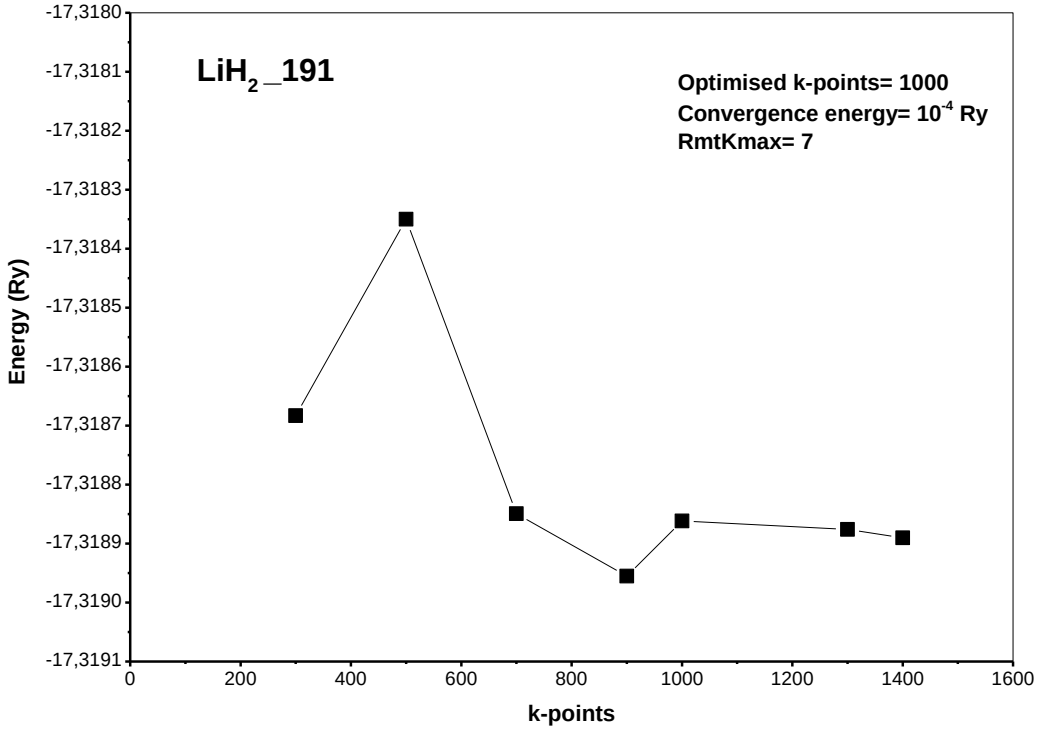


**Figure A.A5:** Total energy of $LiH_2$_191 versus k-points.

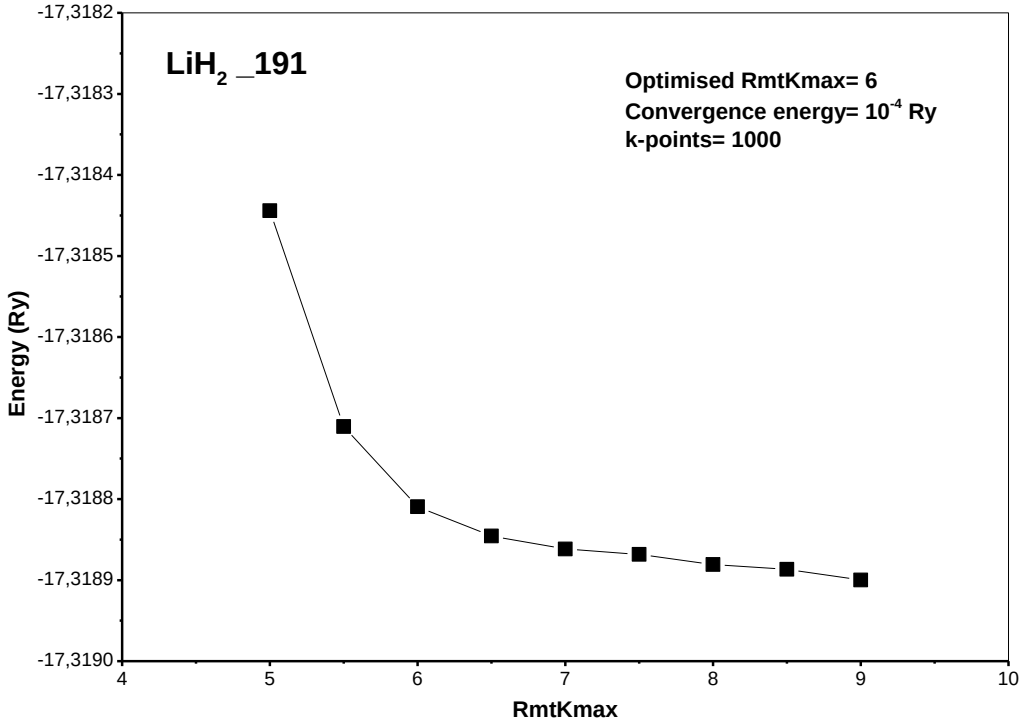


**Figure A.A6:** Total energy of $LiH_2$_191 versus RmtKmax.

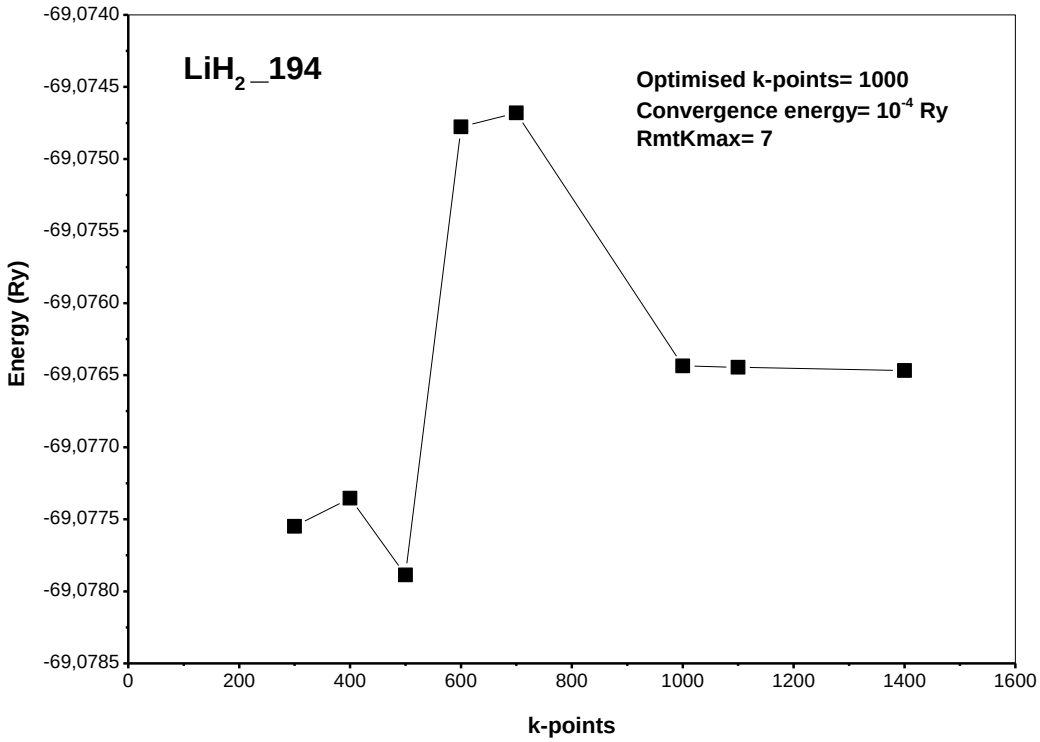


**Figure A.A7:** Total energy of $LiH_2$_194 versus k-points.

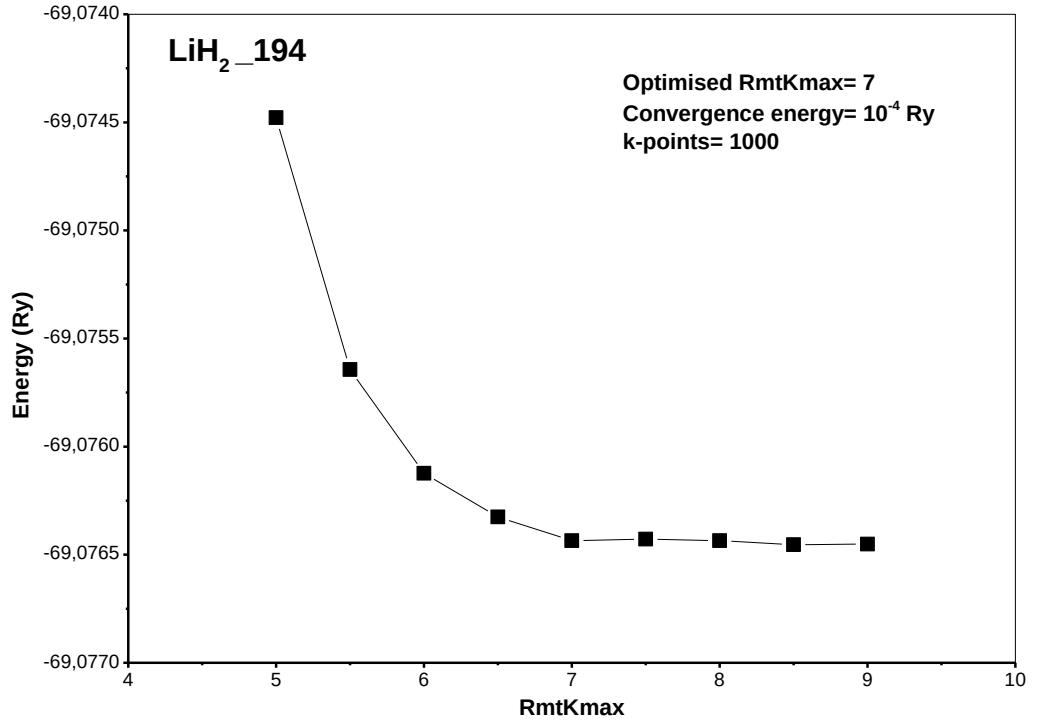


**Figure A.A8:** Total energy of $LiH_2$_194 versus RmtKmax.

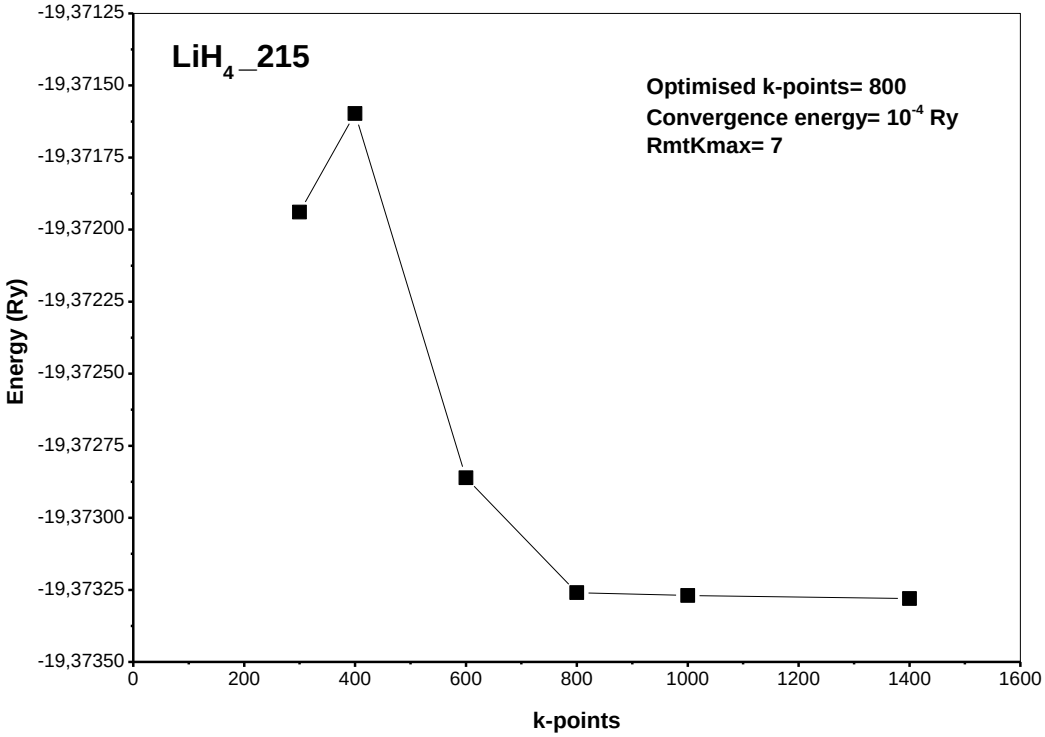


**Figure A.A9:** Total energy of $LiH_4$_215 versus k-points.

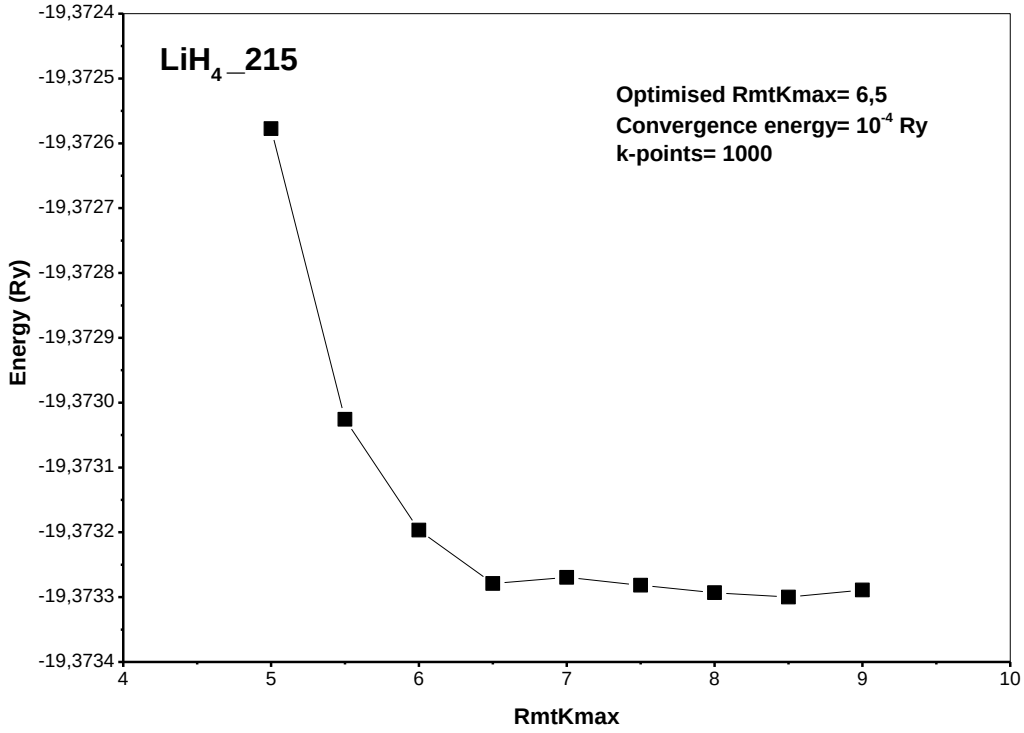


**Figure A.A10:** Total energy of $LiH_4$_215 versus RmtKmax.

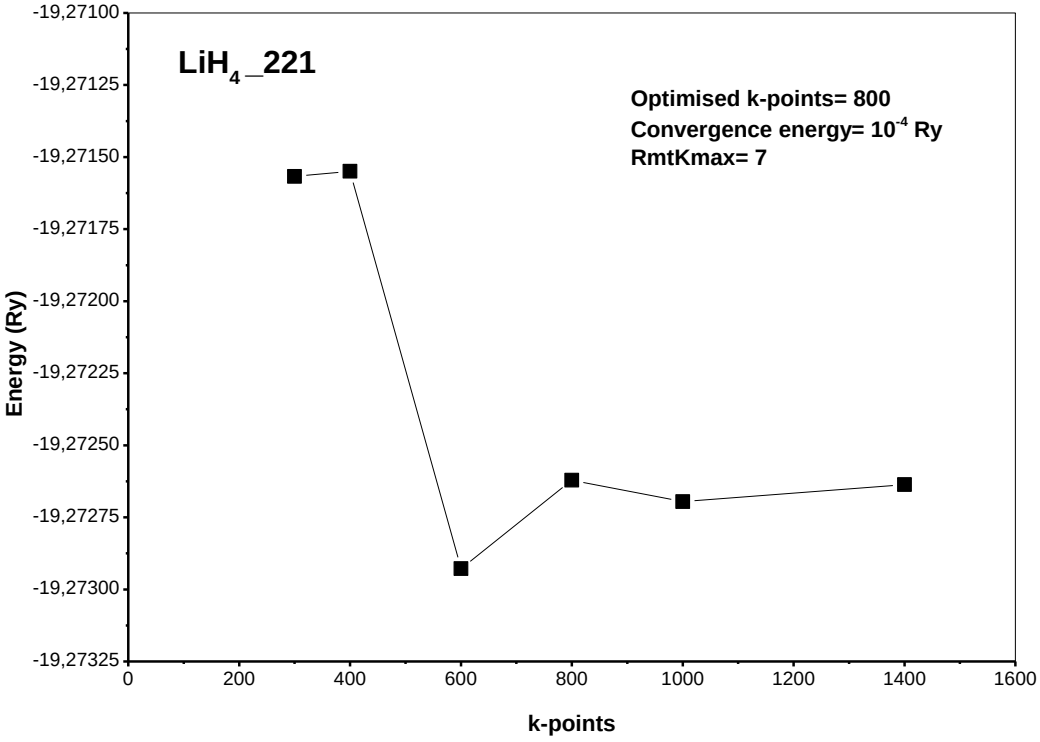


**Figure A.A11:** Total energy of $LiH_4$_221 versus k-points.

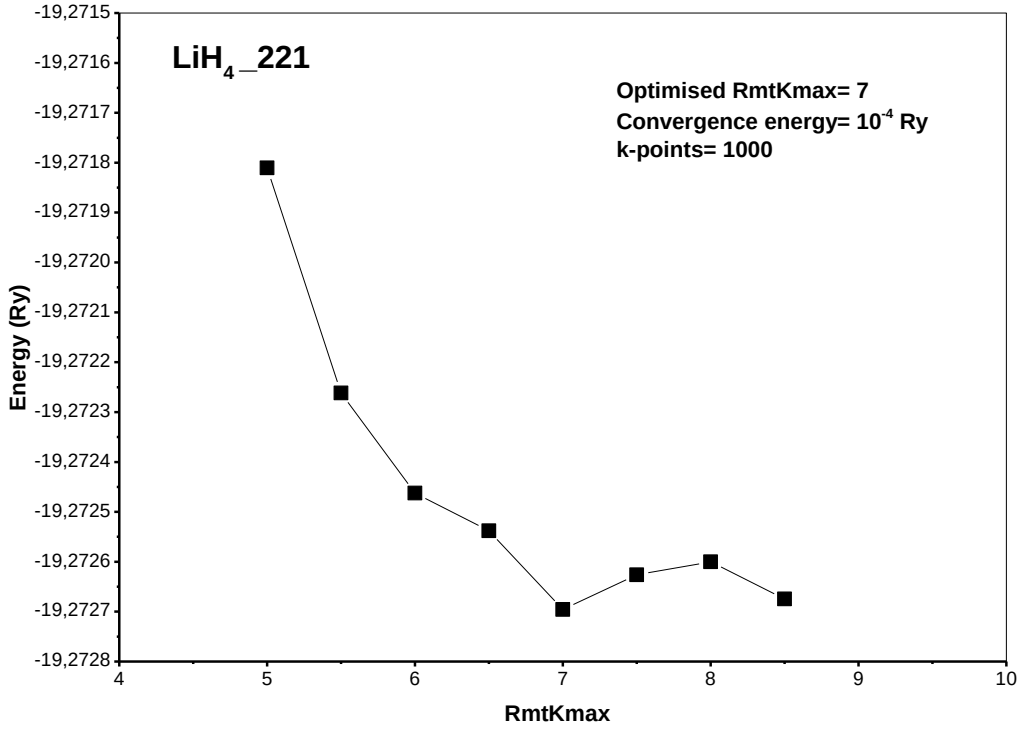


**Figure A.A12:** Total energy of $LiH_4$_221 versus RmtKmax.

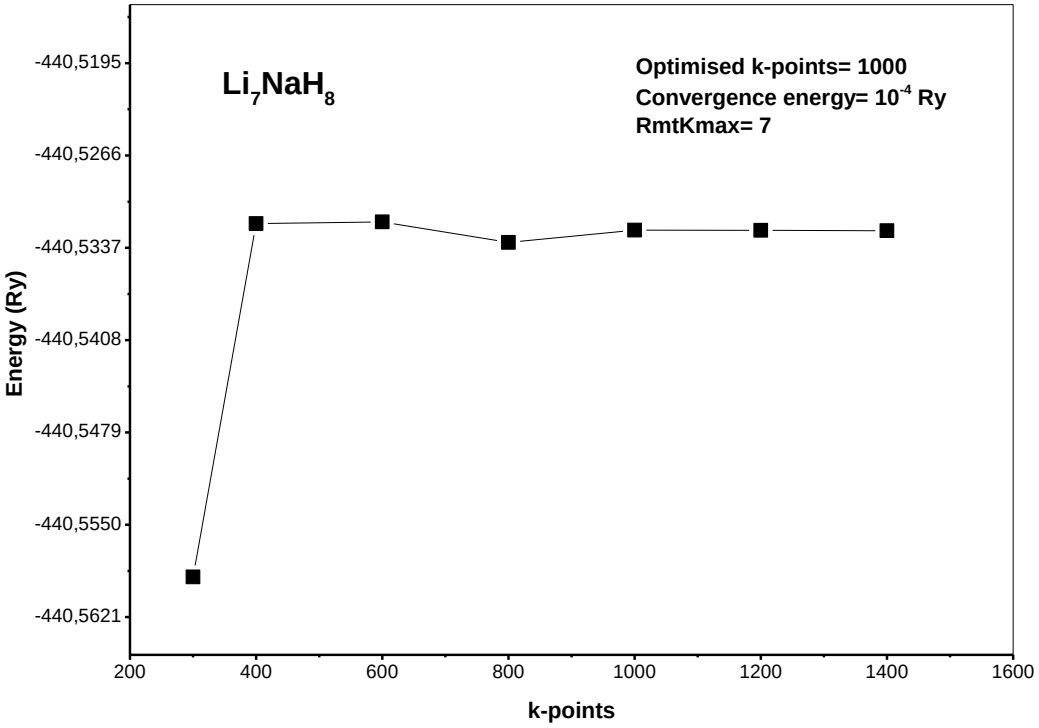


**Figure A.A13:** Total energy of $Li7NaH_8$ versus k-points.

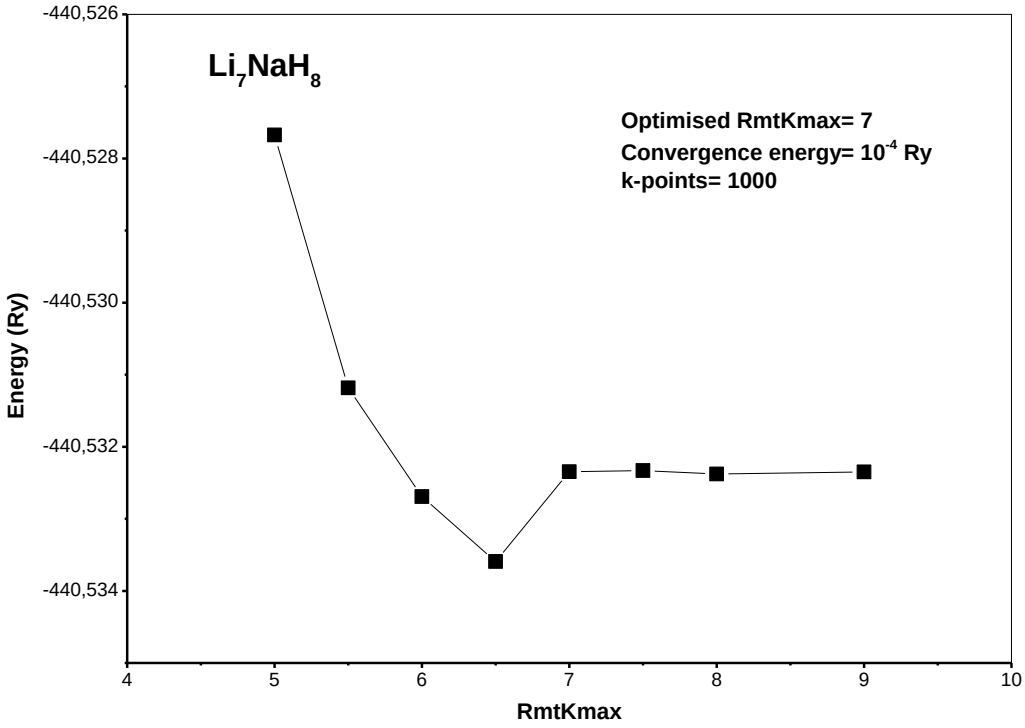


**Figure A.A14:** Total energy of $Li_7NaH_8$ versus RmtKmax.

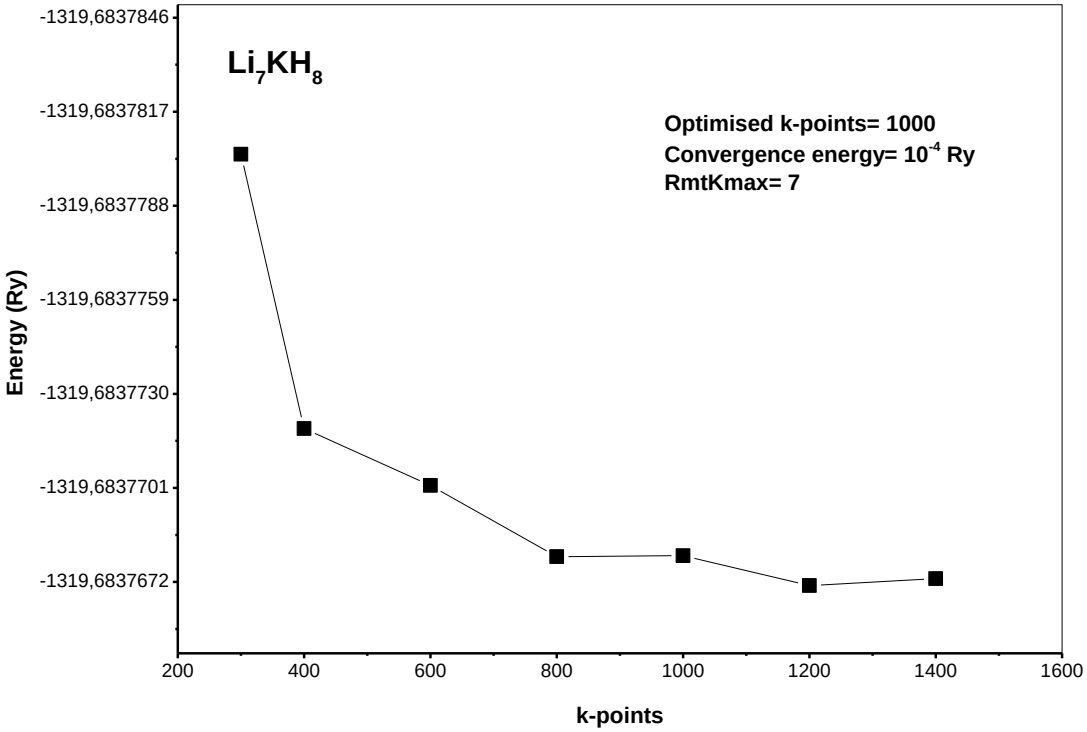


**Figure A.A15:** Total energy of $Li_7KH_8$ versus k-points.

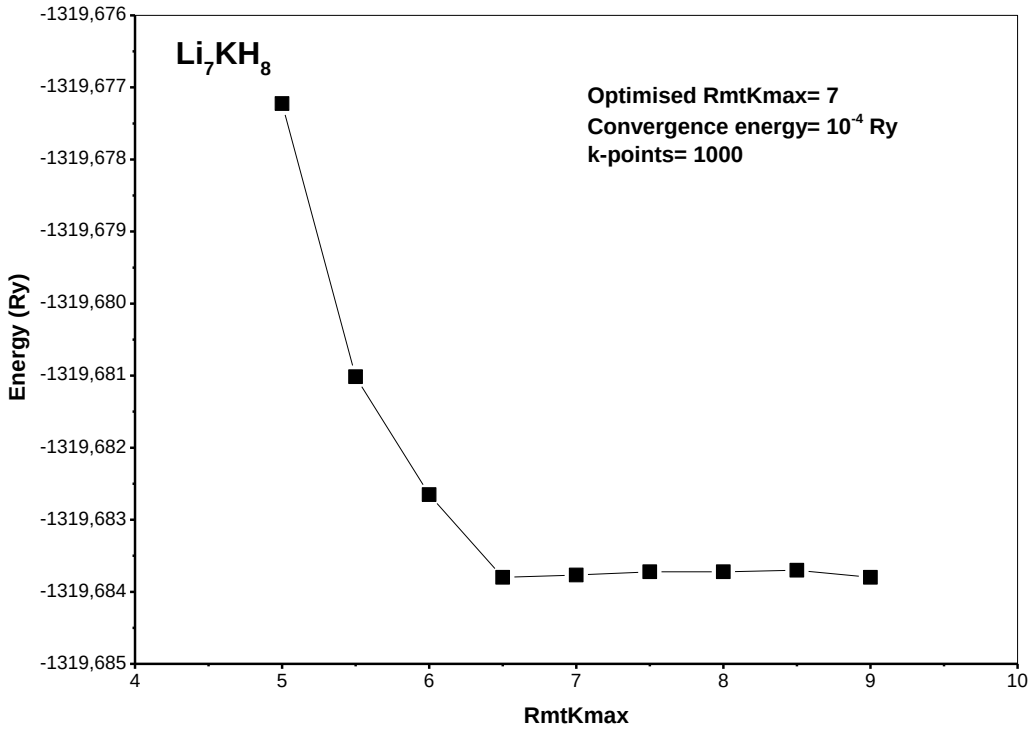


**Figure A.A16:** Total energy of $Li_7KH_8$ versus RmtKmax.

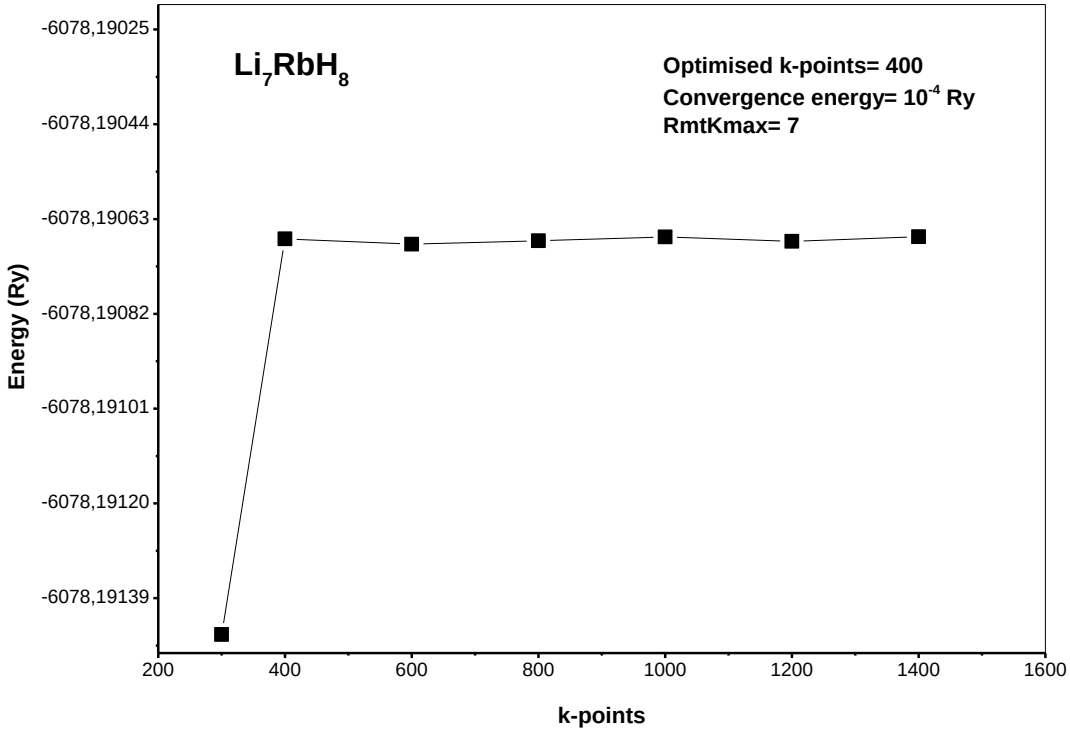


**Figure A.A17:** Total energy of $Li_7RbH_8$ versus k-points.

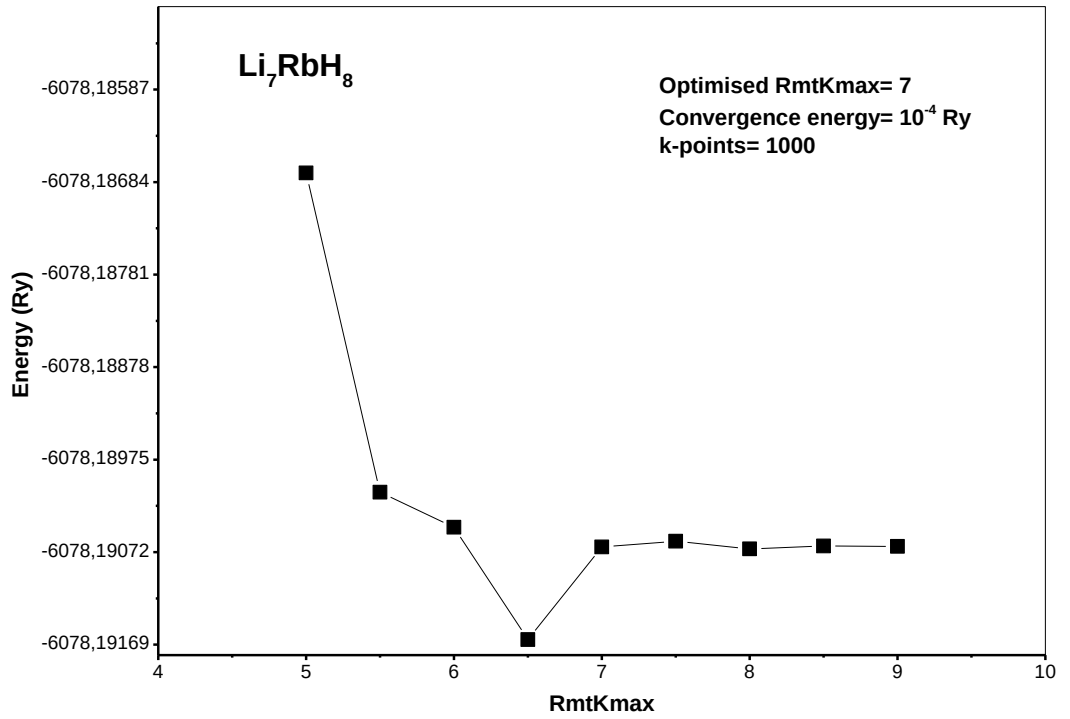


**Figure A.A18:** Total energy of $Li_7RbH_8$ versus RmtKmax.

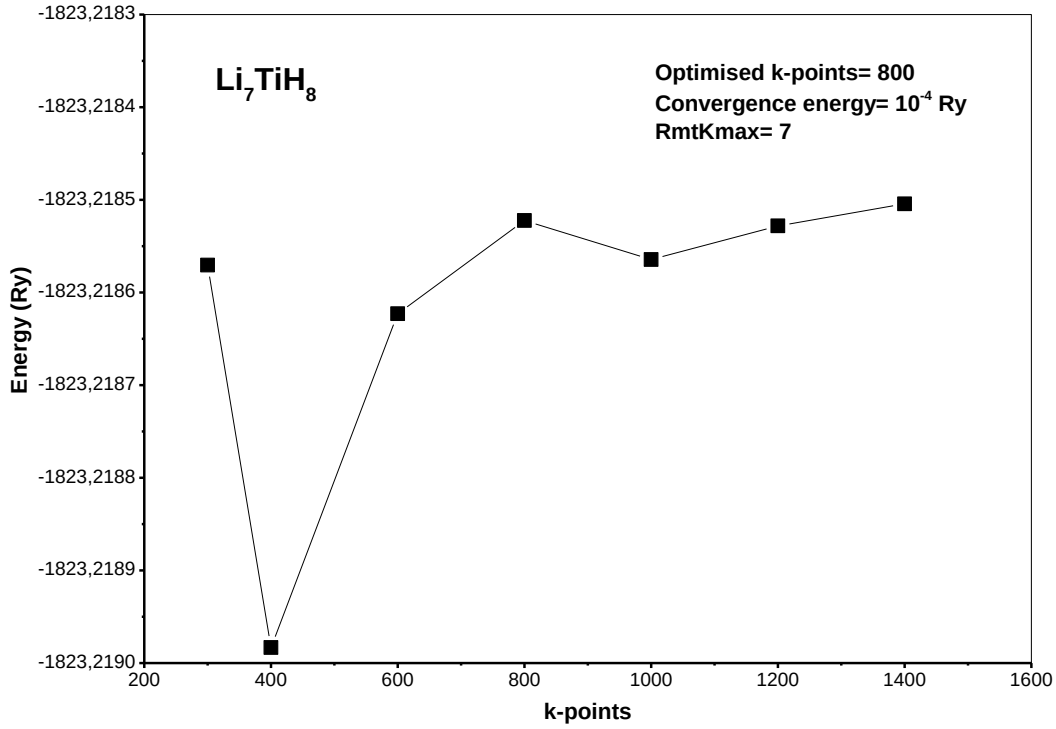


**Figure A.A19:** Total energy of $Li_7TiH_8$ versus k-points.

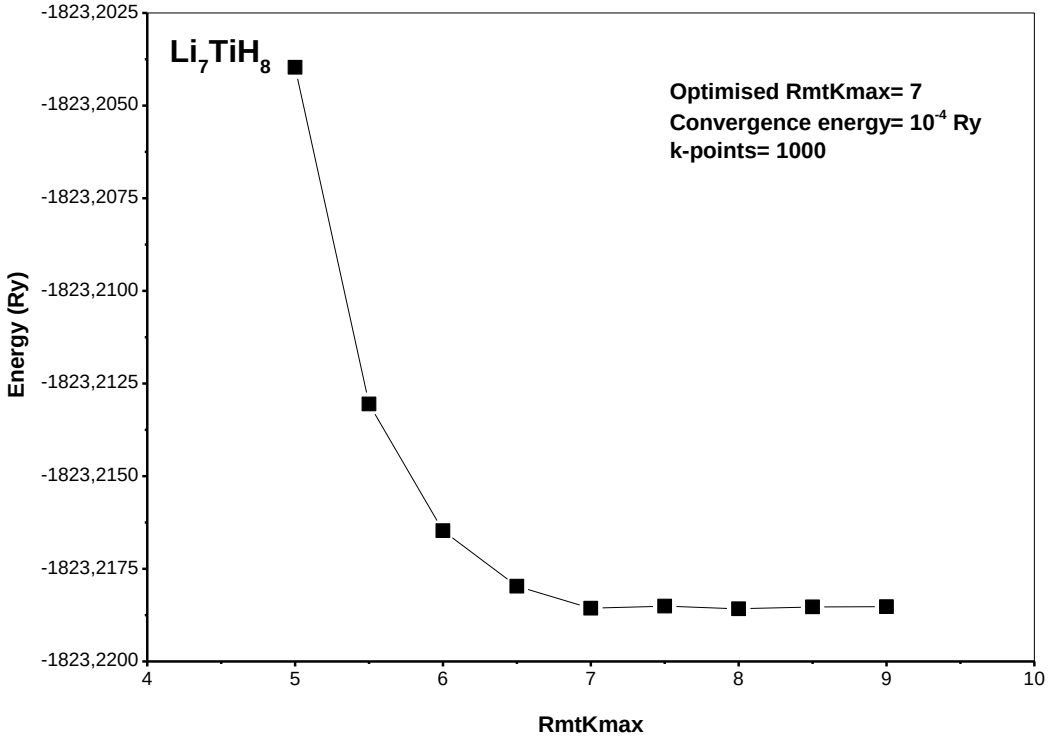


**Figure A.A20:** Total energy of $Li_7TiH_8$ versus RmtKmax.

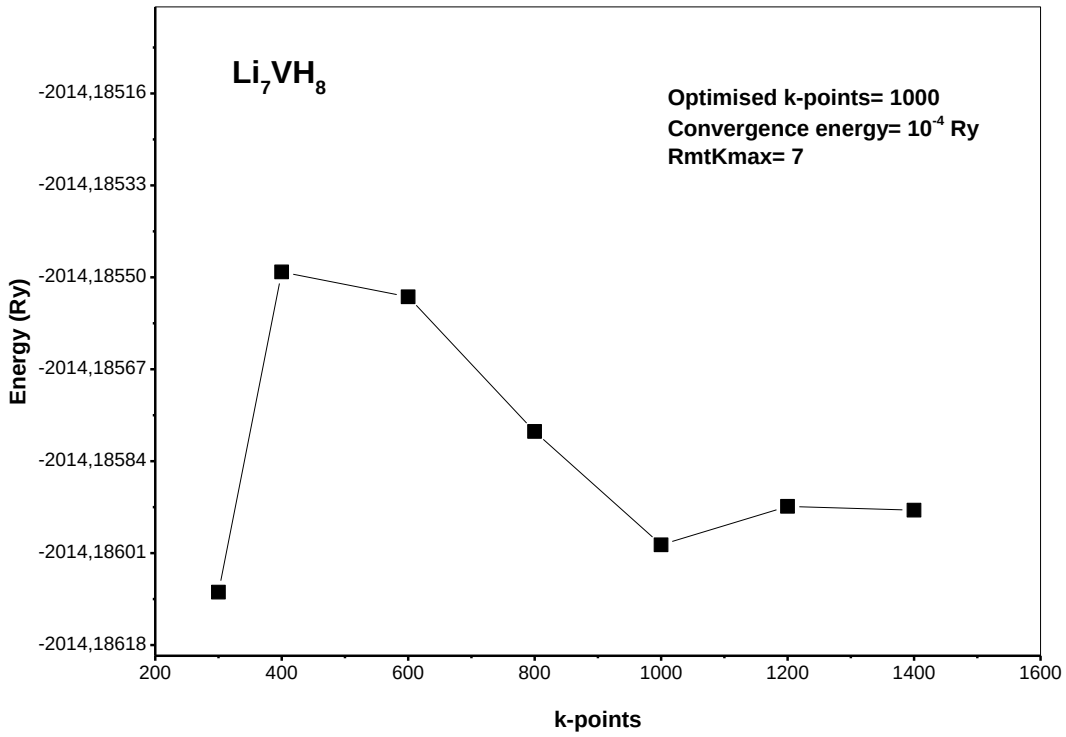


**Figure A.A21:** Total energy of $Li_7VH_8$ versus k-points.

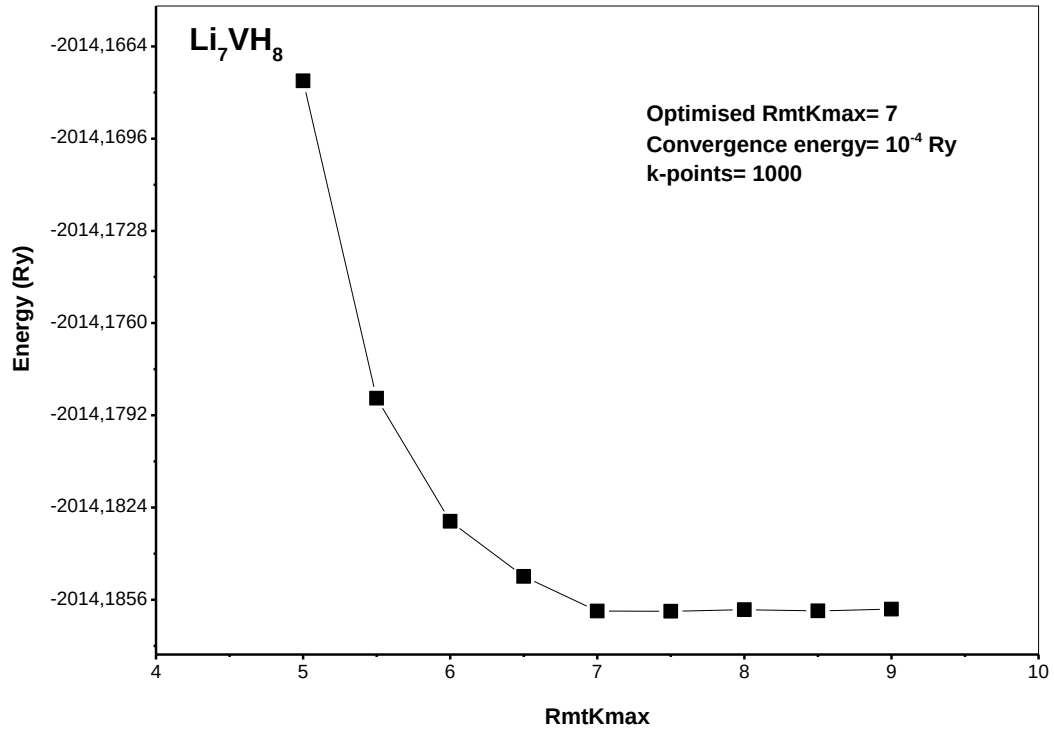


**Figure A.A22:** Total energy of $Li_7VH_8$ versus RmtKmax.

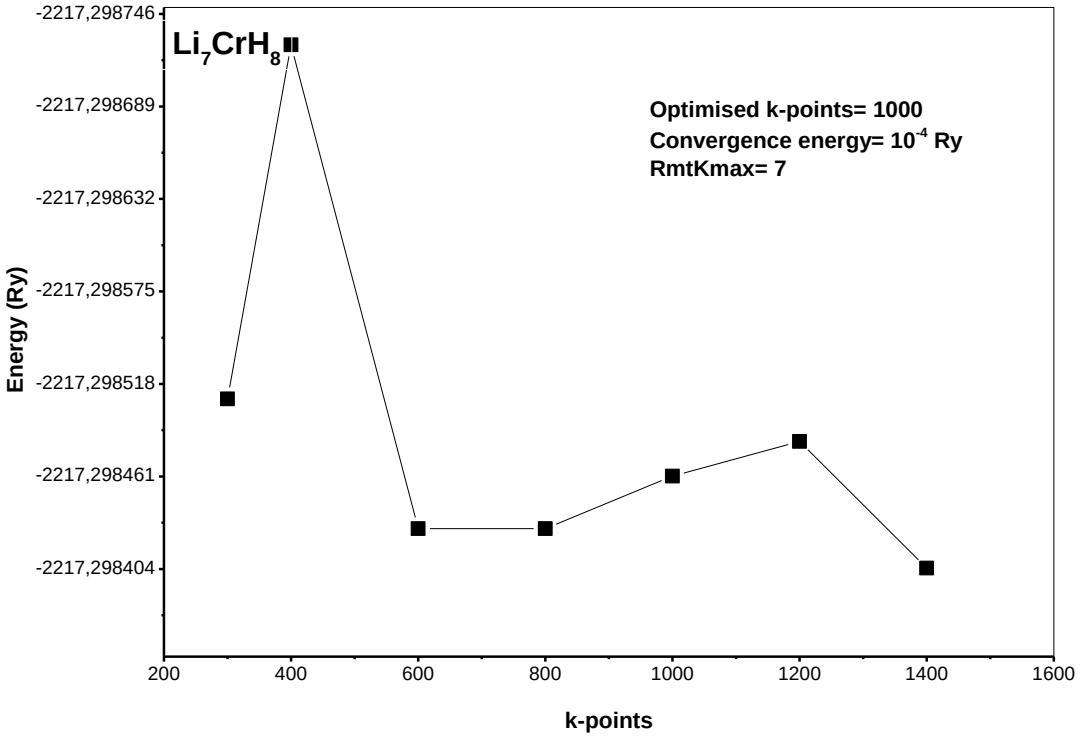


**Figure A.A23:** Total energy of $Li_7CrH_8$ versus k-points.

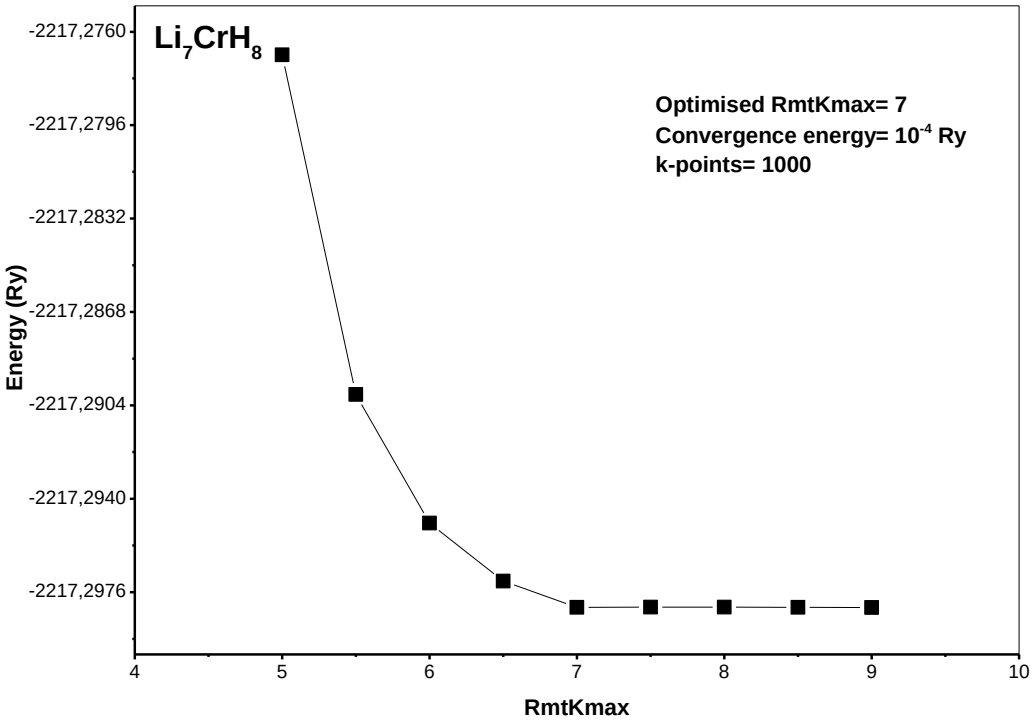


**Figure A.A24:** Total energy of $Li_7CrH_8$ versus RmtKmax.

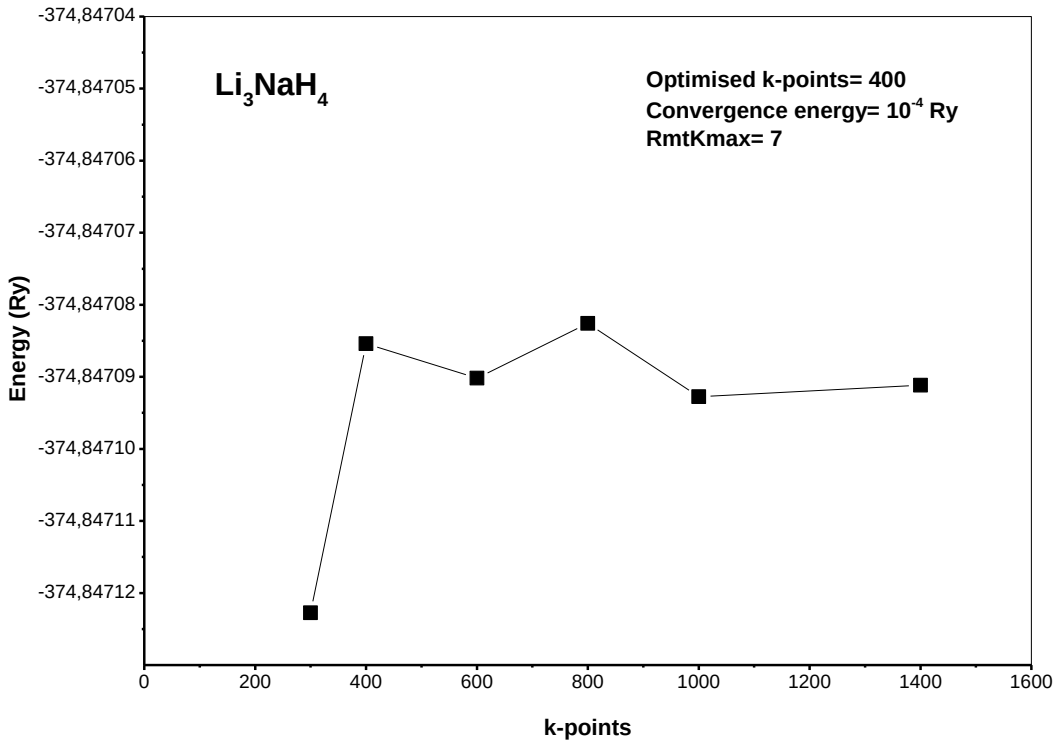


**Figure A.A25:** Total energy of $Li_3NaH_4$ versus k-points.

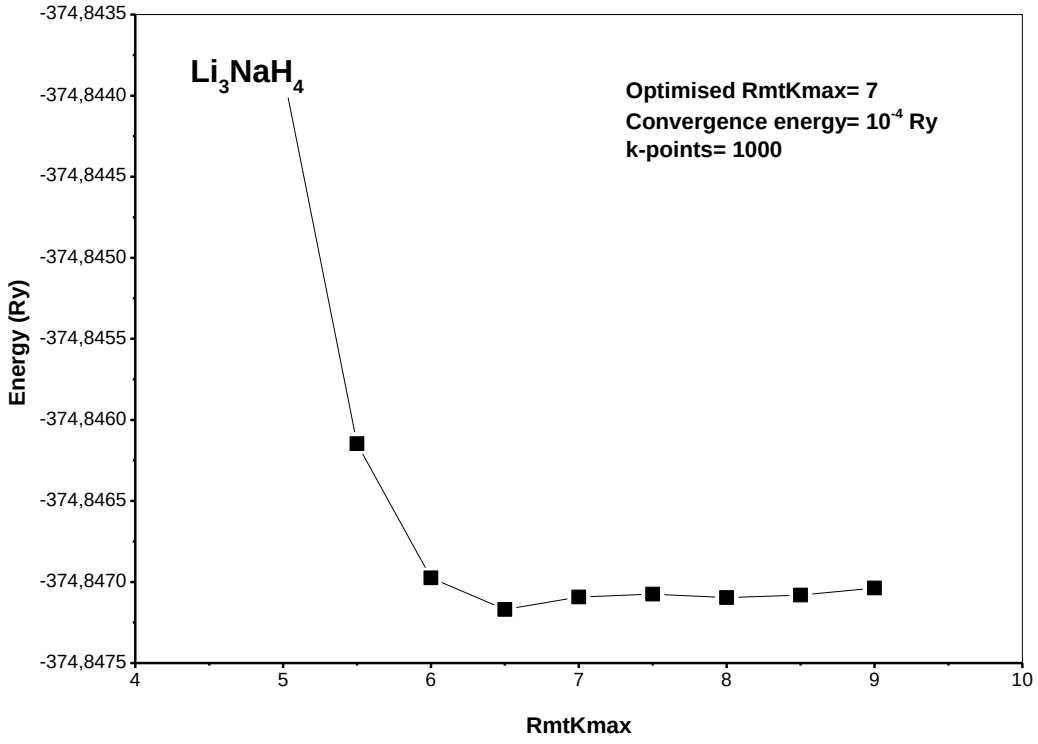


**Figure A.A26:** Total energy of $Li_3NaH_4$ versus RmtKmax.

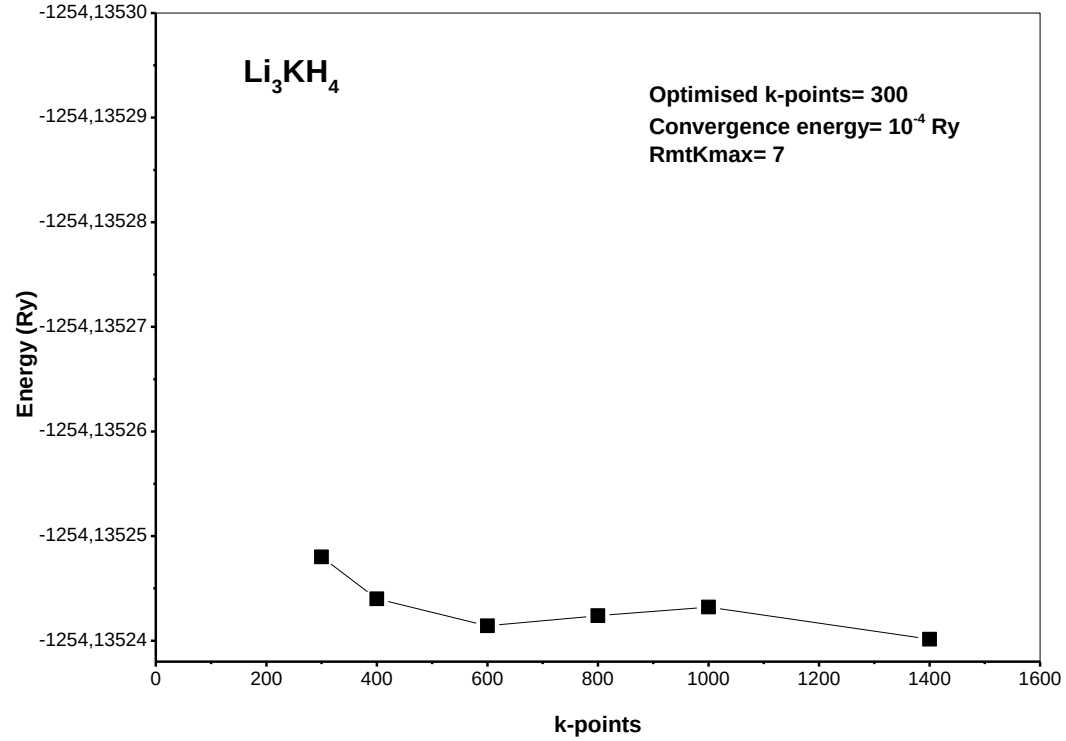


**Figure A.A27:** Total energy of $Li_3KH_4$ versus k-points.

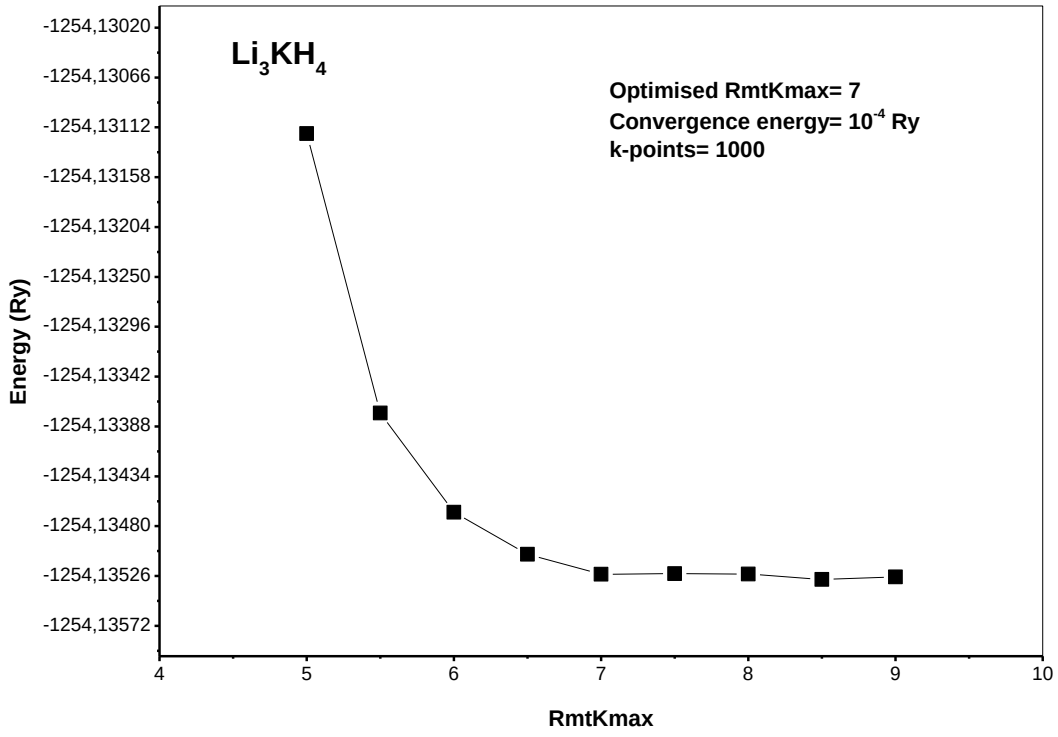


**Figure A.A28:** Total energy of $Li_3KH_4$ versus RmtKmax.

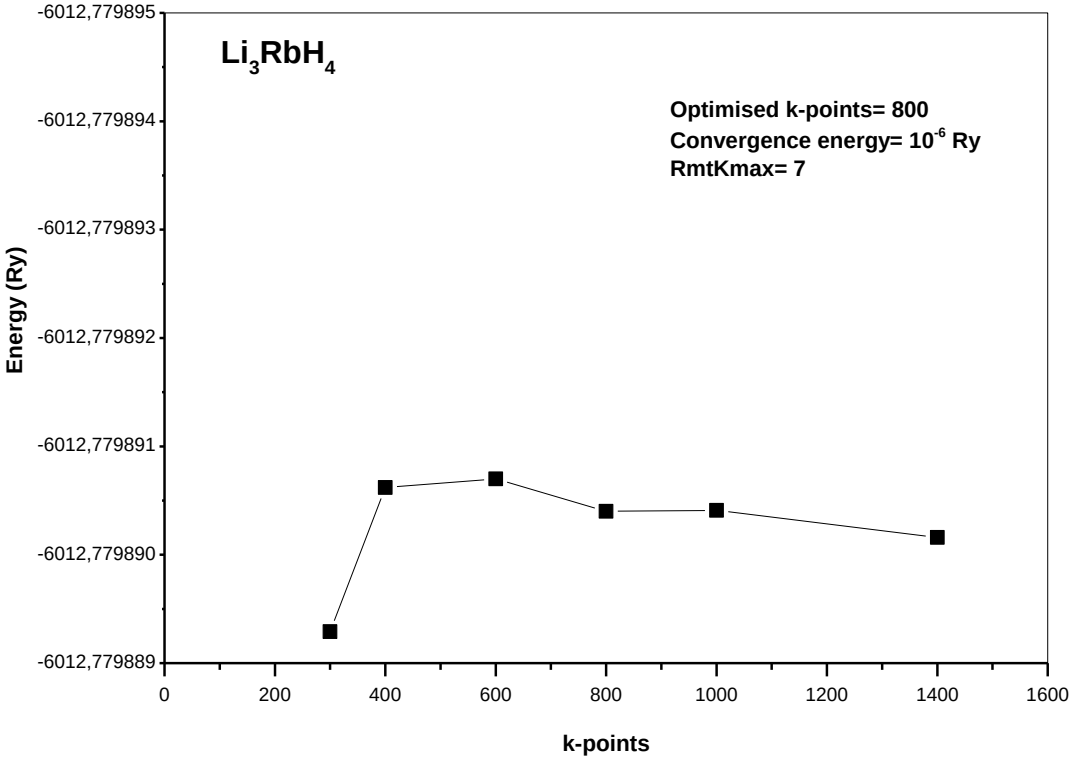


**Figure A.A29:** Total energy of $Li_3RbH_4$ versus k-points.

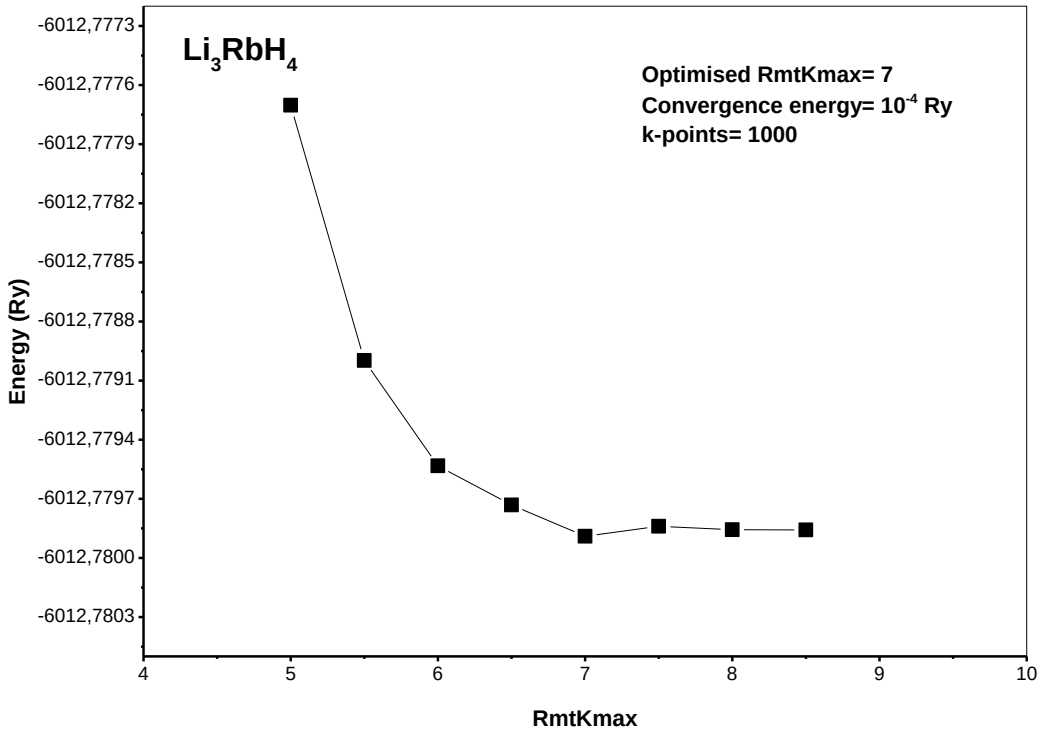


**Figure A.A30:** Total energy of $Li_3RbH_4$ versus RmtKmax.

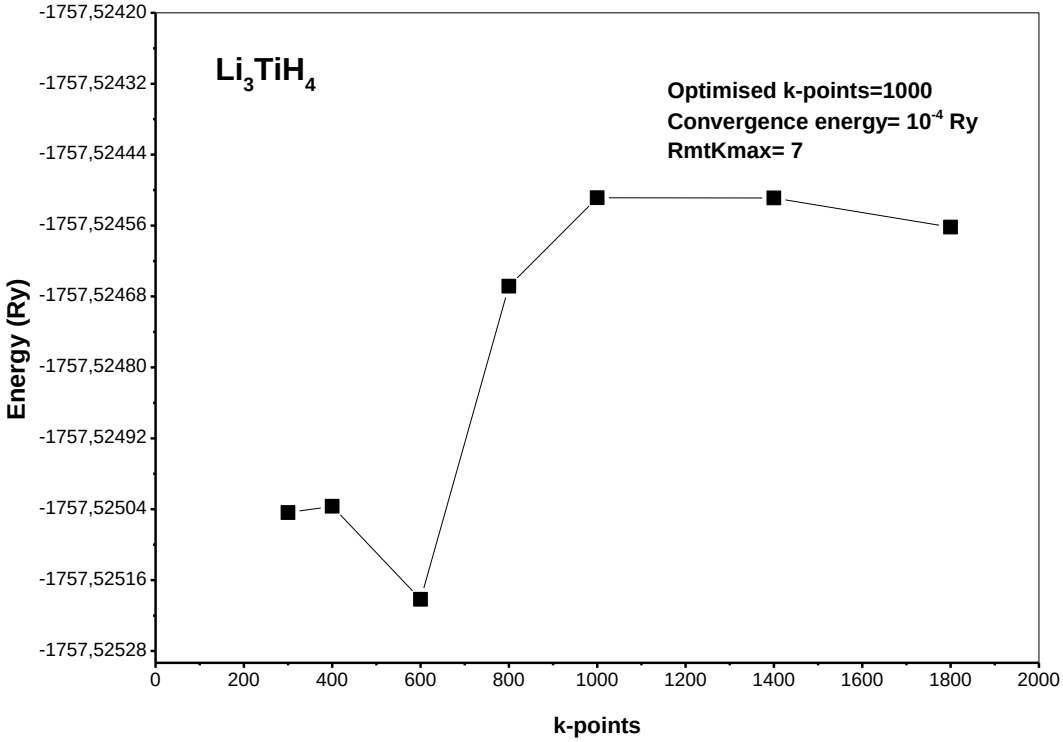


**Figure A.A31:** Total energy of $Li_3TiH_4$ versus k-points.

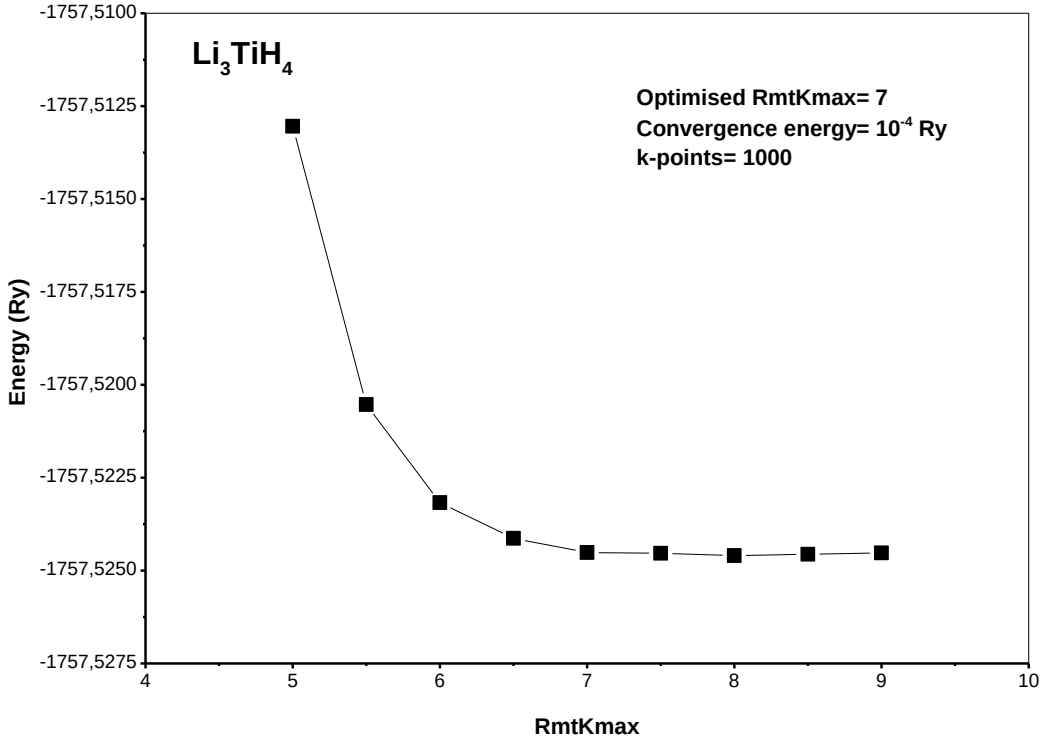


**Figure A.A32:** Total energy of $Li_3TiH_4$ versus RmtKmax.

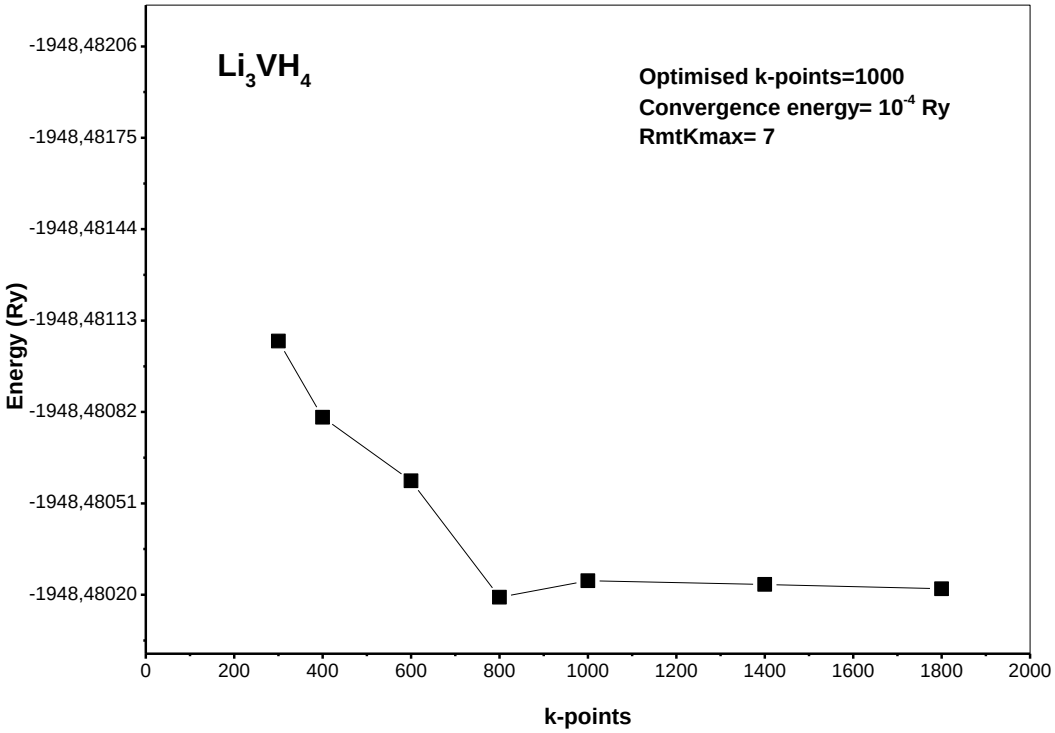


**Figure A.A33:** Total energy of $Li_3VH_4$ versus k-points.

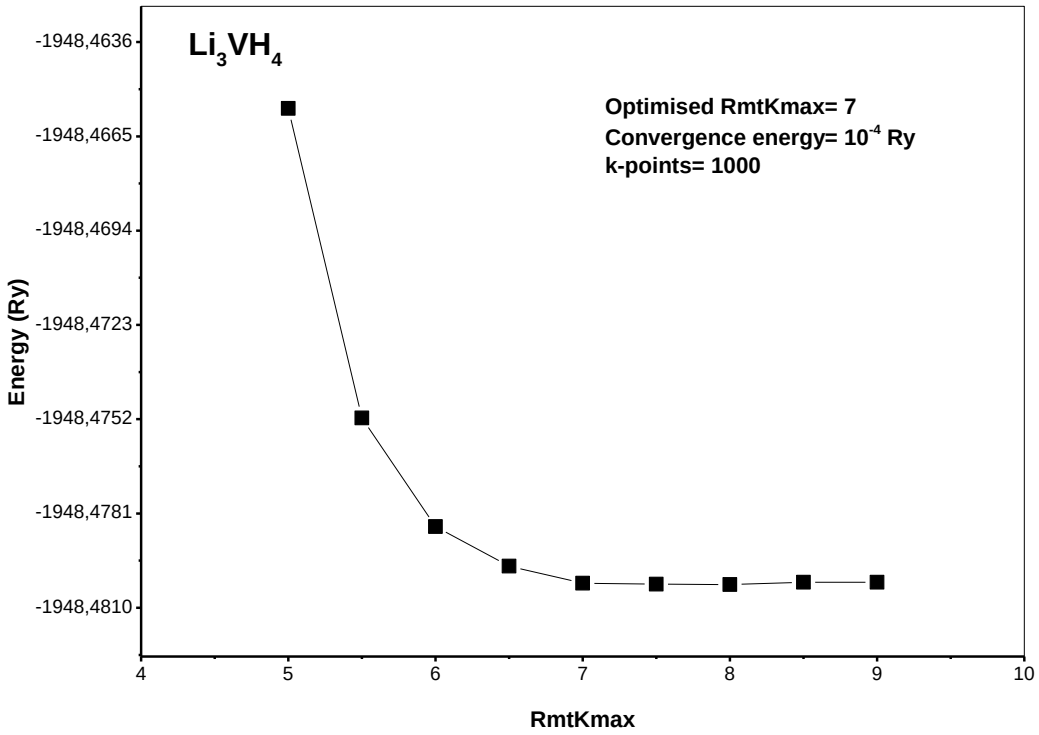


**Figure A.A34:** Total energy of $Li_3VH_4$ versus RmtKmax.

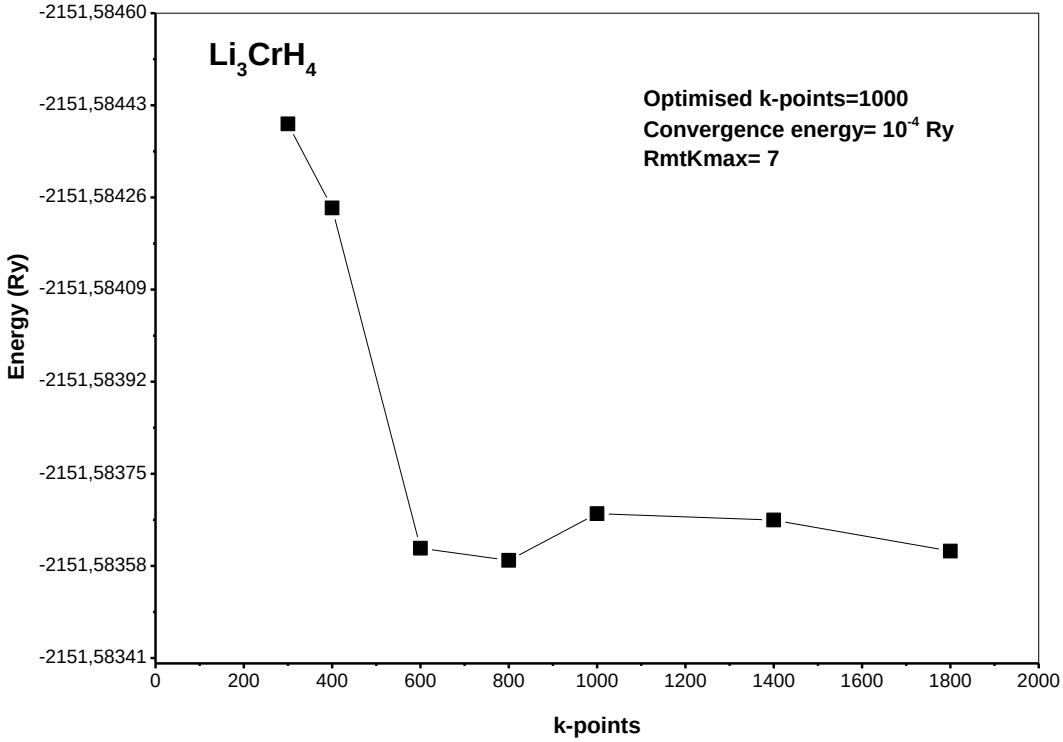


**Figure A.A35:** Total energy of $Li_3CrH_4$ versus k-points.

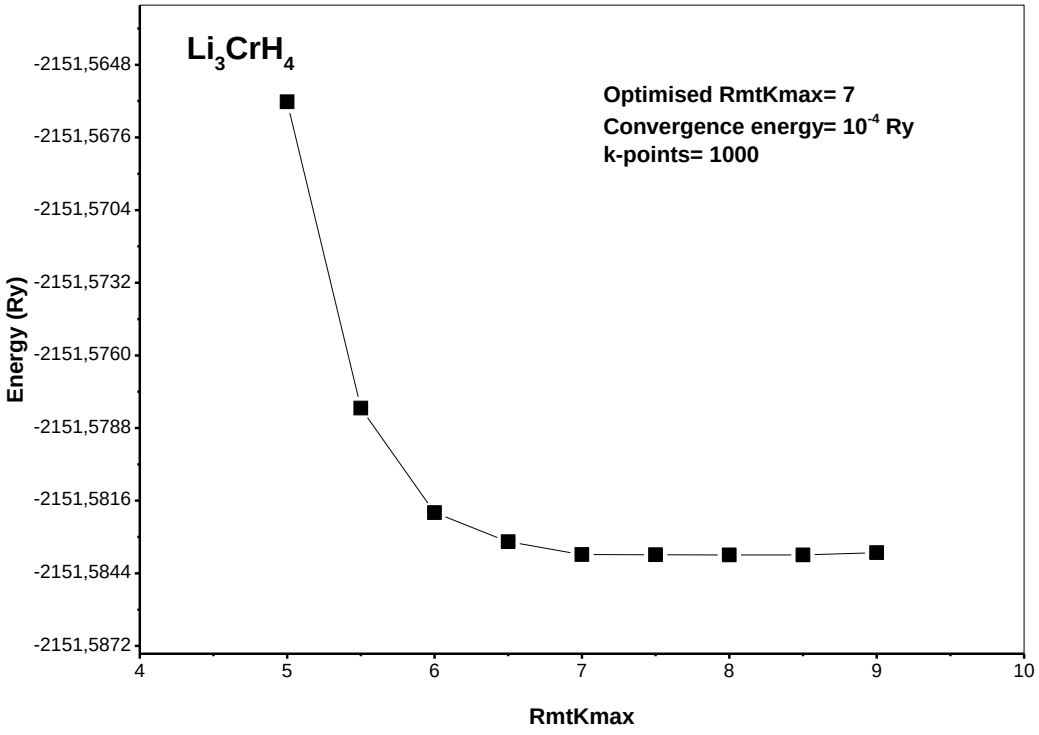


**Figure A.A36:** Total energy of $Li_3CrH_4$ versus RmtKmax.

# Appendix B

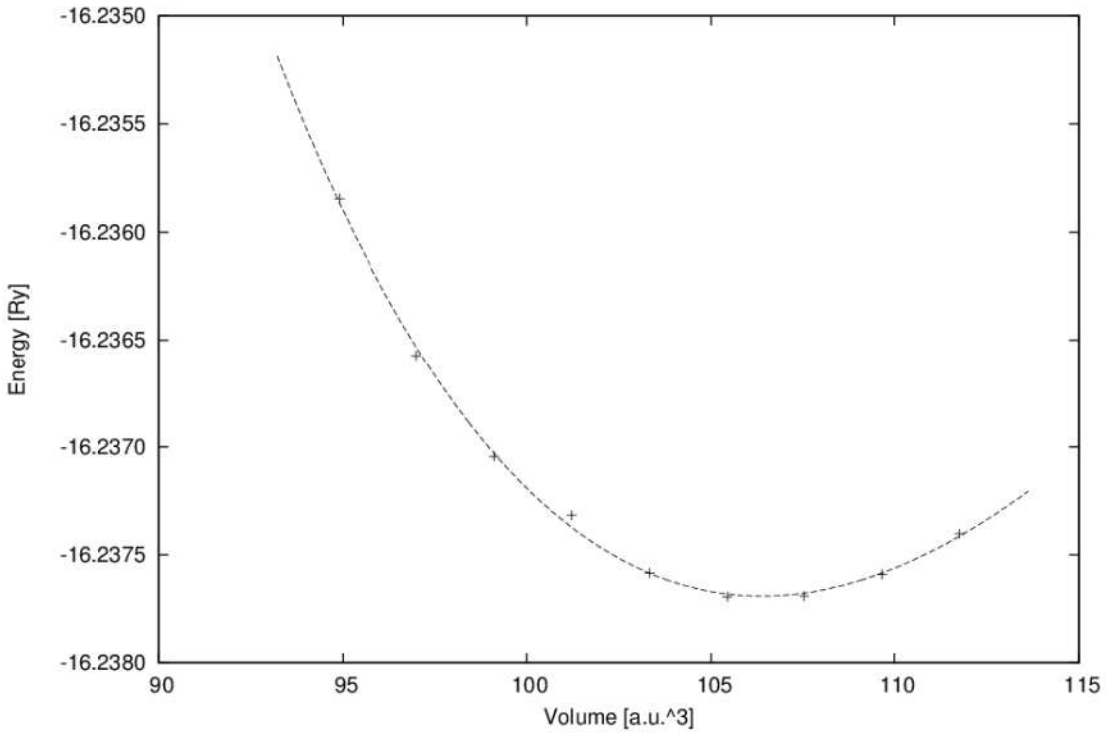


**Figure A.B1:** Total energy of LiH_221 versus volume

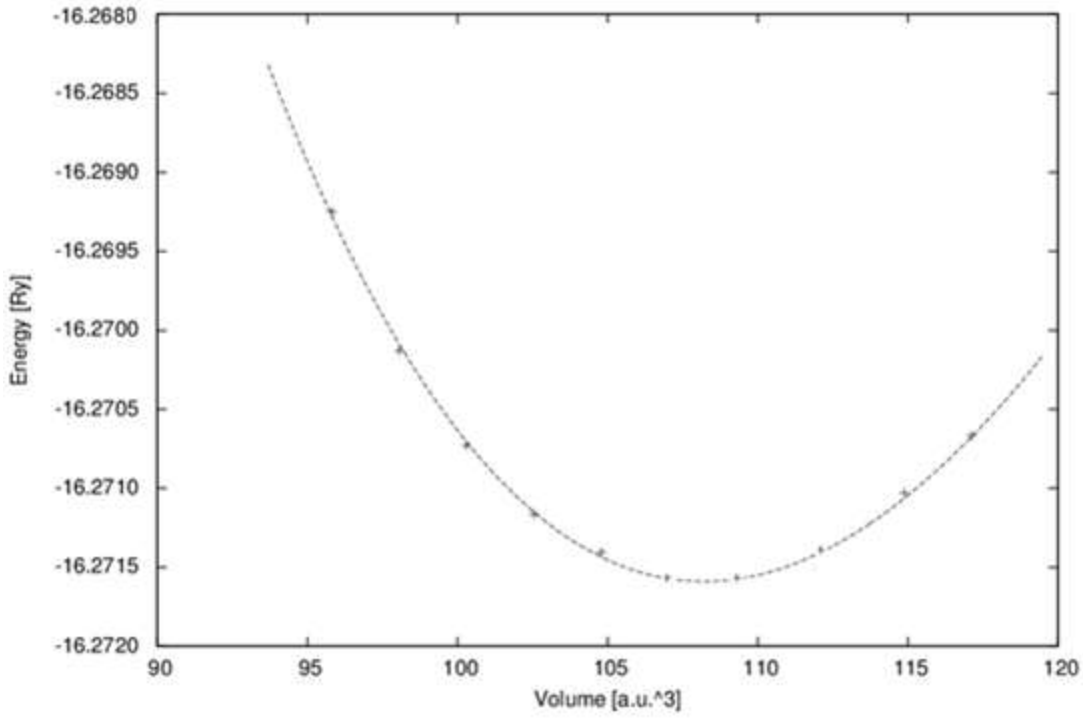


**Figure A.B2:** Total energy of LiH_225 versus volume

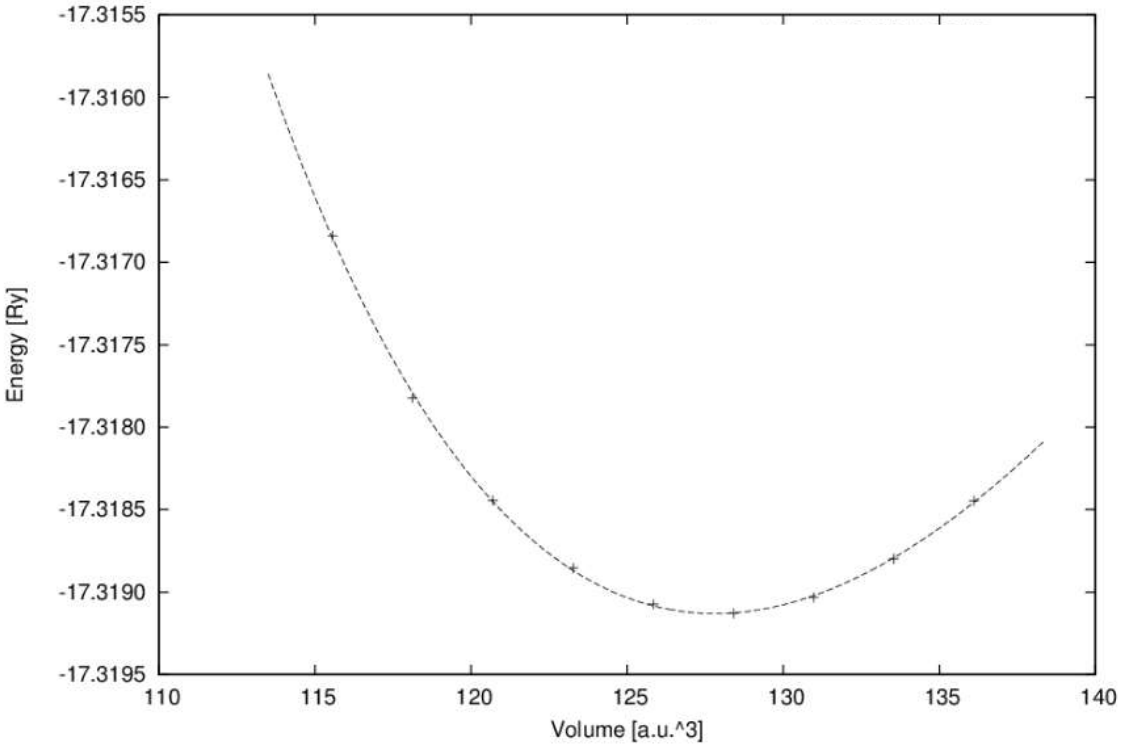


**Figure A.B3:** Total energy of $LiH_2$_191 versus volume

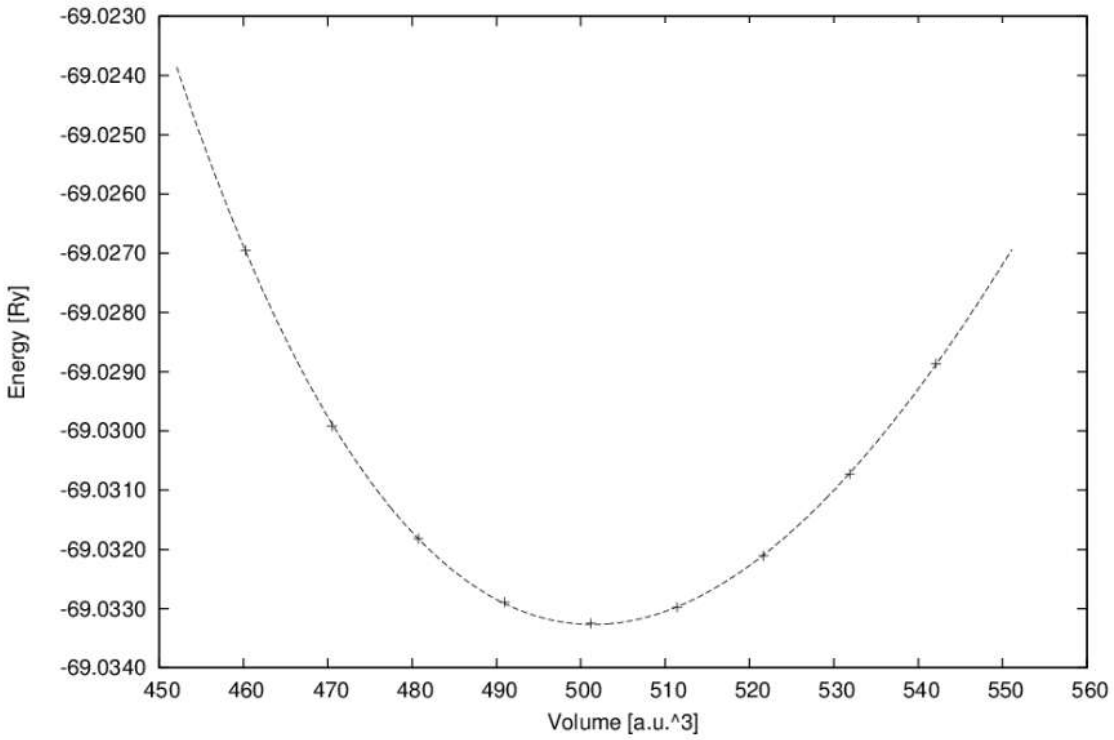


**Figure A.B4:** Total energy of $LiH_2$_194 versus volume

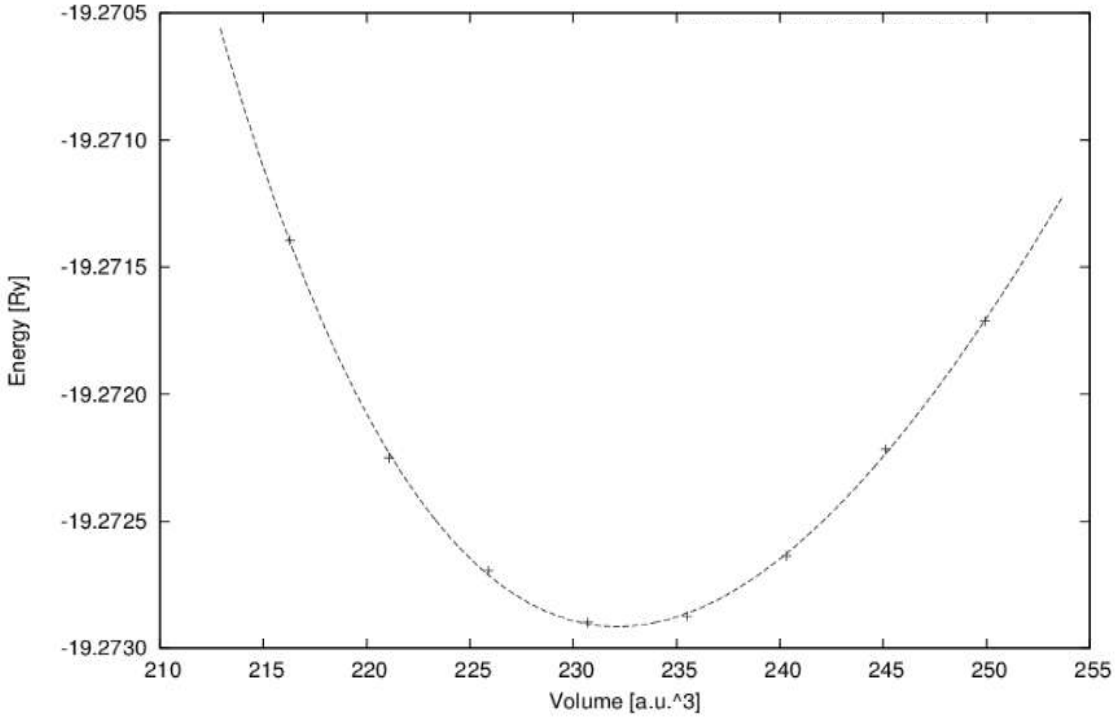


**Figure A.B5:** Total energy of $LiH_4$_215 versus volume

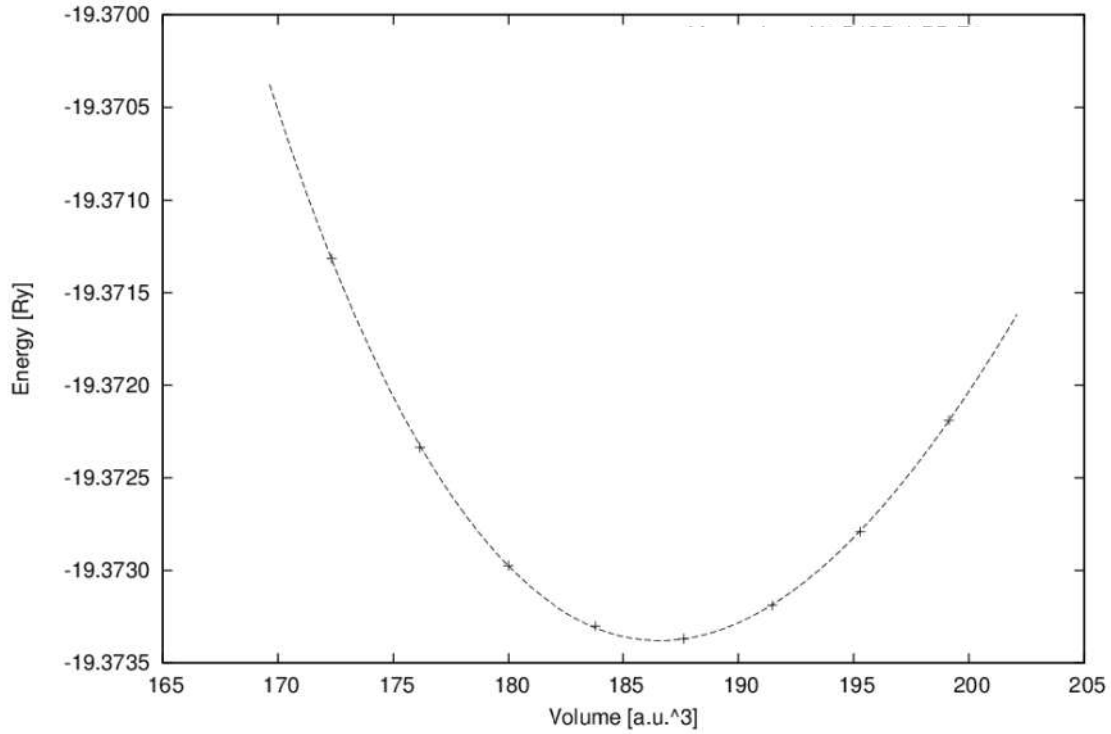


**Figure A.B6:** Total energy of $LiH_4$_221 versus volume

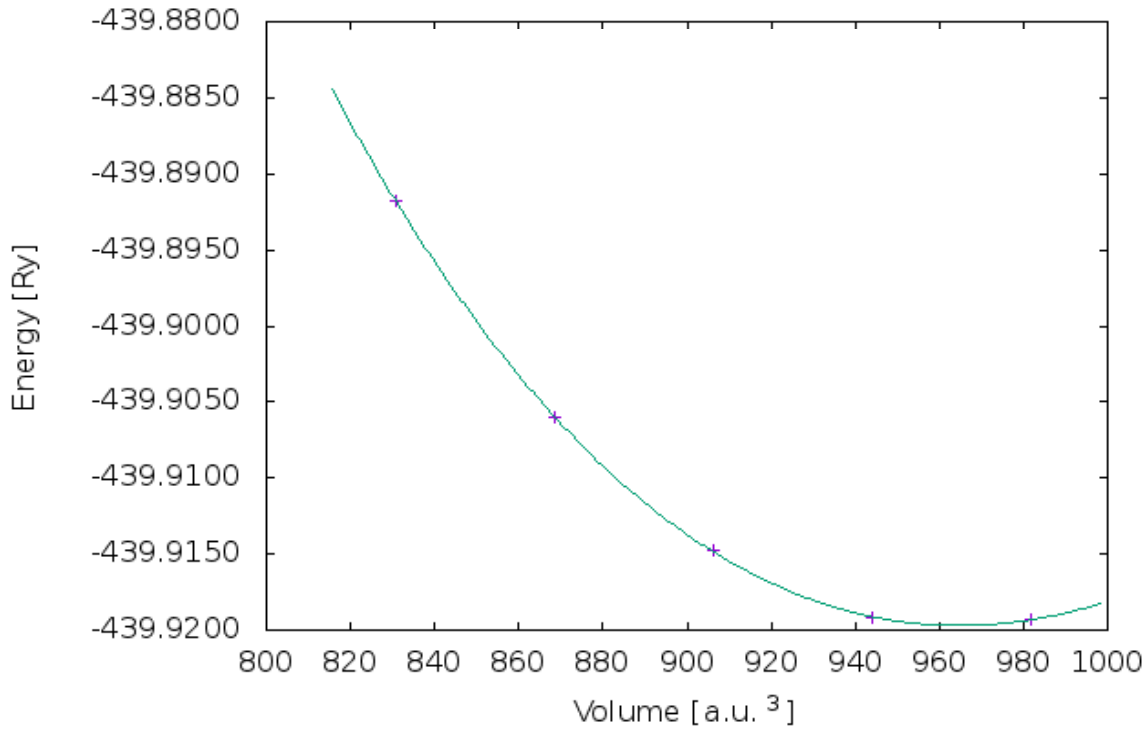


**Figure A.B7:** Total energy Li7NaH8 versus volume

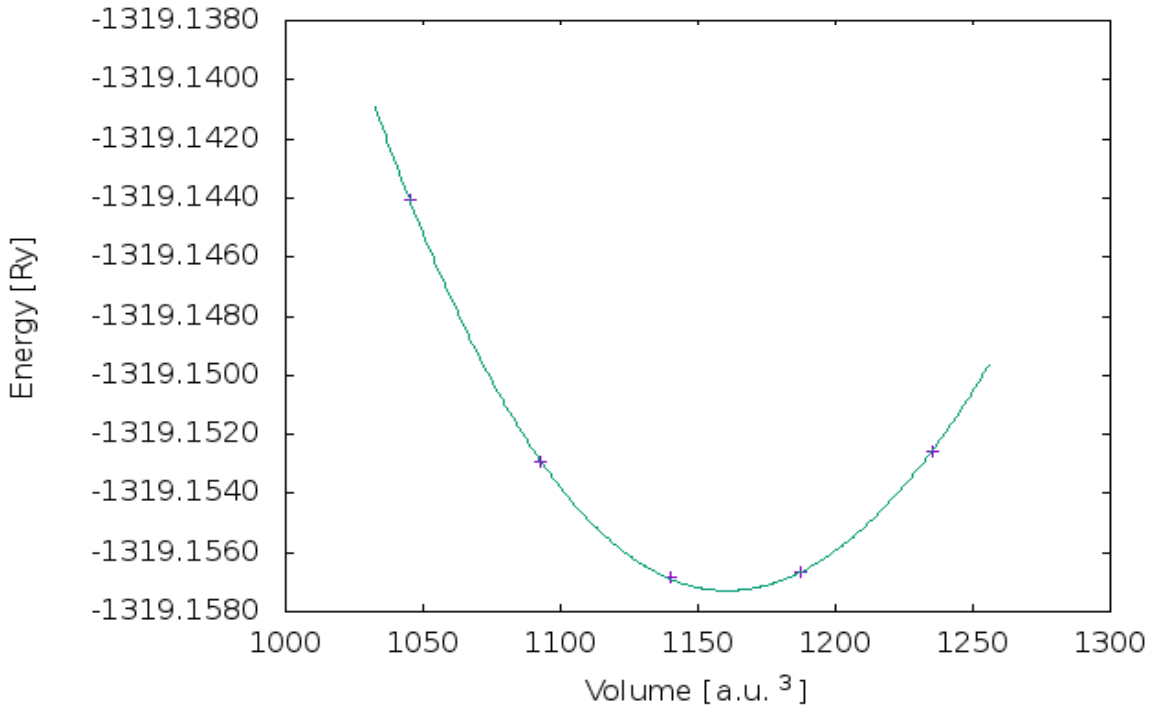


**Figure A.B8:** Total energy of $Li_7KH_8$ versus volume

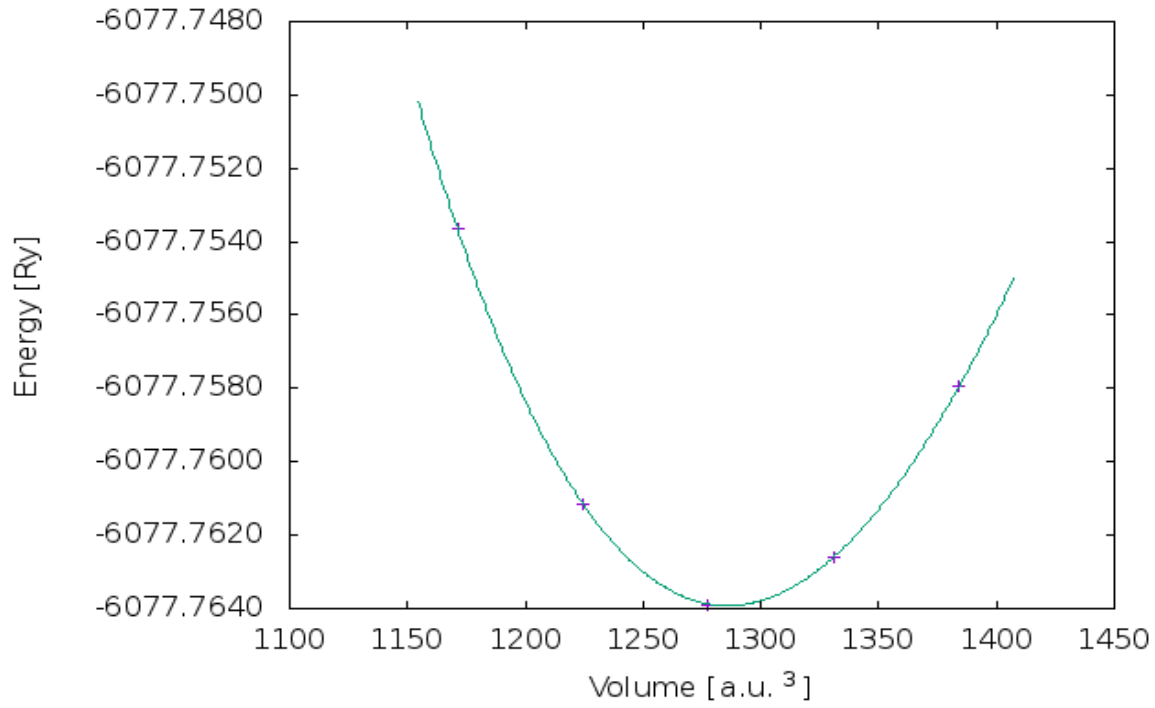


**Figure A.B9:** Total energy Li7RbH8 versus volume

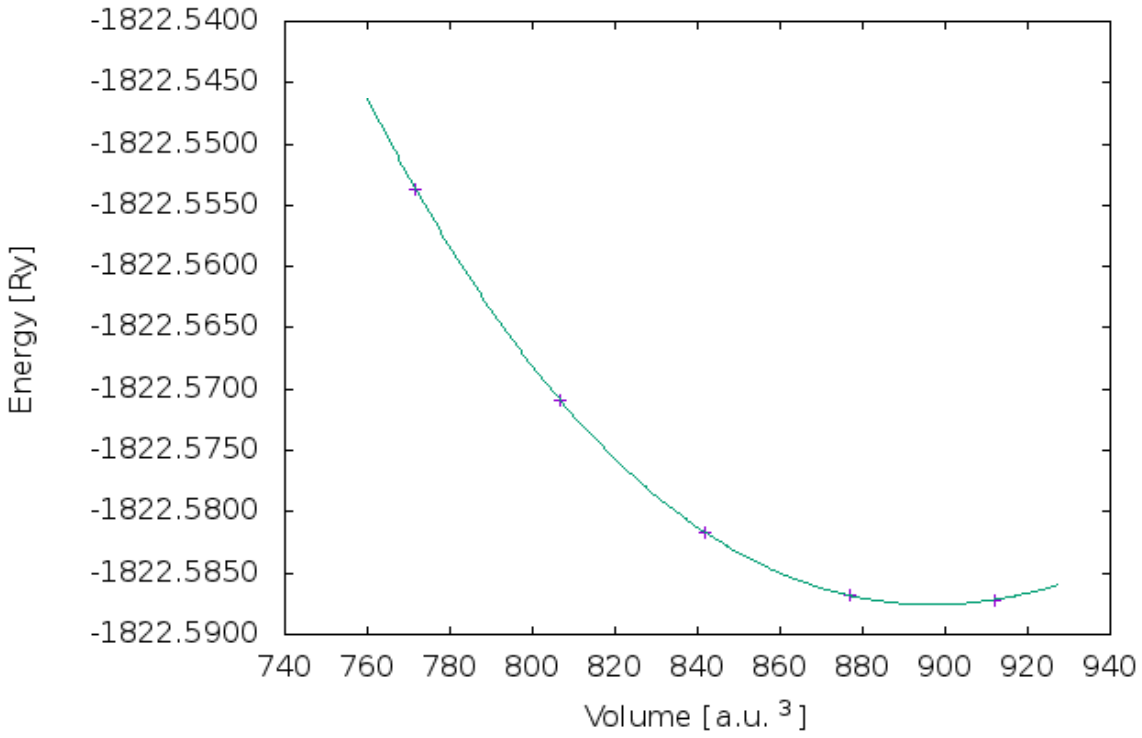


**Figure A.B10:** Total energy Li7TiH8 versus volume

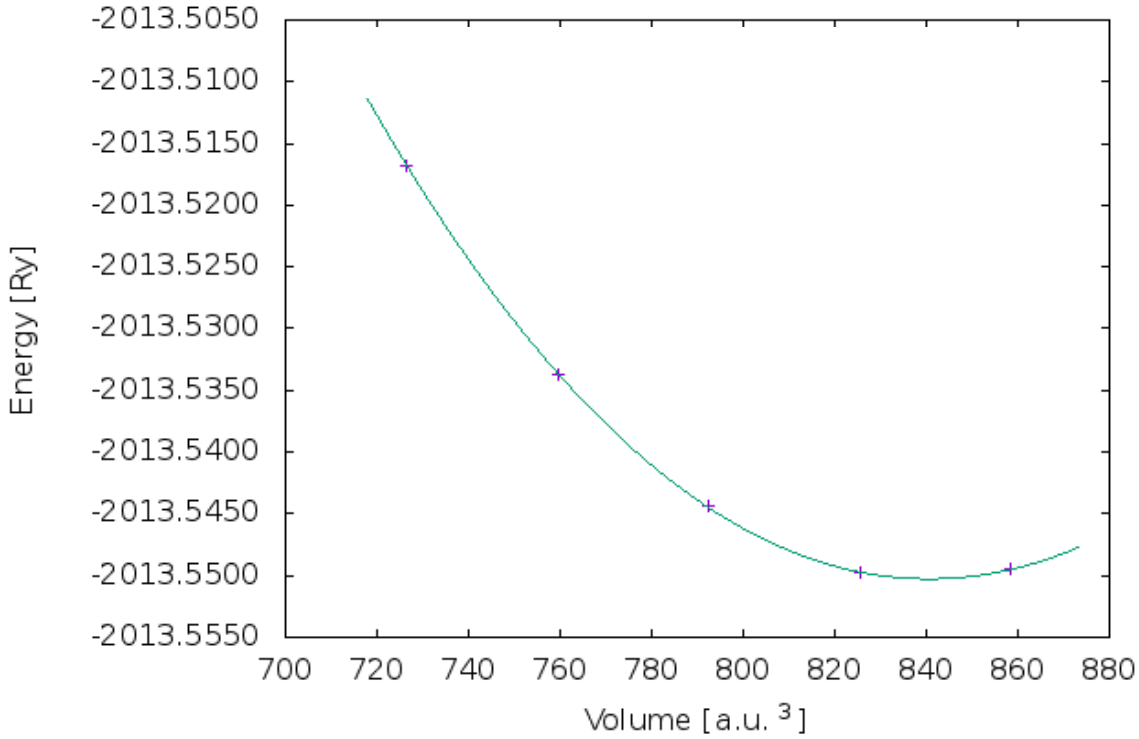


**Figure A.B11:** Total energy Li7VH8 versus volume

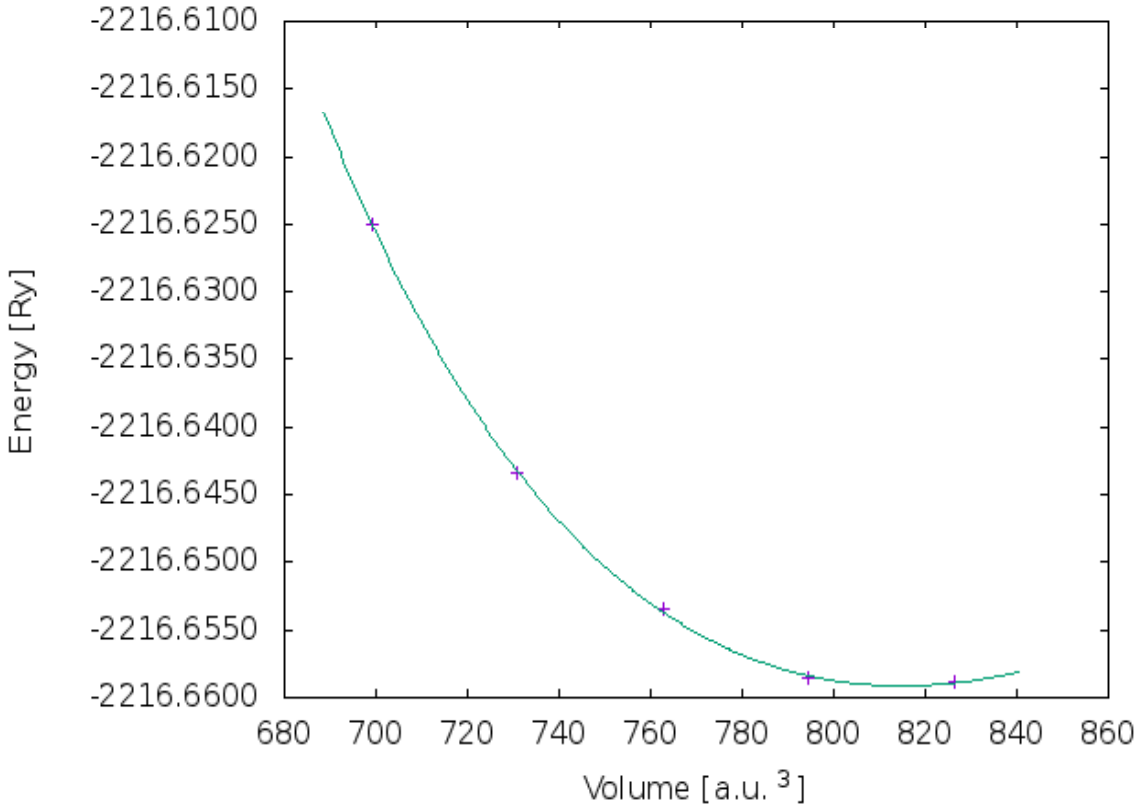


**Figure A.B12:** Total energy $Li_7CrH_8$ versus volume

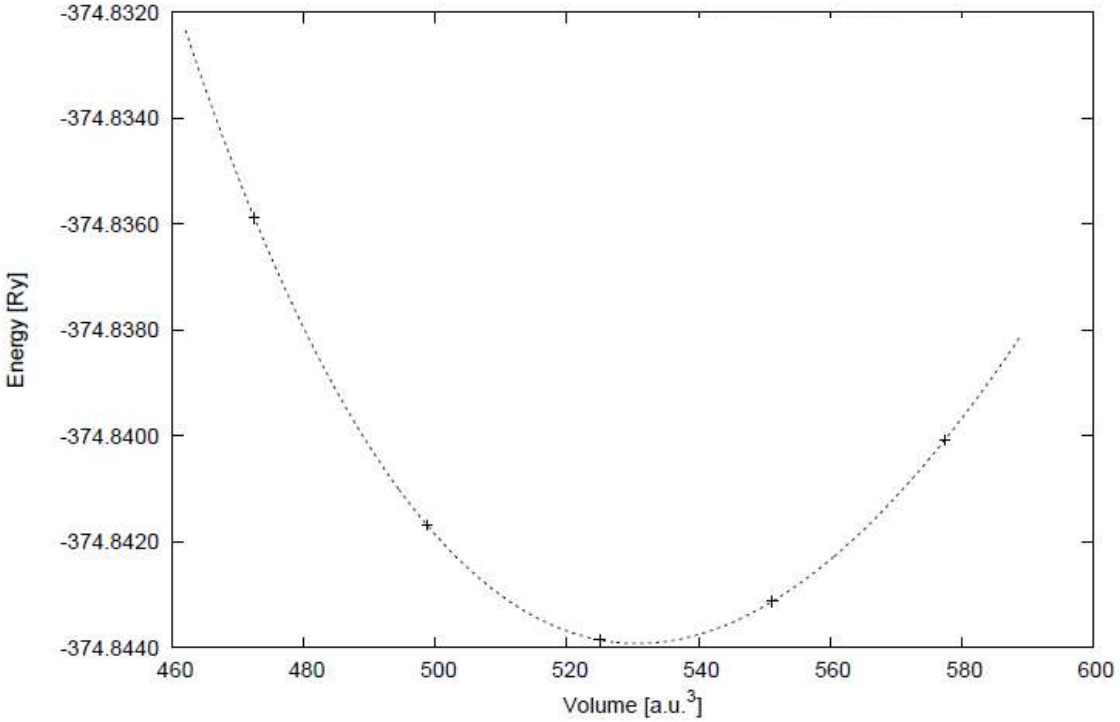


**Figure A.B13:** Total energy of $Li_3NaH_4$ versus volume

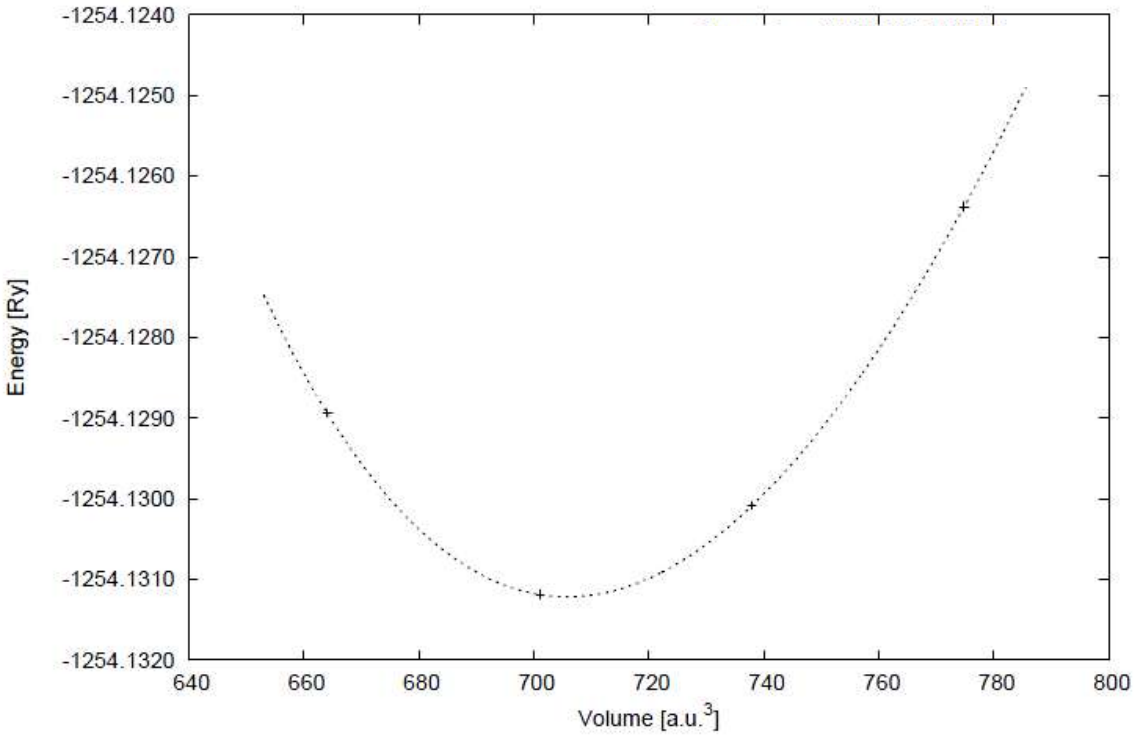


**Figure A.B14:** Total energy of $Li_3NaH_4$ versus volume

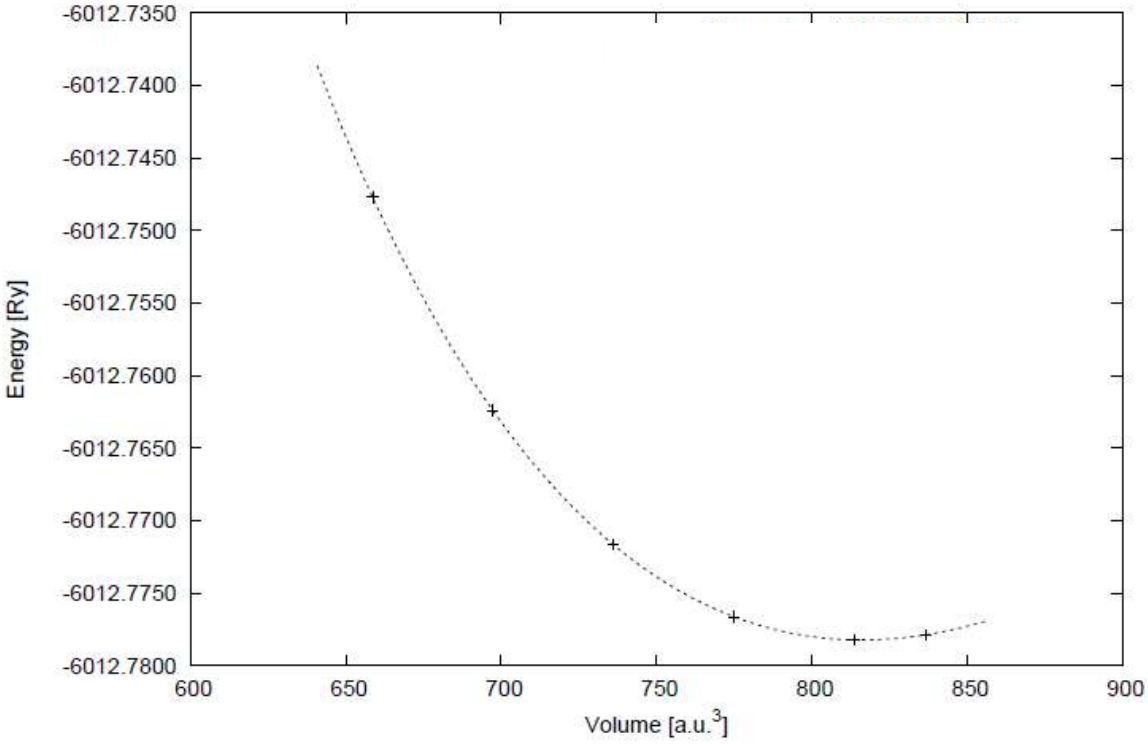


**Figure A.B15:** Total energy of $Li_3RbH_4$ versus volume

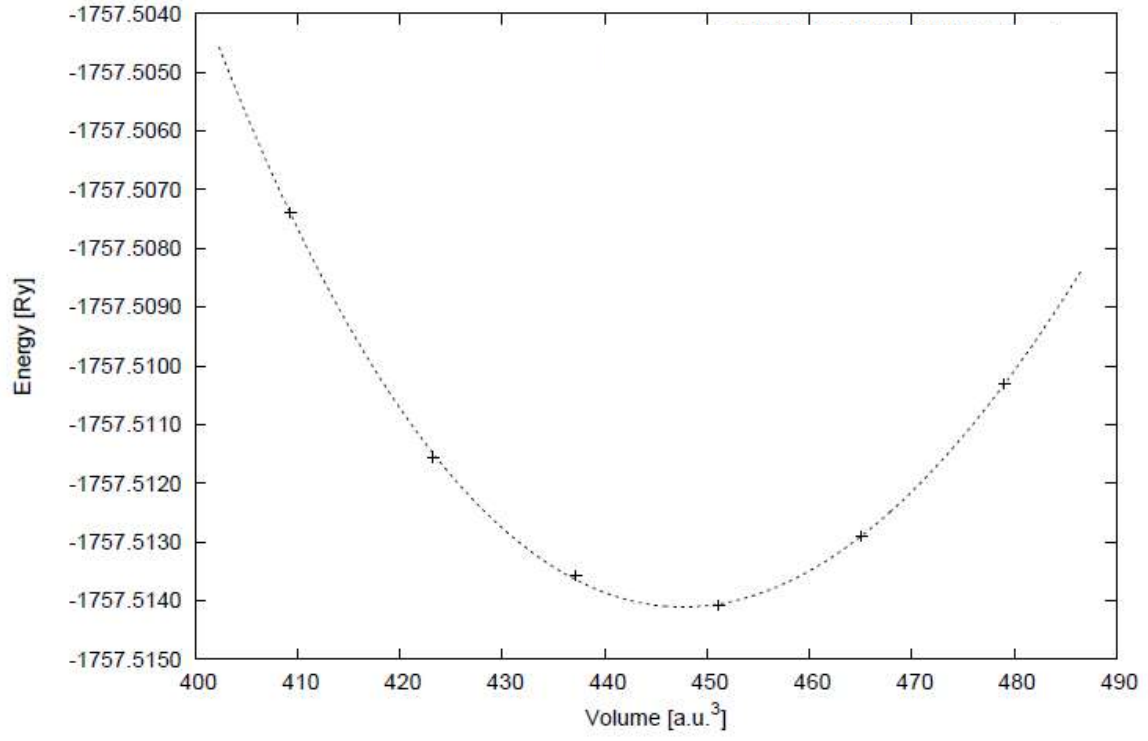


**Figure A.B16:** Total energy of $Li_3TiH_4$ versus volume

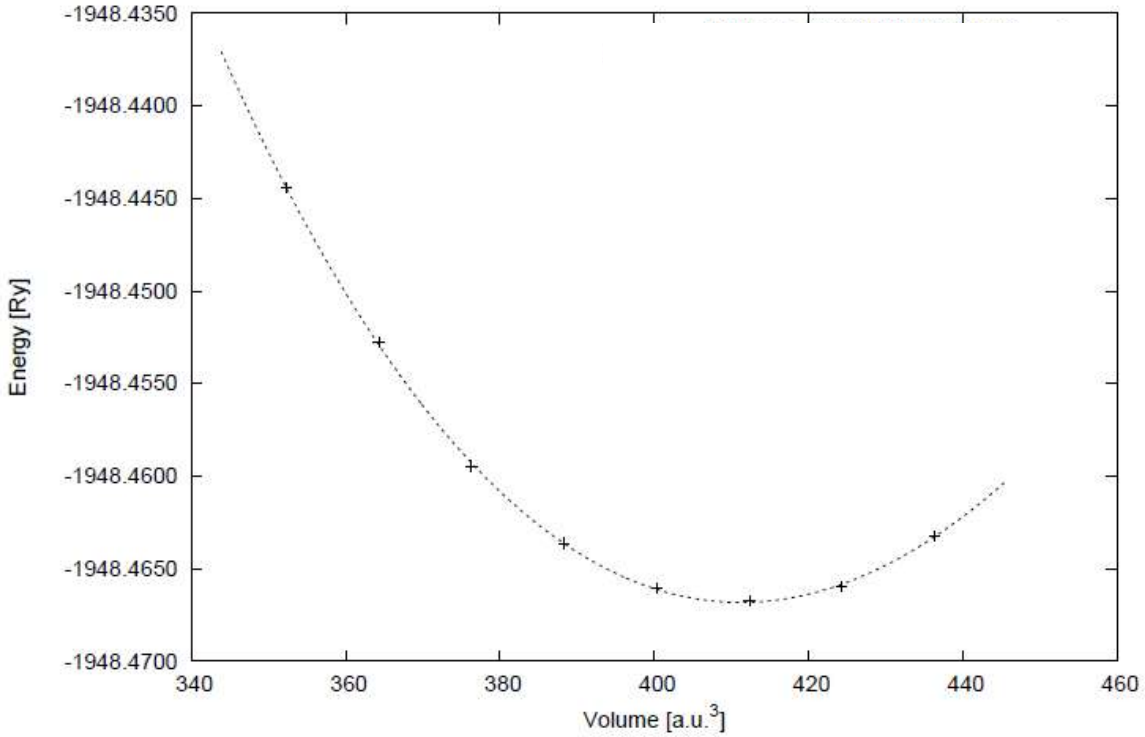


**Figure A.B17:** Total energy of $Li_3VH_4$ versus volume

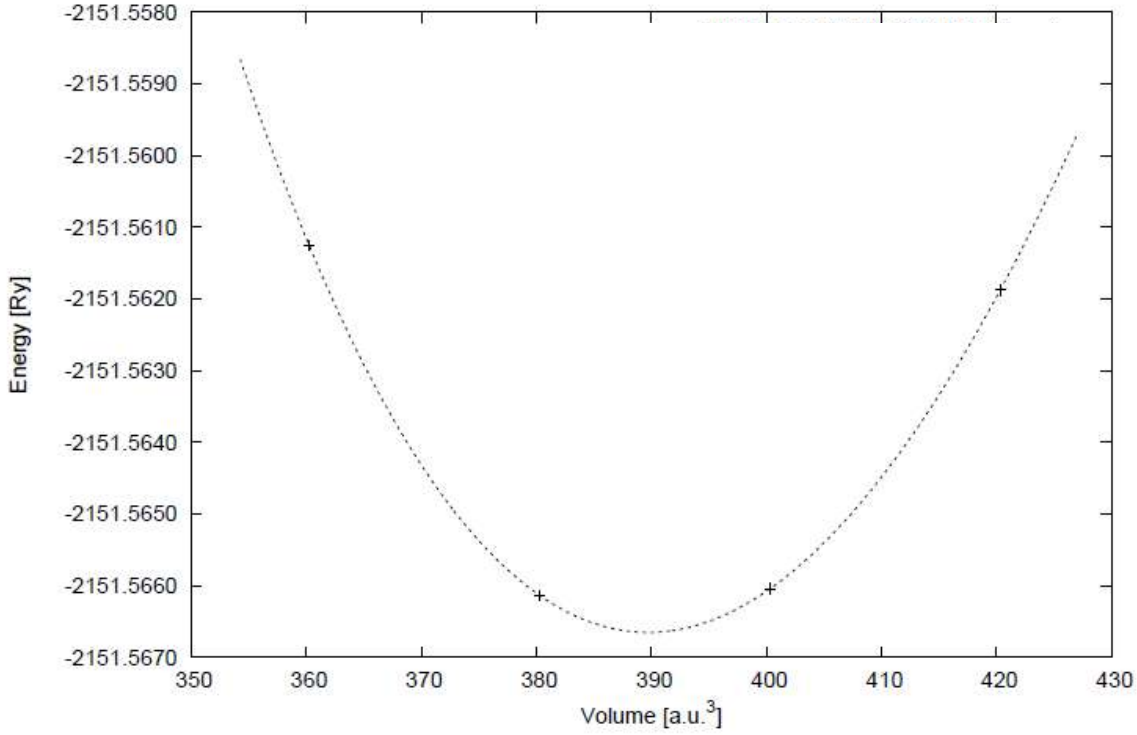


**Figure A.B18:** Total energy of $Li_3CrH_4$ versus volume